DESIGN AND DEVELOPMENT OF NOVEL LARGE SCALE APPLICATIONS IN MICRO/NANOPHOTONICS AND NANOBIOTECHNOLOGY

A DISSERTATION SUBMITTED TO
MATERIALS SCIENCE AND NANOTECHNOLOGY PROGRAM
OF THE GRADUATE SCHOOL OF ENGINEERING AND SCIENCE
OF BILKENT UNIVERSITY
IN PARTIAL FULFILLMENT OF THE REQUIREMENTS
FOR THE DEGREE OF
DOCTOR OF PHILOSOPHY

By
Erol Özgür
August, 2014

I certify that I have read this thesis and that in my opinion it is fully adequate, in scope and in quality, as a thesis of the degree of Doctor of Philosophy.

…….

Prof. Dr. Mehmet Bayındır (Advisor)

I certify that I have read this thesis and that in my opinion it is fully adequate, in scope and in quality, as a thesis of the degree of Doctor of Philosophy.

…….

Prof. Dr. Engin Umut Akkaya

I certify that I have read this thesis and that in my opinion it is fully adequate, in scope and in quality, as a thesis of the degree of Doctor of Philosophy.

…….

Assoc. Prof. Dr. Mehmet Özgür Oktel

I certify that I have read this thesis and that in my opinion it is fully adequate, in scope and in quality, as a thesis of the degree of Doctor of Philosophy.

…….

Assoc. Prof. Dr. Mecit Yaman

I certify that I have read this thesis and that in my opinion it is fully adequate, in scope and in quality, as a thesis of the degree of Doctor of Philosophy.

…….

Assist. Prof. Dr. Necmi Bıyıklı

Approved for the Graduate School of Engineering and Science:

…….

Prof. Dr. Levent Onural

Director of the Graduate School of Engineering and Science

ABSTRACT

DESIGN AND DEVELOPMENT OF NOVEL LARGE SCALE APPLICATIONS IN MICRO/NANOPHOTONICS AND NANOBIOTECHNOLOGY

Erol Özgür

Ph.D. in Materials Science and Nanotechnology

Supervisor: Prof. Dr. Mehmet Bayındır

August, 2014

Developments in micro/nanophotonics and nanobiotechnology creates new opportunities regarding development of devices with unprecedented capabilities, which could improve human civilization substantially. On the other hand, a certain level of maturity in transforming these possibilities into reality still requires considerable efforts. One of the main problems of these novel technologies is that their practical know-how is so scarce that they could only be utilized within strictly determined laboratory conditions, and by highly sophisticated scientists.

This thesis focuses on large scale applications at the intersection of microphotonics and nanobiotechnology, and also in nanophotonics. On microphotonics side, optical microresonators with toroidal shape were successfully fabricated and optically integrated. Having an extremely high sensitivity towards perturbations in their environments, these microcavities could be used as biological sensors; however, they are also very sensitive for nonspecific interactions. Thus, a novel surface chemistry enabling bioconjugation of molecular probes without compromising their sensitivity and enhancing their selectivity was developed, based on methylphosphonate containing silane modification of the microtoroid surface. After this functionalization, microtoroids were used in biodetection in complex media.

Also, a macroscopic photodetection device composed on intrinsically aligned semiconducting selenium nanowires were demonstrated. This device could be considered as a novel and efficient demonstration of nanowire integration to the macroscopic world. Together with the research on biosensors, these are important large scale applications of emergent science of our age.

Keywords: Microtoroid, microphotonics, selectivity, sensitivity, surface chemistry, nanobiotechnology, nanophotonics, semiconducting nanowires, large scale application.

ÖZET

MİKRO/NANOFOTONİK VE NANOBİYOTEKNOLOJİ İÇİN YENİ YAYGIN UYGULAMALAR TASARLANMASI VE GELİŞTİRİLMESİ

Erol Özgür
Malzeme Bilimi ve Nanoteknoloji, Doktora
Tez Yöneticisi: Prof. Dr. Mehmet Bayındır
Ağustos, 2014

Mikro/nanofotonik ve nanobiyoteknolojideki gelişmeler, insan uygarlığını büyük oranda değiştirebilecek, daha önce düşünülmemiş özelliklere sahip aygıtların ortaya çıkma ihtimalleri sunmaktadır. Bununla birlikte, bu ihtimalleri gerçekliğe dönüştürecek birikimin oluşması hala önemli bir çaba gerektirmektedir. Söz konusu yeni teknolojilerin en önemli sorunlarından bir tanesi, uygulamaları ile ilgili teknik bilginin azlığından dolayı, sadece çok iyi denetlenen laboratuvar koşullarında uzman araştırmacılar tarafından ilgili çalışmaların yürütülebilmesidir.

Bu tezin amacı, mikrofotoniğin nanobiyoteknoloji ile kesişiminde, ayrıca nanofotonik alanında yaygın uygulamaların geliştirilebilmesidir. Mikrofotonik alanı içinde toroid şekilli optik mikrorezonatörler üretilmiş ve ışıkla eşlenmişlerdir. Çevrelerindeki en ufak değişikliğe karşı bile çok hassas olan bu yapıların bu özelliğinden biyolojik sensörlerde faydalanılması amaçlanmakla beraber, bu durum beraberinde seçici olmayan etkileşmelere karşı da istenmeyen seviyede bir hassasiyet getirmektedir. Bu sorunun aşılması amacıyla hem protein dirençli hem de biyoeşlenebilir bir yüzey kaplaması geliştirilmiş, yüzeyi bu kaplamayla işlevselleştirilen mikrotoroidler, karmaşık ortamda biyolojik ölçüm yapmak için kullanılmıştır.

Ayrıca, kendiliğinden düzenli yarıiletken selenyum nanoteller kullanılarak, makroskopik boyutta bir fotoalgılayıcı cihaz üretilmiştir. Bu cihaz, makroskopik dünyaya nanotel entegrasyonunda yeni ve verimli bir yöntem sunmaktadır. Biyosensör çalışması ile birlikte ele alındıklarında, çağımızın yükselen bilimi ile ilişkili önemli yaygın uygulamalar gösterilmiştir.

Anahtar kelimeler: Mikrotoroid, mikrofotonik, seçicilik, hassasiyet, yüzey kimyası, nanobiyoteknoloji, nanofotonik, yarıiletken nanoteller, yaygın uygulama.

Acknowledgement

First and foremost I would like to thank my academic advisor, Prof. Mehmet Bayındır, not only for the support and guidance he provided me throughout my dissertation, but also for the extremely valuable independence that he provided me during the course of my Ph.D., enabling me to utilize my creativity to its fullest extent, while simultaneously encouraging me to push the limits of the research furthermore. Being a member of Bayındır Research Group was a memorable experience, which I believe will continue to shape my future career as a scientist.

And also, all the faculty members, researchers, students and staff of UNAM-National Nanotechnology Research Center *a priori* deserve acknowledgement, appreciation and admiration. I would like to thank especially to Prof. Salim Çıracı for pioneering the establishment of such an invaluable research center.

I would like to express my acknowledgement to The Scientific and Technological Research Council of Turkey, TÜBİTAK, for the Ph.D. Scholarship I have benefited throughout my Ph.D.

Research is always a teamwork, and synergistic effect is ultimate in success. As a part of the team, I earnestly express that without my teammates, it would be impossible for me to accomplish even only a small part of what I have done. In particular, collaborating with Ozan Aktaş was one of my greatest opportunities in the course of my Ph.D. I do not even remember the number of problems, whether scientific or technical, that we solved together. An extremely talented researcher and natural born scientist like him is very difficult to be found elsewhere. Pelin Tören, although joined our group much later, also had an incredibly positive effect on both the route of my research, and my life. I am grateful for her resilient criticism that helped me to shift my point of view towards illumination for a myriad of times, and her sincere friendship. Lastly, I would like to thank one of the most open hearted person I have ever known, Ersin Hüseyinoğlu. Although his type of people have almost all became extinct, he stands there, self-confident, like a stone, providing constant trust, in research, and in life.

Besides my teammates, here I also met other people that was also really fun to work with and talk to, and share thoughts and feelings. Adem Yildirim is one of them, whom I enjoyed much to be a colleague and a friend, and I hope we collaborate and meet every once in a while in future. I find people who really like talking quite amusing, and so is Bihter Dağlar. She is another person that I would like to see around and work together. I also want to express my gratitude to present and former Bayındır Research Group members: Fahri Emre Öztürk, Muhammad Yunusa, Tamer Doğan, Urandelger Tuvshindorj, Mehmet Kanık, Tural Khudiyev, Bekir Türedi, Pınar Beyazkılıç, Girayhan Say, Gökçen Birlik Demirel, Osama Tobail, Mostafa M. El-Ashry, İbrahim Yılmaz, Emel Gürbüz, Murat Dere, Dilara Öksüz, Hale Nur Çöloğlu, Seyit Ali Yaşar, Neşe Özgür, Mecit Yaman, Abdullah Tülek, Hakan Deniz, Hüseyin Duman, Muhammet Çelebi, Yunus Çetin, Duygu Akbulut, Kemal Gürel, Murat Celal Kılınç, Mert Vural, Enes Korkut, and Ahmet Ünal.

A person who deserves a special thank is my old friend Ali Aytaç Seymen. We, together, had a dream, and now we are on the verge of realizing it. I hope our harmony lasts for much longer times. I also would like to thank Bülend Ortaç for supporting our dream and believing in us. Lastly, from UNAM, I believe it would be incomplete without thanking Engin Umut Akkaya, Aykutlu Dana, Necmi Bıyıklı, Çağlar Elbüken, Mustafa Özgür Güler, Ali Kemal Okyay, Ayşe Begüm Tekinay, Urartu Şeker, Okan Öner Ekiz, Çağla Özgit Akgün, Ayşegül Abdelal, Melis Şardan, Aslı Çelebioğlu, Fatma Kayacı, Hakan Ceylan, Eda Çetinörgü Goldenberg, Rashad Mammadov, Sabri Alkış, Hasan Şahin, Handan Acar, Seymur Cahangirov, Selim Sülek, Enver Kahveci, Mustafa Güler, Zeynep Ergül Ülger, Semih Yaşar, Fikret Piri, Gökçe Çelik, Adem Saraç, Koray Mızrak, Emre Tanır, Mustafa Kemal Ruhi, and Burkan Kaplan.

And of course, my sweet family. Ekin Özge Özgür, my dear wife: Without her constant support and patience, nothing would be possible. She transformed me to the person I am now. She taught me love, and passion, and dignity. She taught me that being a good partner in life is more important than being a good scientist, and career is of no importance when family is the issue. She also gave me the most valuable present that I have ever had, our son, Erkin Ozan. I would not trade a thousand Ph.D. degrees for him. All I did, am doing and will do is for my family. Also, I would like to express my limitless thanks to my parents, Gülbahar and Bayram. Even if I am an

adult now for a long time, trying to stand on my very own feet, it is good to know that there is a place where I can always call “home”, no matter what happens.

As a last world, I dedicate my thesis to all graduate students. I wish they, the essence of research, will get what they deserve soon. I find it irrational and immoral that they are simultaneously indispensable and insignificant in front of the eyes of the scientific community. I believe things are changing to better, and as a scientist, I will definitely be on the side of progress regarding this issue.

Contents

List of Figures

List of Tables

Chapter 1

Biosensing with Optical Microcavities

1.1 Introduction

As humans we, similar to virtually all other animals, gather qualitative and quantifiable information from the universe via our highly sophisticated sensory organs, which evolved within millions of years, driven by the probabilistic and imperfect nature of life that also enabled our existence. The source of external stimuli, besides the environmental physical parameters such as temperature, moisture, light, etc., is mostly related to living organisms directly or indirectly, shaping the course of the evolution of life and; therefore, of the sensory organs, regarding the eminent phenomenon denominated as natural selection. The emergence of human civilization; however, with rapidly increasing communication and collaboration skills among human beings, required more objective and quantitative means of detection of the stimuli of any kind, notwithstanding the subjective nature of the sensory organs developed under the drive of evolution.

A sensor is an artificial tool for detection of a measurable quantity, and transduction of it into a comprehensible and interpretable signal. Among different types of sensors, biological sensors constitute an important branch, since the environment of any living organism consist of organic and also inorganic matter related to biological activity.

Due to the microscopic, even nanoscopic scales that life-related processes occur, proper biological sensing could still be described as an immature field of research. Despite huge efforts after atomic resolution in imaging was attained, and elaborate improvements in physical chemistry and biochemistry in the last fifty years, biosensing still has its own limitations. In an age, where single-photon and single atom measurements can be performed within appropriate technical infrastructure, accurate detection of single proteins or even single bacteria remain challenging, partly because of the complex interactions among life-related entities, and also for the unlimited diversity provided by the organic chemistry based background of life.

People require biosensors both for to understand and manipulate the life. Scientists demand better tools to analyze the molecular pathways, components and mechanisms of physiological and pathological phenomena. In order to comprehend the localization and distribution of the metabolites and also the interactions among them, molecular and cell biologists need fast and reliable tools suitable for multiplexed detection. Genetics and genomics researchers are seeking novel genetic and epigenetic screening methods. Evolutionary biologists try to understand polymorphisms and their distribution in the populations, while oncologists require sensors for quantifying and classifying cancer markers in order to detect pathologies at earlier stages. Microbiology studies are closely related to daily life, because food consumption for survival is actually far too risky without proper supervision, and current technology for food screening heavily depends on conventional tests that are too slow to take appropriate precautions except destruction of even minimally contaminated food. Last but not least, for security issues, i.e., against biological warfare, high sensitivity and selectivity biosensors are important demands of the contemporary society.

1.2 Conventional Methods for Biodetection

The biodetection tools can be divided into two broad categories: Methods that require labeling prior to detection, and label-free methods. Labeling for detection exploits the quantitatively observable materials that are able to produce a measurable

signal themselves or by external means, such as fluorescent molecules. Labeling is performed before detection; therefore, *a priori* information about the existence and the approximate amount of the target molecule is a prerequisite. Label-free methods are more flexible compared to the other methods, where detection precedes labeling, if any required. However, they require a more complex hardware for detection most of the times.

Fluorescent imaging constitutes the most diverse and wide branch of labeling before detection. Because of the diffraction limit in optics, it is impossible to detect targets smaller than the optical resolution limit of about a few hundred nanometers; however, most of the biological entities are much tinier. Fluorescent imaging enables researchers to detect even a few nanometer sized targets quantitatively, because it is straightforward to collect the fluorescence and amplify the signal by a photomultiplier tube (PMT) or charge coupled device (CCD) camera [1]. Although the exact localization of the target molecule still could be ambiguous, the quantity can be precisely estimated from the intensity of the signal. There is an increasing population of fluorescent probes specific to many different targets, and optics technology is improving to subdiffraction spatial and ultrafast temporal resolution. Fluorescent detection will remain as an indispensable tool, especially for basic science research.

One prevalent disadvantage of labeling is the requisite of a specific interaction between the label and the target, which is not always possible. Additionally, a quantifiable alteration in the characteristics of the labeling molecule is required in order to distinguish the interaction from the free form label. These disadvantages lead the development of the label-free methods, which some important examples are summarized below.

Immune system of mammals provides the largest and most well-established platform for label free detection, including but not restricted to various blotting methods and Enzyme-Linked Immunosorbent Assay (ELISA) [1]. Although some variations are under development, the high selectivity and specificity of antigen-antibody reaction is the gold standard for conventional biological detection. Antibodies are readily produced in laboratory animals or culture plates, where the spectacular diversification ability of the immunity related cells are exploited. The

resulting products are used for detection of not only proteins but many other biochemical species. After the bioconjugation among antibodies and their targets occur, different additional strategies, among which the mostly used is the utilization of non-specific fluorescent-chemiluminescent molecules, is used to measure the extent of the interaction quantitatively.

Major problem related to immunologic detection is that the minimum detectable quantity is far more than single molecule. Therefore, alternative methods for detection are being developed. Since the immunogenic interactions are incredibly selective and specific, related research focuses on revealing the minimum amount of these interactions possible. Rather than a subsequent labeling step that reduces the efficacy, alternative methods for detection of antigen-antibody interaction were introduced in recent years, among which surface plasmon resonance (SPR) and quartz crystal microbalance (QCM) are frequently utilized.

SPR depends on the excitation of the surface plasmons by light on metallic surfaces at a specific incident angle. Depending on the chemistry over the metal surface and the wavelength of the incident light, the resonant angle is altered. Researchers exploit this characteristic to determine the immunogenic interactions at the surface *in situ*. A thin layer of metal, mostly gold, coated substrate is conjugated with the targeting probes such as antibodies, and the analyte solution is passed over the surface. Any interaction among the antibodies and the target shifts the resonant angle proportional to the strength of the interaction. Therefore, quantitative information about the amount of the target, and also the reaction rates could be collected. Even though single-molecule detection is not attainable by SPR, the method provides a fast and reliable alternative to conventional methods [2].

Another promising method is QCM, where the oscillations occurring in a piezoelectric material, quartz, is used for detection. The frequency of the oscillation depends on the mass of the quartz plate, and any alteration in the mass shifts this frequency. When the target interacts with the antibodies, coated on the surface of the quartz plate in a similar fashion with SPR, the shift in the oscillation frequency could be transduced as a signal that reveals the binding [3]. This method is shown to detect very low quantities [4], but single molecule interactions have not been reported yet.

1.3 Whispering Gallery Mode Microresonators for Biodetection

A resonator is a system that light continuously oscillates back and forth at specific wavelengths (or frequencies) depending on the size of the cavity constituting the resonator structure. The resonant wavelengths could be determined by the total path length, because the path length should be an integer multiple of the wavelength, providing the appropriate condition for constructive interference [5]. In order to obtain visible or near infrared (NIR) light oscillating inside a resonator, with distinguishable resonant frequencies produced by alternating integer multiples of the wavelength, the size of the resonator has to be in order of micrometers, which can be named as a microresonator.

One method to create a microresonator is to fabricate a circular path for the light, where light can travel via total internal reflection. Evanescent field can be used to couple light into such a cavity, and depending on the geometry and the quality of the fabrication, once coupled, light an remain in the cavity oscillating for a long time, when the lifetime of a photon is considered. This phenomenon, known as whispering gallery mode (WGM), is obtained in microresonators with a circular path [6].

There are two main parameters that determine the efficacy of WGM type microresonators, which are quality factor (Q) and the mode volume (V). Q determines how long the light will keep oscillating, and is directly related with all the loss mechanisms. V is the volume in which light travels. The higher Q and the lover V corresponds to the better microresonator [6].

Various geometries have been fabricated in order to attain WGM type microresonators, among which microspheres and microtoroids have the best characteristics. This is related to the fact that these microcavities are produced by surface tension created when the material they are formed of; i.e., silica, is melted. This greatly reduces their surface roughness, which is the primary reason of optical power loss in WGM microresonators. [7] Both microsphere and microtoroid geometries have very high Q, in the order of 10^8-10^9; however, the mode volume of a

microtoroid is much lower, which provides many advantages besides on chip fabrication and thus easier integration to optoelectronic systems [8]. The advantage of a microsphere is that it can be fabricated much easier than a microtoroid, which requires long and detailed microfabrication processes. Different type of microresonators according to their geometry are given in Figure 1.1.

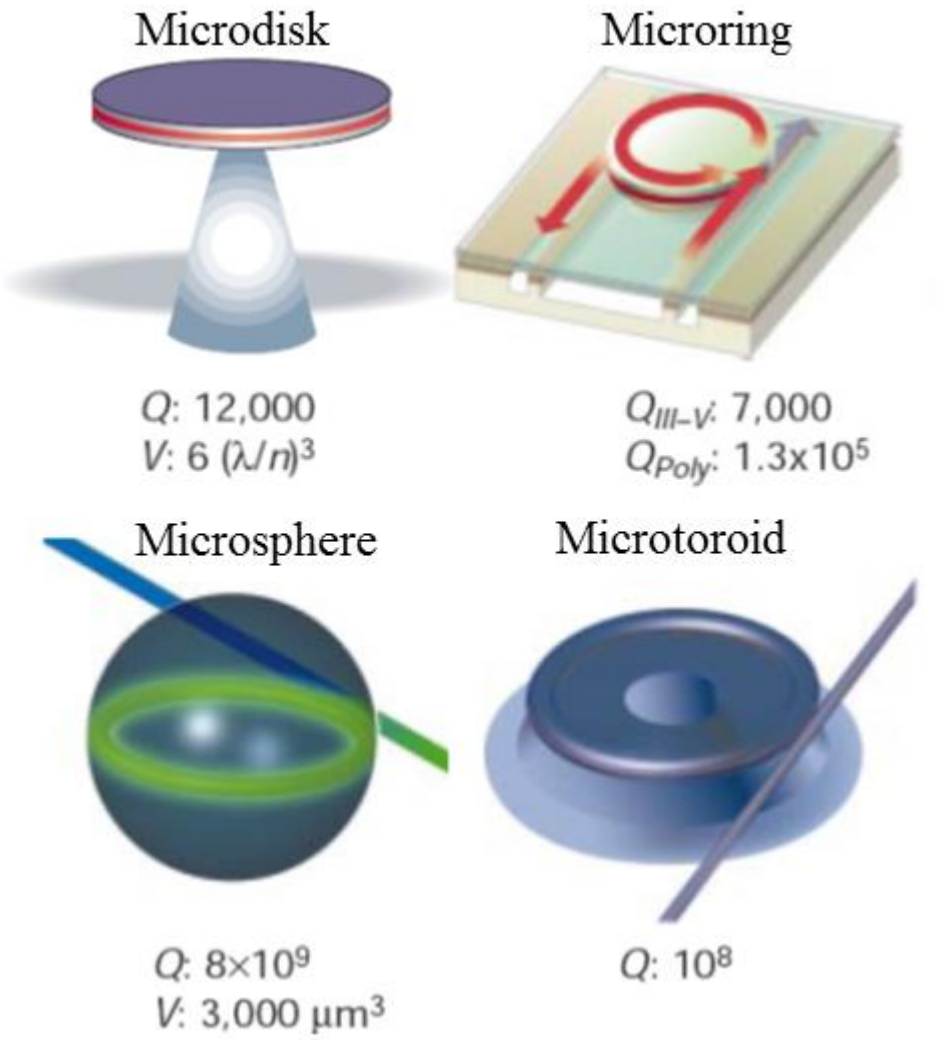

Figure 1.1: Various types of optical microcavities with their corresponding Q and V. [6] Surface roughness is the primary source of the optical loss, determining the Q.

Microresonators, especially when equipped with high quality factors could be utilized as sensors with ultra-high sensitivity. Especially for biological sensing applications, microresonators provide incredible opportunities, including single molecule sensing [9]. Therefore, intensive research is being conducting in order to develop novel sensors using microresonators.

The ultra-sensitive sensing capability of the high Q microresonators depends on the perfect confinement of photons inside the cavity. Actually, biological samples have similar refractive index to the material that the microresonator have been fabricated, and the binding of even a single target entity with specific or non-specific interactions on the microresonator alters the path in which light travels, shifting the resonant wavelength towards red. The amount of the shift is proportional to the quantity of the interaction [10]. Since each photon inside the microresonator travels inside the resonator millions of times, this leads to a cumulative effect that enables the detection of even single molecule binding events.

Although nonspecific binding of the target readily occurs onto the material which the microresonators are fabricated, which is silica most of the times, the surface of these microresonators can be chemically modified in order to attain specificity. Modified surfaces containing detection probes such as antibodies provide highly sensitive biological and chemical sensors.

There are several important examples of biological sensors developed by utilization of the shift of the WGM of microresonators. Microspheres are shown to be used for detection of DNA [11], viruses [12], and detection of conformation changes of proteins coated on the microspheres are also demonstrated [13]. In another study, microtoroid sensors are shown to detect single protein binding events [14]. Figure 1.2 shows examples of WGM type microresonators as biosensors.

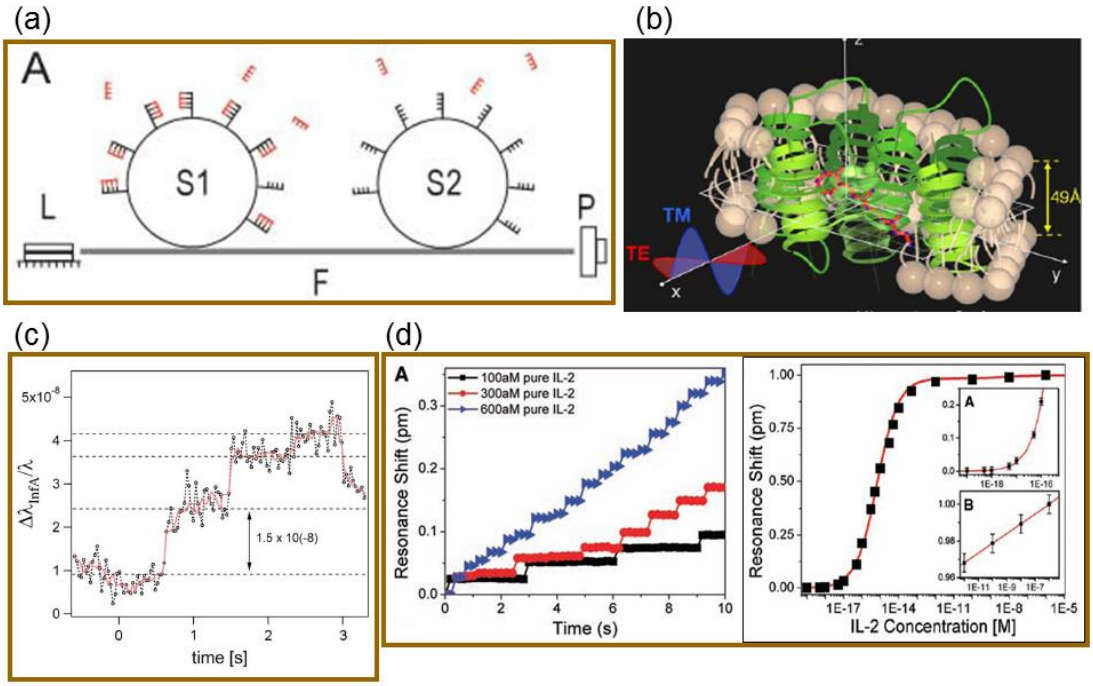

Figure 1.2: Examples of biosensing with WGM type microresonators. (a) Detection of DNA single strands with microspheres functionalized with their complementary DNA. This sensor is capable of distinguishing single nucleotide polymorphisms. [11] (b) Detection of conformational changes of bacteriorhodopsin protein assembled over a microsphere. Bacteriorhodopsin contains the chromophore retinal, which changes conformation upon exposure to light. This leads a conformation change in bacteriorhodopsin, which could be detected as a shift in resonant wavelength. [13] (c) Single virus detection using microspheres. [12] (d) Detection of IL-2 protein using microtoroids, the time scale and the associated concentration-resonant wavelength shift graph. [14]

Figure 1.3 shows a schematic representation of biodetection with toroidal microresonators with an appropriate surface chemistry.

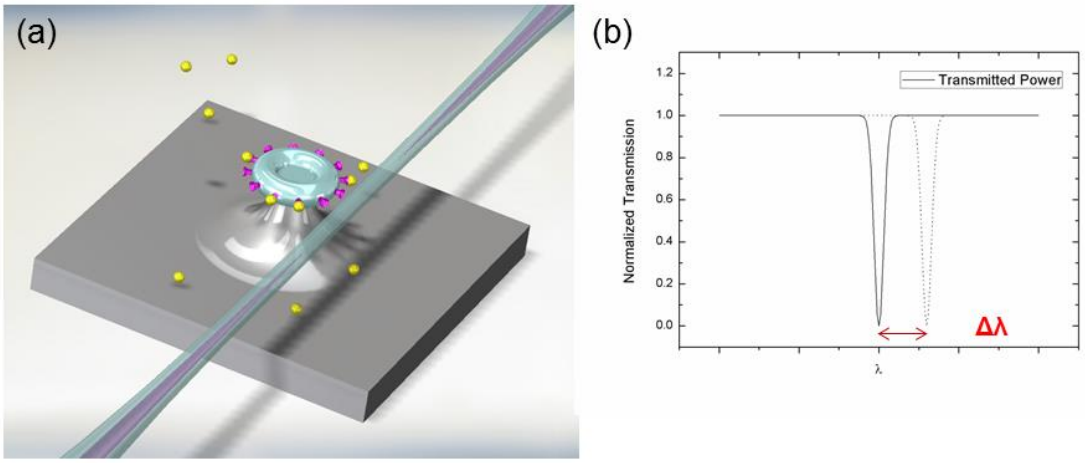

Figure 1.3: Schematic representation of biosensing with a toroidal microcavity. The interaction of the analyte with the microtoroid surface via targeting probes creates a shift in the resonant wavelength, which could be tracked in order to detect the amount of the interaction.

Specificity is definitely as critical as sensitivity when a sensor is considered, since lack of differentiation of the target from any other species, namely false positives, could be as misleading as false negative results, which are related to the detection limits. Provided that the ultimate detection at single molecule level, by elaborate utilization of various targeting probes and an advanced level of surface chemistry, has been attained using microresonators, the remaining challenge is to increase the specificity of the detection, in order to enable these optical microcavities to be utilized as sensors reliably.

The specificity issue remains ambiguous in the literature, which can be tolerated since the field is rather new, and study in order to transform these highly sensitive sensors into detection tools with also high specificity will probably have important impact in related area. Surface chemistry have been enabling novel methods for highly specialized functional surfaces, and utilization of the surface modifications could enable the realization of high specificities associated with better sensors. Therefore, research on surface modified microresonators for simultaneously high sensitivity and specificity biological sensing could be considered as an important area of study.

Chapter 2

Fabrication of Toroidal Microcavities

2.1 Photolithographic Patterning

The fabrication of microtoroids begins with patterning of substrates with photolithography. During this research, 4 inch silicon wafers with thermal oxide layers grown on their top were utilized, and various oxide thicknesses were evaluated (University Wafers and Addison). The best fabrication results were obtained with an oxide thickness of 2 μm. Before photolithography, wafers were diced into 20 x 20 mm squares using a dicing saw (Disco), and each square chip was treated independently. After the substrates were cleaned with acetone, isopropanol and deionized (DI) water, respectively, they were spin coated first with HMDS at 4000 rpm for 45 s with a spin coater (Laurell), and then with the photoresist, AZ4533 again with the same parameters, to obtain a nominal photoresist thickness of 3.3 μm. Following a soft bake at 110 °C for 50 s on a hot plate, the photoresist was patterned using a 5 $inch^2$ chromium patterned mask containing circular features, drawn with the commercial software L-Edit, and produced by a mask writer (Heidelberg Instruments). The exposure dose is 80 mJ/cm^2, where also the proximity mode of the mask aligner (EVG620) is used with a proximity of 200 μm, in order to minimize the nanometer scale non-uniformities in the circularity, exploiting the diffraction of light at far field. After the exposure, the photoresist was developed using AZ400K developer with a

developer:H_2O ratio of 1:4, for approximately two minutes. Following inspection of the disks with an optical microscope (Zeiss), the circular photoresist patterns were hard baked at 120 °C for 50 s (Figure 2.1).

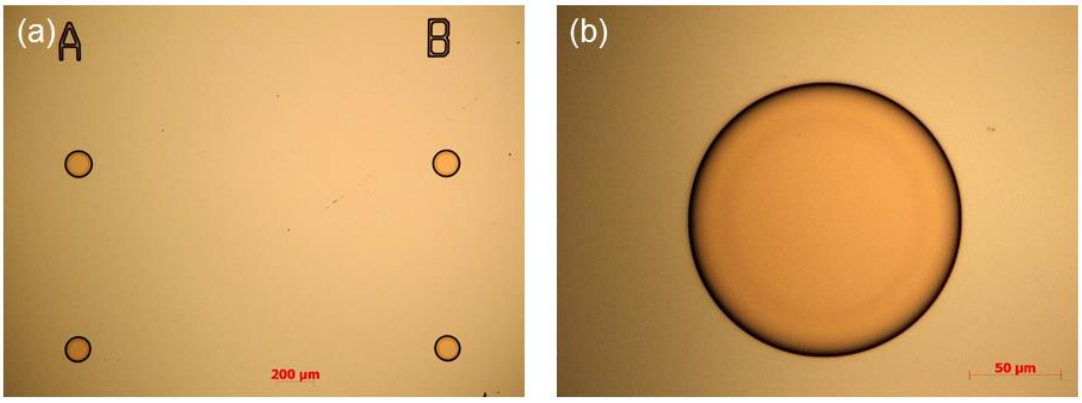

Figure 2.1: Optical microscopy images after the photolithography. (a) Image taken with a 5X objective. (b) Image taken with a 50 X objective. This perfect circularity could be attained with the proximity mode of the mask aligner.

2.2 Formation of Microdisks by Wet and Dry Etching

Microtoroid fabrication process requires the etching of both the thermal oxide layer and the silicon substrate, where selectivity is the most important issue. The silicon oxide could be etched either by wet or dry etching methods, and both methods have their advantages and disadvantages. Inductively coupled plasma (ICP) etching could be used in order to have very anisotropic etch of the oxide. In this procedure, O_2 (30 sccm) and CHF_3 (100 sccm) gases are used with the forward coil power of 250 W and forward platen power of 30 W using a low frequency RF platen (380 kHz), at 50 mTorr using an ICP etch system (STS). The drawback of this method is that the etch rate is quite low (*ca.* 20 nm/s), and prolonged exposure to plasma damages the photoresist during etching. Wet etching, on the other hand, is performed with a 7:1 mixture of NH_4F:HF, buffered oxide etch (BOE), where ammonium fluoride provides a buffer for hydrofluoric acid and prevents it from reacting with the oxide vigorously, in which the

photoresist is damaged by fast emission of gases during the chemical reaction. However, since this is an isotropic process, a wedge shape occurs, which becomes more apparent when the oxide thickness increases. After an optimization of these processes, we decided to use buffered HF for the etching of the oxide layer. The etch rate was *ca.* 60 nm/min, and the substrate with 2 µm oxide thickness was etched for 35 min to reveal silica disks over the silicon.

The next step was the isotropic etch of the silicon in order to obtain silica disks standing on silicon pillars. Prior to this step, the wafers were diced once more to obtain rectangles with sizes of 2 mm x 20 mm, each having a column of microdisks with varying sizes, in order to facilitate the coupling of light with a tapered fiber, and also more efficient use of microtoroids during surface treatment. ICP with SF_6 gas (130 sccm) was used with coil forward power of 600 W and platen forward power of 8 W with a high frequency RF platen (13.56 MHz), at 50 mTorr. The vertical etch rate was measured as *ca.* 1 µm/min, while the lateral etch rate was observed to be *ca.* 0.5 µm/min. The optimized etch time was found to be 22.5 min, because shorter etch times led to the formation of microdisks with short undercuts that make them harder to reflow, while longer etch times created microdisks with non-uniformities in their pillar circularity, which causes problem in subsequent toroid shape. This could be explained by the fact that longer etch times damages the photoresist, and since SF_6 plasma has a low selectivity for silica over silica, it harms the edges of silica microdisk, affecting the isotropicity of the silicon etch. XeF_2, which has an extremely higher $Si:SiO_2$ selectivity is often used for this process [15], while we observed that SF_6 plasma created comparable results.

As a last step, the remaining photoresist is cleaned by using a mixture of O_2 (30 sccm) and N_2 (5 sccm) with 400 W RF power at a plasma cleaner (Asher) for 45 min. The scanning electron microscopy (SEM) (FEI Nova NanoSEM) images of the microtoroids are given in the Figure 2.2. In order to facilitate imaging from the sides, a SEM stub with 45° tilt was used, and the SEM stage was further tilted.

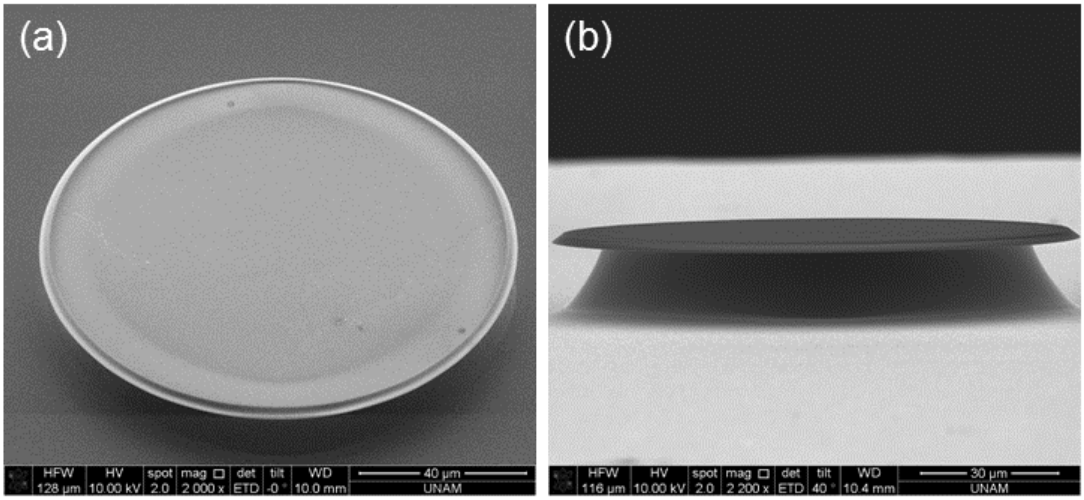

Figure 2.2: 45° and side view of the microdisks after ICP etch. (a) 45° view of a fabricated microdisk for observing the circularity. (b) Side view of the microdisk, with a total tilt angle of 85°. The Si pillar could also be observed. There is a wedge shape at the circumference of the disk, related to the isotropic nature of BOE.

2.3 Formation of Microtoroids by CO_2 Laser Reflow

The rectangular wafer containing the microdisk array is clamped vertically on a small flip 2-axis motion stage for CO_2 laser reflow. A He-Ne laser at 633 nm (Thorlabs) was used as a pilot light. The beam from a CW operating CO_2 laser at 10.6 μm (Coherent) was focused over the microtoroids using a ZnSe plano-convex lens. Typical laser powers used were within the range of 12-20 W. Laser was controlled by a custom developed software. The reflow process was monitored by a charge coupled device (CCD) camera (Hitachi) equipped with a 10X plan apochromatic long working distance objective (Mitutoyo) and Zoom 70XL Optical System (Qioptiq). After the position of the microtoroid was aligned to the beam center, as observed with the pilot light, the flip mirror was folded to enable CO_2 laser beam to interact with the microdisk. Figure 2.3 shows the reflow setup.

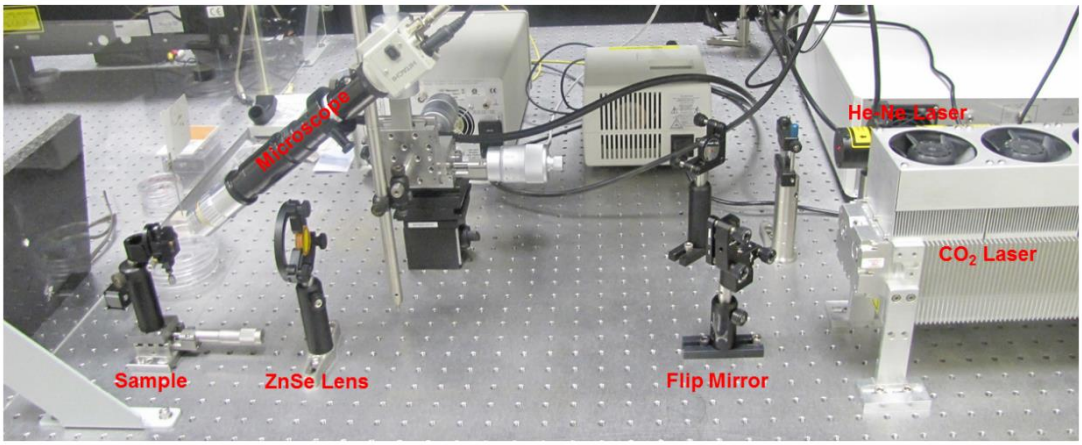

Figure 2.3: Components forming the microtoroid reflow setup.

Since silica has a much higher absorption for CO_2 laser beam with the wavelength of 10.6 µm, it creates a high temperature that causes the melting of the silica. The silicon pillar, acting as a heat sink, leads to formation of a microtoroidal shape with a very low surface roughness [8]. The SEM images of the microtoroids are given in Figure 2.4.

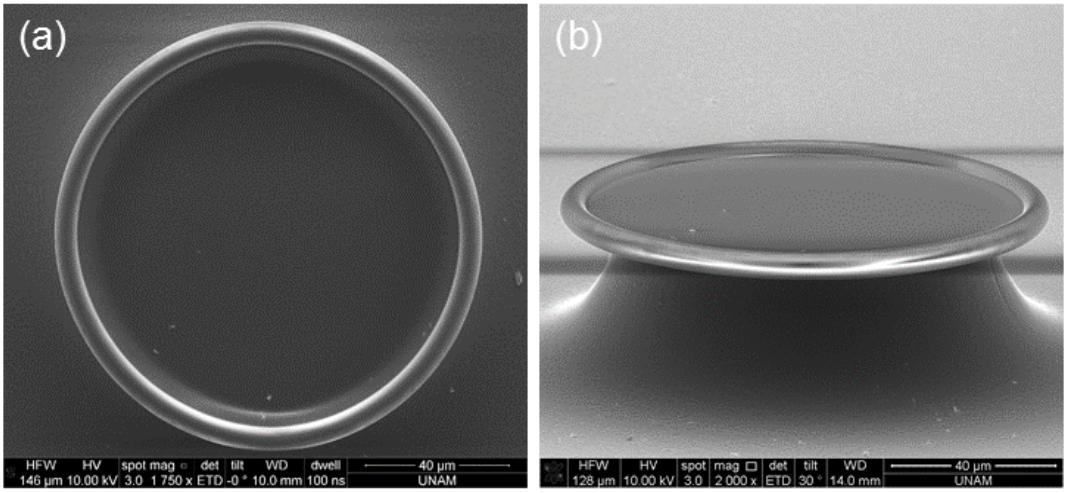

Figure 2.4: SEM images of the microtoroids. Both top and side (75° tilted) views were investigated to comprehend the toroid morphology better.

Chapter 3

Optical Coupling to Microtoroids

3.1 Production of the Tapered Optical Fibers

Among various methods for coupling light into WGM microresonators such as free space [16] or prism coupling [17], and tapered fiber coupling, tapered optical fibers are the most prominent in terms of coupling efficiency [18]. Tapered optical fibers are generally produced by heating a particular zone of the silica fiber up to its softening temperature and pulling the fiber sides towards opposite directions simultaneously. The most important characteristic of a tapered fiber is adiabadicity, which is inversely correlated to the optical loss observed after the tapering process. In an adiabatically tapered fiber, transmission values higher than 99% could be observed [19]. The adiabadicity depends on the taper length, which longer tapers provide higher adiabadicity [20]. Although it is possible to etch fibers to form tapers using silica etchants such as HF [21], the best results are obtained by heating fibers by various means. Unlike etched fibers, where only the core of the fiber remains after tapering, when the fiber is tapered by simultaneously heating and pulling the fiber apart, the core of the fiber gradually diminishes, and at the taper region where the diameter is minimum, the optical wave inside the fiber is guided only by the remaining core region [20]. In case of uniform heating, the taper profile could be deduced from the formula below:

$$r(z) = r_0 e^{-z/L_0}$$

where $r(z)$ is the radius of the fiber at the distance z, which is the distance from the tapering center, and L_0 is the length of the hot zone [20]. One important outcome of this formulation is that the taper length mainly depends on the length of the hot zone, provided that the hot zone is kept constant and uniform in terms of length and temperature.

During our research we have tested various methods for fiber tapering including HF etch, CO_2 laser heating prior to HF etch, CO_2 laser alone, propane/butane torch, and hydrogen torch. The most effective tapering was observed with hydrogen torch used as a heating source. The tapering setup used in this research, as schematically represented in Figure 3.1 consists of several optical and mechanical elements. We have coupled SMF28 optical fibers to the output of a laser operating at 1550 nm (Santec TLS-510) and to the signal input of an optical powermeter (Newport 1935C) using mechanical fiber splicers (Thorlabs). The output intensity of the laser was monitored continuously during the tapering. We used two reciprocal linear motion stages (Newport) driven by an ESP motion controller (Newport). Laser, powermeter and linear stages were controlled simultaneously by a custom built software developed in C#. The tapering process was also continuously observed by a CCD camera equipped with a 10X plan apochromatic long working distance objective.

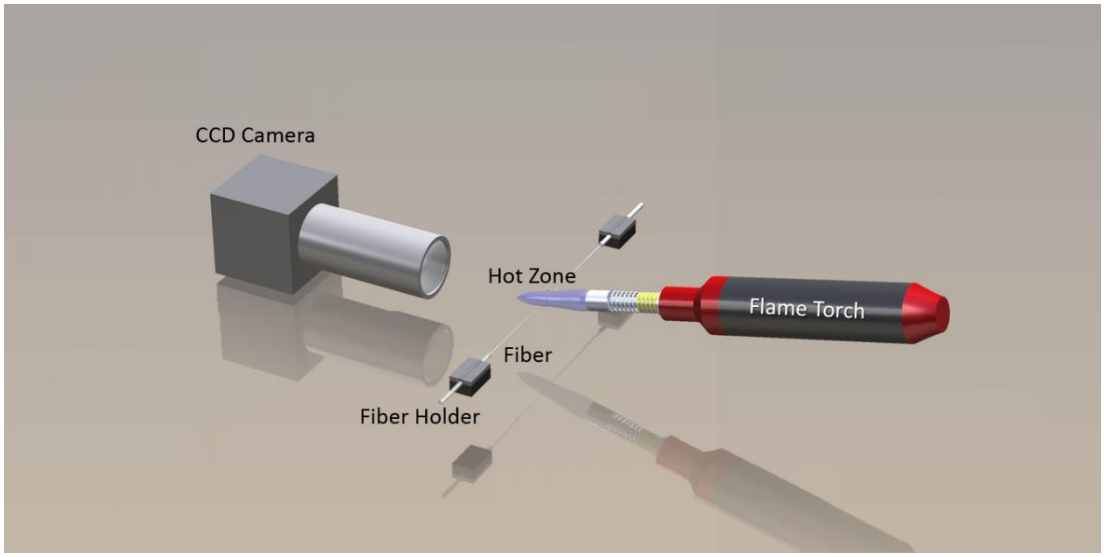

Figure 3.1: Schematic representation of the basic components forming the fiber tapering setup. The light inside the fiber is also continuously monitored.

Monitoring of optical output enables us to observe the alterations in the wave guiding characteristics during the fiber tapering process, as previously described in the literature [22]. Initially, the light travels within the core, which is single mode core-guided operating regime. During the tapering, the fiber first enters into taper multimode operating regime, and finally when the diameter approaches to the order of the wavelength, it enters into taper single mode operating regime. The fluctuations during taper multimode operating regime occurs because although the tapered region supports multiple modes, the rest of the fiber is still single mode, therefore it could not guide the modes formed at the tapered region. Figure 3.2 shows a typical fiber tapering process, where we typically obtain transmissions higher than 95% using our fiber tapering system. Figure 3.3 shows the transmission spectrum of a fiber before and after fiber tapering, demonstrating the adiabadicity of our fiber tapering process. Also, in Figure 3.4 there are SEM images of a tapered optical fiber.

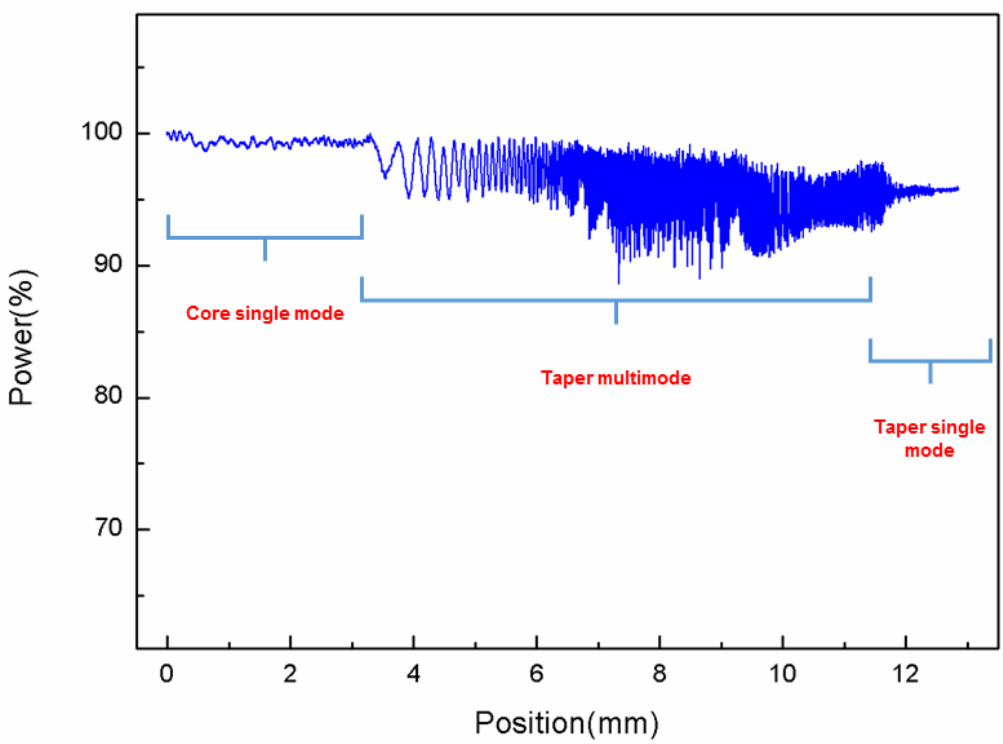

Figure 3.2: Transmission from the optical fiber during the fiber tapering. Transmission is given as a function of the change in the position of one of the motion controllers; therefore, the actual taper length is twofold.

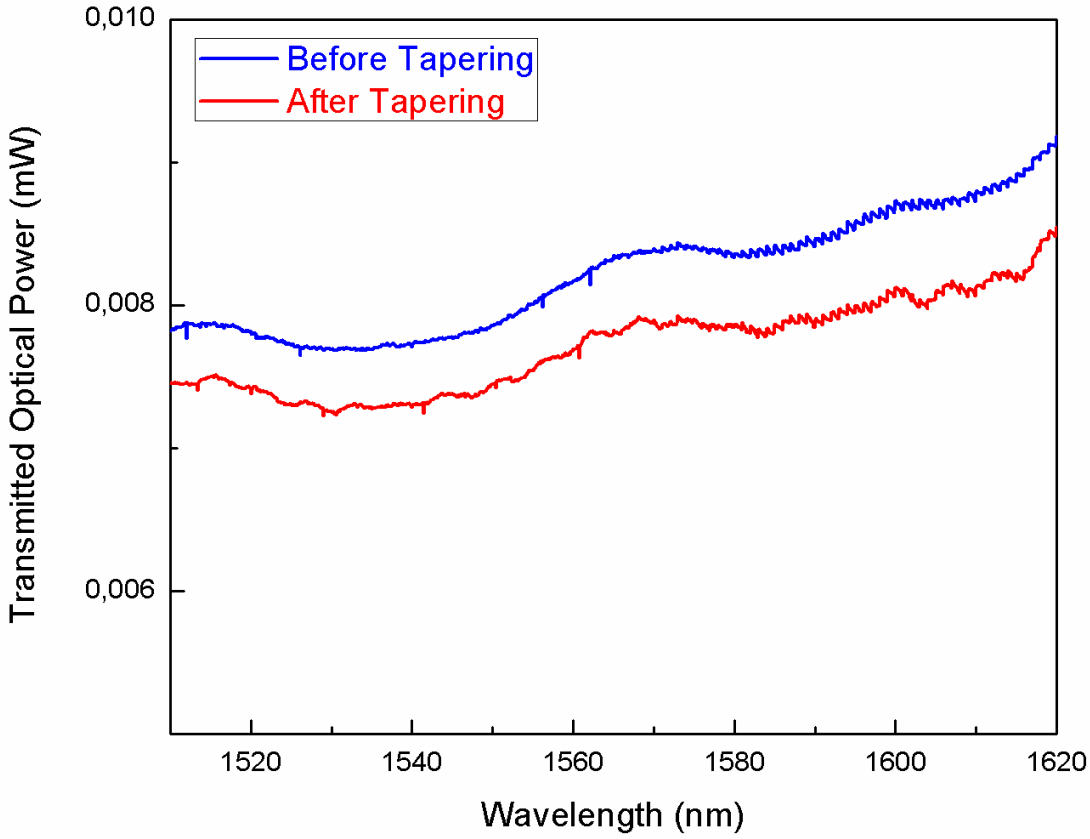

Figure 3.3: Transmission spectra of a SMF28 fiber before (blue) and after (red) the tapering process. The transmission in the tapered fiber has a similar transmission pattern with the fiber before tapering, except a loss occurring during the tapering, demonstrating the adiabadicity of the tapering process.

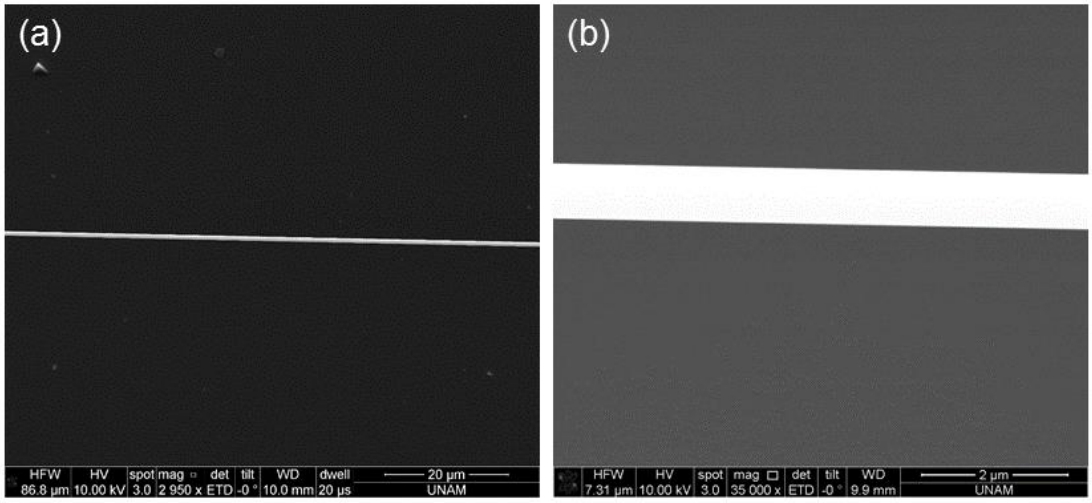

Figure 3.4: SEM images of a tapered fiber. The fiber is uniform in diameter within a large length range (a), and submicron diameters could be reached. For instance, the taper diameter here is 750 nm (b).

3.2 Optical Coupling and Measurement Setup

As mentioned in the previous section, light is coupled into microtoroids by using tapered fibers. While the light is guided through the taper region, an evanescent field traveling in the air around the fiber occurs. If this evanescent field encounters a medium with a similar refractive index, the light could be coupled into and out of the medium. When this medium is a resonator; i.e., a constructive interference of light occurs within that medium, the light is coupled into this resonator as resonant modes, which could be observed as dips in the transmission spectrum of the waveguide. Since the light travels within the microresonator as a result of total internal reflection, the constructive interference condition depends on the optical path length, which is the circumference of the microcavity, the wavelength of the coupled light, and effective refractive index of the resonator according to the following formulation [5]:

$$m\lambda_m = 2\pi r n_{eff}$$

Here, m stands for mode number, an integer that satisfies the resonance condition, λ_m is the corresponding resonant wavelength, r is the radius of the microresonator, and n_{eff} is the effective refractive index of the mode coupled into the microresonator,

depending on the propagation of light within the cavity, which differs from bulk material. n_{eff} is also essential for one of the two important phenomena regarding the optical coupling into all WGM microresonators, which are phase matching and critical coupling. Phase matching occurs when effective refractive indices of the waveguide and the microresonator have similar values. The refractive index of a waveguide having dimensions on the order of the wavelength of the light inside, similar to of a WGM microresonator, differs from the bulk material. The effective index decreases with decreasing taper diameter. The effective index of the WGM resonator, on the other hand, depends on its radius r, and it also decreases with decreasing resonator size [18]. Effective indices, therefore phase matching condition, could be calculated both analytically and numerically, and also phase matching could be determined empirically by changing the position of the microresonator with respect to taper diameter. Especially in complex geometries such as microtoroids, where there are less symmetry compared to spheres, numerical methods and empirical determination becomes more feasible. When phase matching condition is satisfied, all the optical power could be transferred within the microresonator. The second important condition regarding optical coupling to WGM microresonators is coupling efficiency, which depends mainly to the distance between tapered fiber and the microresonator, but also the taper diameter. There are three conditions that could occur with respect to coupling efficiency, which are undercoupling, critical coupling and overcoupling. The critical coupling occurs at the distance where all the optical power is transferred into the microresonator, which could also be determined experimentally [18].

The optical coupling setup used in this research consists of a tunable external cavity laser operating around 1550 nm (Santec TLS-510), a powermeter (Newport 1935C) or a 1.2 GHz InGaAs FC/PC-Coupled Photodetector, 800 - 1700 nm (Thorlabs), depending on the measurement, an oscilloscope acquiring data from analog output of the laser and powermeter or photodetector (Tetronix TDS-1012B), a 3-axis closed loop piezo stage (Thorlabs Nanomax TS) driven by a piezo controller (Thorlabs) on which an adjustable height, pitch and roll platform (Thorlabs) is mounted, and two optical microscopes enabling top and side imaging of the optical coupling. Laser, powermeter, and oscilloscope were controlled by a custom built software developed in C#, while

piezo controller could be used either manually or with the same software as well. The laser was tuned continuously within a predefined wavelength range between 1510 and 1620 nm, with a constant sweep rate that could be varied from 1 nm/s to 100 nm/s, and the voltage signal depending on the amount of tuning was tracked by the oscilloscope. The other channel of the oscilloscope simultaneously tracked the voltage signal from the powermeter, and the software recorded and also plotted these signals. The schematic representation of the optical measurement system is given in the Figure 3.5, and the images of a coupled microtoroid, as well as coupling observed with an infrared (IR) camera (Xenics) connected to our microscope system is given in Figure 3.6.

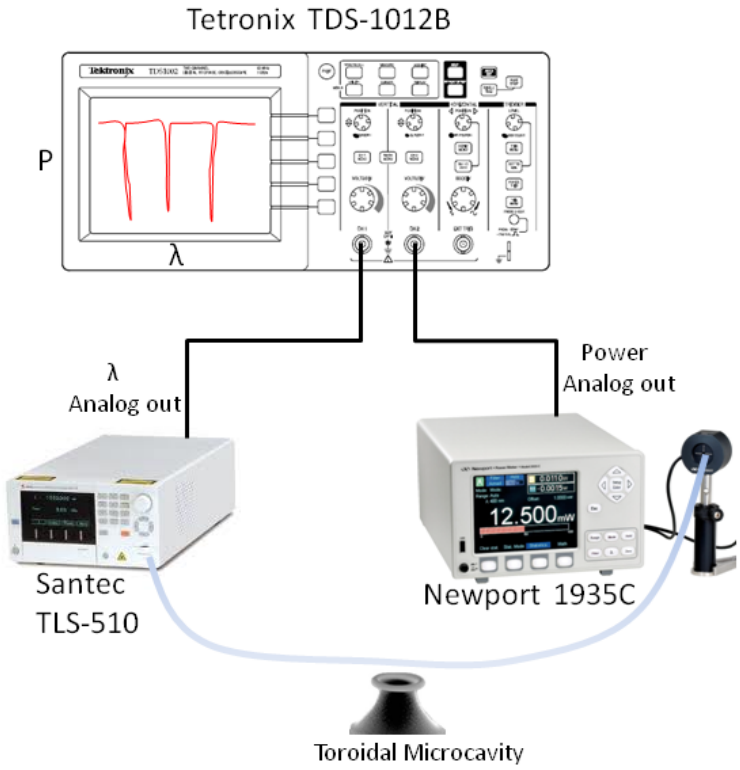

Figure 3.5: Schematic representation of the optical measurement setup. The components are used simultaneously with a custom software to capture and record data.

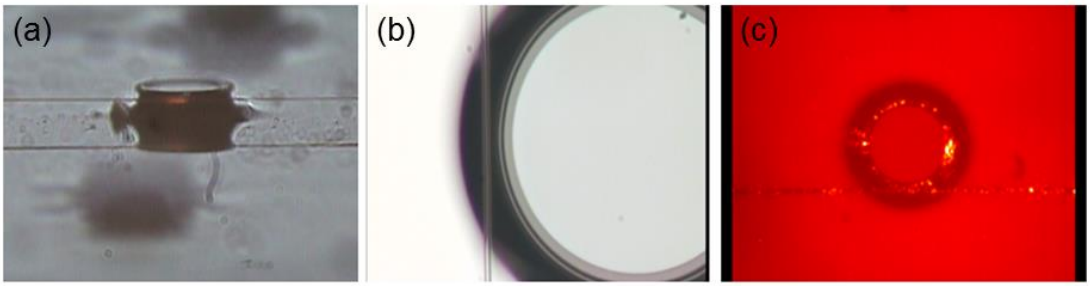

Figure 3.6: Imaging optical coupling. Side (a) and top (b) views of optical coupling to microtoroids are given. Also, with the help of an IR camera, the optical coupling could be visualized.

3.3 Observation and Analysis of Whispering Gallery Modes

As mentioned above, the coupling into the microresonators occurs as resonant modes, which depend on the interference condition. The polarization of the light is also important, and various TE and TM modes could be controlled by a manual polarization controller (Thorlabs FPC030). When a large wavelength range is scanned for optical resonances, a definite pattern of whispering gallery modes could be observed. The mode spectrum consists of these repeated patterns, separated by a distance denominated as free spectral range (FSR) and calculated as following:

$$FSR = \frac{\lambda^2}{2\pi r n_{eff}}$$

Each pattern represents an individual resonance condition, determined by consecutive values of the integer m [23]. Provided that a plane polarized light is coupled into the microresonator, which could be accomplished by the polarization controller, several resonances could be observed in each pattern, representing modes of different orders. One distinct advantages of the microtoroids is that most of the higher order modes are suppressed due to the geometrical restrictions compared to

spheres. Figure 3.7 shows a spectrum of a microtoroid with several mode patterns separated by FSR, and a spectrum of a set of modes of different orders at perpendicular polarizations controlled by the paddle acting as a half wave plate. In order to minimize the instability caused by thermal effects, the power of the laser was kept at the order of nWs.

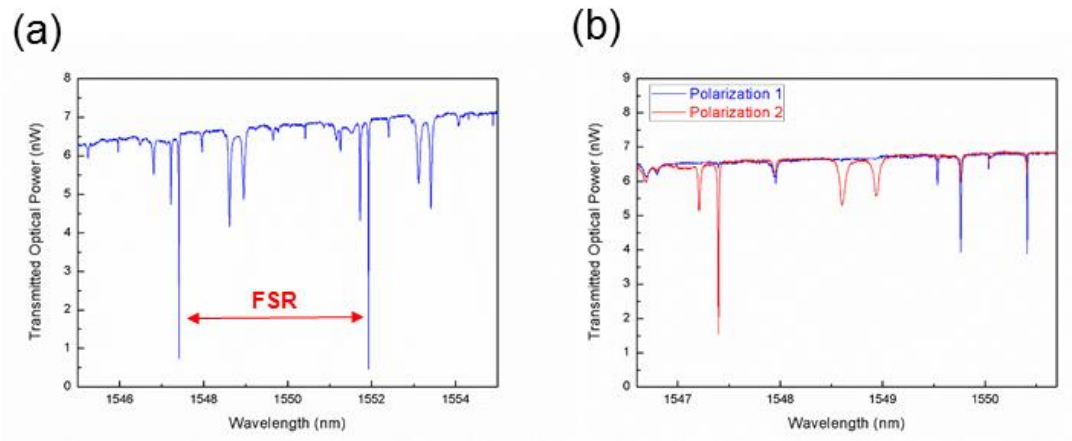

Figure 3.7: Optical spectrum of coupled light into the microtoroids. (a) There are consecutive mode patterns separated by FSR. (b) Perpendicular polarizations show different resonance patterns.

When each resonance dip is investigated individually, they provide another important information regarding the microresonator, which is the quality factor (Q). Q represents the amount of power that could be stored within the cavity. With an increasing Q, the full width half minimum ($FWHM$) of the resonance becomes smaller, and the relation between Q and $FWHM$ could be described as below [12, 24]:

$$Q = \frac{\lambda}{\Delta\lambda}$$

where $\Delta\lambda$ represents the $FWHM$. While there are other more precise methods for measuring Q such as cavity ring down [8] or ringing [25], the formula above provides a reasonable estimate.

Although laser is tuned around the resonance continuously to observe WGM resonances, since the oscilloscope collects discrete data points, it is necessary to fit the data, which could be fitted to a Lorentzian function [26-28]. Physically, the

transmission intensity from the tapered fiber around a WGM resonance could be calculated accurately from the Lorentzian of the angular frequency ω as:

$$F(\omega) = T_i - \frac{A}{(\omega - \omega_0)^2 + (\frac{FWHM}{2})^2}$$

where T_i is the optical transmission without optical coupling, A is the amplitude parameter of the coupling, and ω_0 is the resonant frequency. Since this function is in the frequency domain, $FWHM$ should also be considered in terms of frequency. Yet, although not exactly Lorentzian, because the relation of λ with ω is not linear as shown below:

$$\lambda = \frac{2\pi c}{\omega}$$

the shape of the resonant mode in transmission spectrum in wavelength domain still resemble a Lorentzian function; therefore, the equation used in the calculations was:

$$F(\lambda) = T_i - \frac{A}{(\lambda - \lambda_0)^2 + (\frac{FWHM}{2})^2}$$

where λ_0 is the the resonant wavelength. In this notation, $FWHM$ is also in the terms of λ.

By a script performing nonlinear regression in MATLAB, it is possible to perform Lorentzian fit numerically and obtain the value of Q (Figure 3.8). As calculated from this Lorentzian fit, Q is 3.95 x 10^6.

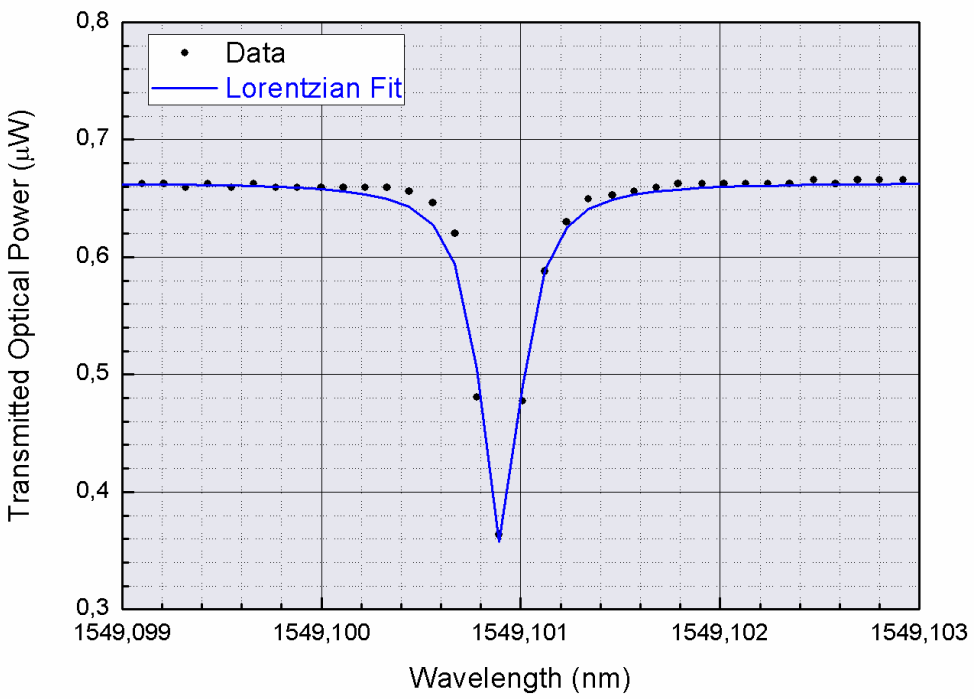

Figure 3.8: A high resolution scan of a single resonant mode. A Lorentzian fit of the mode is also given in the figure.

By using our optical coupling setup, we could observe WGM resonances of not only microtoroids, but also other type of WGM resonators. One prominent example is coupling of light into on chip chalcogenide microcavities, recently demonstrated by our research group. Silica tapered fibers were used to couple light into spherical As_2Se_3 microresonators with size below 100 μm; although the phase mismatch with low order modes caused observation of only higher order modes, which could be phase matched with the mode coupled into the tapered fiber. Yet, the quality factors measured were on the order of 10^5 with those chalcogenide microcavities [29].

Chapter 4

Surface Chemistry for Biosensing with High Selectivity

4.1 Surface Chemistry for Simultaneously Protein Resistant and Bioconjugable Surfaces

One of the most important aims of this research was to develop a biosensing strategy capable of reducing nonspecific interactions substantially. For this reason, a novel surface chemistry strategy was designed and evaluated.

Physical and chemical modification of surfaces enables unprecedented manipulation of the characteristics of materials [30]. Numerous functionalities could be implemented by a myriad of techniques to virtually all kind of solid surfaces, among which anti-fouling and bioconjugable interfaces are quite prominent, because of their large applicability in both everyday life and state-of-the-art research, including anti-

fouling implants [31], self-cleaning surfaces [32], high sensitivity and selectivity biosensors [33], biocompatible nanoparticles [34], and targeted drug delivery [35]. Although these fields of research are quite mature regarding production of efficient, convenient and cost-effective surfaces with desired characteristics, there is still a considerable effort for optimizing the current techniques and asserting novel ones, in order to quench continuously increasing demands of emergent materials science.

Chemical modification of surfaces could be attained by a virtually indefinite number of different compounds; however, regarding the accommodation of these substances over the surfaces, self-assembly strategies depending on spontaneous interaction of molecules with the surface for formation of mono- or multilayers are frequently utilized [36]. Self-assembly generally occurs via functional head groups, which have high affinity towards the substrate, anchoring the molecule covalently or non-covalently to the surface. Among various different head groups, thiols and silanes are particularly important and widely used. Thiol based modification is well characterized especially for gold, but they are also applicable for other metals such as silver, copper or palladium [37]. One major advantage of thiols is that, although the nature of the ligand-surface interaction is still under debate, the assembly kinetics of these molecules are well defined, enabling production of monolayers almost precisely defined in composition [38]; i.e., in function as well. Silanes, on the other hand, are much difficult to anticipate in terms of assembly over silicon based surfaces. They are most of the times assumed to form monolayers, which are stronger that their thiol counterparts, but the knowledge regarding their assembly is far more empirical, although practical. This process is also highly dependent on the environmental conditions, obstructing formation of films with well-defined characteristics [39].

Having a coating with more than one function simultaneously thus represents a challenge, especially for silane based molecules, since the characteristics of the coating heavily depend on both the tail and the functional group, where an alteration in one directly affects the nature of the whole coating. Polyethylene glycol (PEG) based molecules are the gold standard in especially protein resistant coatings, where almost zero adsorption could be attained, depending on the density [40], chain length and the functional group [41]; however, inducing a different functionality eventually alters their characteristics. Coating with more than one molecule is hypothetically possible, either simultaneously or sequentially, but although it has been shown to effectively function with the thiols [42], due to the easy polymerization and unpredictable assembly behavior of silanes, it is not practical to perform in every case [39]. Another strategy is selective patterning of surfaces via lithographic methods enabling production of surfaces with different functionalities [43, 44]. In this case, multifunctional surfaces are possible to obtain, but this does not solve the issue of nonspecific interactions particularly at the patterned site, and these techniques are limited with the sizes of the current microfabrication tools, which are at most wafer scale.

Here we propose a different strategy for realizing anti-fouling surfaces with bioconjugation capability by using only a single molecule for surface coating. We utilize a commercial small silane-based molecule having a methylphosphonate group, and show that it is suitable for producing bioconjugable anti-fouling silica surfaces. Phosphonates have frequently been used either as head groups for conjugating self-assembly monolayers over metal oxide surfaces [45, 46], functional groups stabilizing silica containing nanoparticles against aggregation [47, 48], and sites for covalently

anchoring primary amines to other molecules [49], especially to nucleic acids [50, 51]. Also, it has been shown previously that methylphosphonate containing silica nanoparticles exhibited significantly reduced non-specific biological interactions [52], and our research group has recently demonstrated that methylphosphonate conjugation particularly decreased protein adsorption on silica nanoparticles [53]. However, to our knowledge, neither the physical and chemical characteristics of these phosphonate-based films were investigated in detail, nor were their bioconjugation properties utilized together with their protein resistant characteristics. Here, we developed a method to coat silica surfaces efficiently with methylphosphonate containing small organosilane molecules, and experimentally characterized the formed thin organosilane film. We have also examined these films regarding their protein resistance and bioconjugation characteristics. Our results show that methylphosphonate containing organosilanes could effectively be used for producing simultaneously bioconjugable and protein resistant silica surfaces in a facile manner, as shown in Figure 4.1.

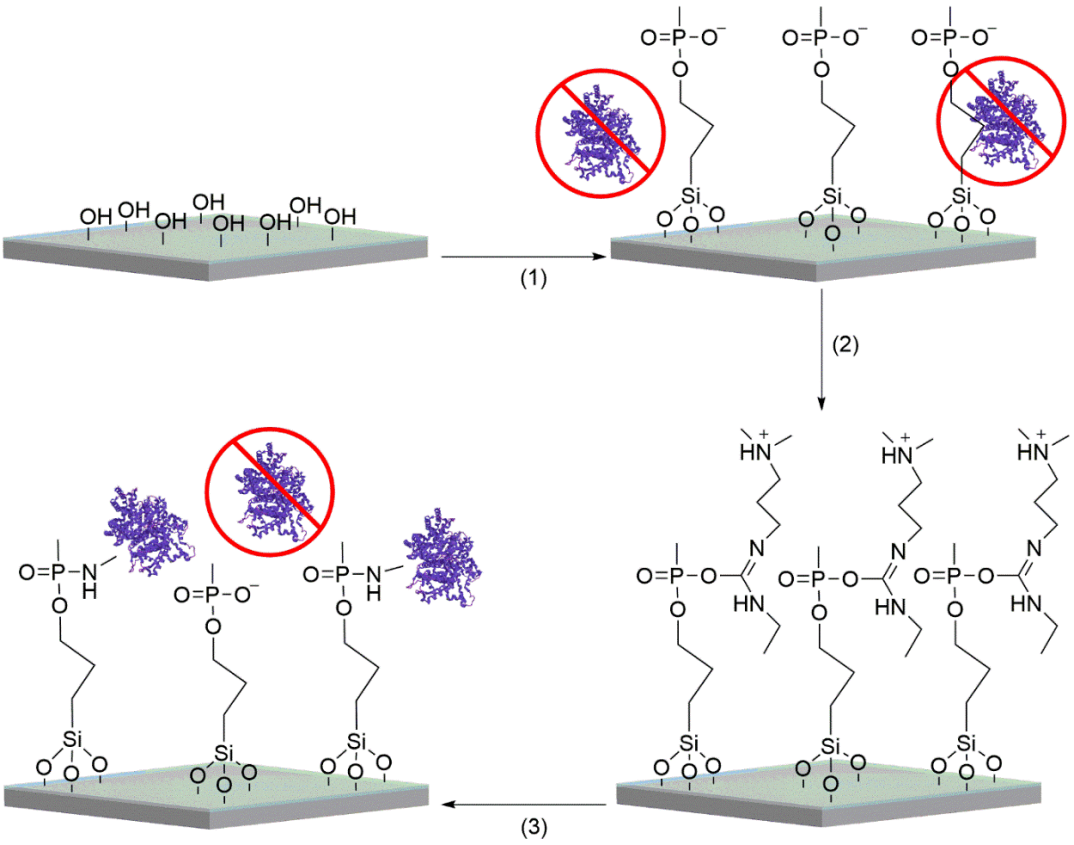

Figure 4.1: Schematic representation of formation of simultaneously bioconjugable and protein resistant coating over silica. Piranha activated silica surface is first treated with methylphosphonate containing silane (1), which forms a protein resistant thin film. Methylphosphonates could be activated temporarily by using a cross-linker molecule (2). After the covalent attachment of proteins from their primary amines via these activated moieties (3), the coating reverts to its bio-inert state, besides being functionalized.

4.2 Coating and Characterization of Silica Surfaces

Silicon wafers with thermal oxide of various thicknesses were cut into pieces using a dicing saw (Disco). They were cleaned with 1% v/v Hellmanex (Hellma-Analytics) solution in water in an ultrasonic bath for 15 min. Then, the surfaces were washed with DI water and sonicated in ethanol, acetone and DI water each for 15 min, respectively. The surfaces were then dried in vacuum for 30 min at 100 °C. To remove residual organic contaminants and increase the number of active hydroxyl groups on the surfaces, piranha cleaning was applied (Caution! Piranha solution is highly reactive

and should be handled with care in a fume hood). After cleaning with piranha solution (H_2SO_4:H_2O_2 3:1 v/v) at 60 °C for 30 min, the surfaces were washed with water and dried with a nitrogen gun.

A 2% v/v 3-(Trihydroxysilyl) propyl methylphosphonate (THPMP, MW 238.18, Sigma-Aldrich) solution in ultrapure water was prepared and left on a shaker for 10 min at room temperature. The dried surfaces were soaked immediately into the THPMP solution and organosilane modification of the surfaces were done for 1h at 60 °C. Then, the surfaces were washed gently with ultrapure water to remove unbound THPMP molecules, and cured in vacuum for 1h at 100 °C.

After coating the silica surfaces with THPMP, we conducted XPS analysis to characterize the coating. XPS measurements were done with a high resolution XPS spectrometer (Thermo Fisher Scientific). As X-Ray source, Al K-α X-Ray monochromator (0.1 eV step size, 12 kV, 2.5 mA, spot size 400 µm) was used at an electron take-off angle of 90°. For all samples, survey spectra were taken 2 times with 50 ms dwell time (pass energy 200 eV). All N1s, O1s, C1s and Si2p spectra were taken 10 times with 50 ms dwell time (pass energy 30 eV). In order to increase signal and minimize the noise from background, all P2p spectra were taken 20 times with 200 ms dwell time (pass energy 30 eV). Peak calibration and peak fitting were done with Avantage software package. Binding energy scales were calibrated with respect to neutral C1s peak at 284.8 eV [54-56]. For peak fitting, background type and function type were chosen as ‘Smart’ and ‘Gaussian-Lorentzian mix’, respectively. During all XPS studies, 1 µm thermally grown oxide on Si wafers, cut into 5 x 5 mm pieces, were used.

As could be seen from the survey XPS spectra (Figure 4.2), P2p signal at 133.2 eV only arises from the THPMP coated sample, showing existence of P over the surface. Due to the fact that low abundance of P on the surface, P2p signal is much lower compared to that other elements have (Table 4.1).

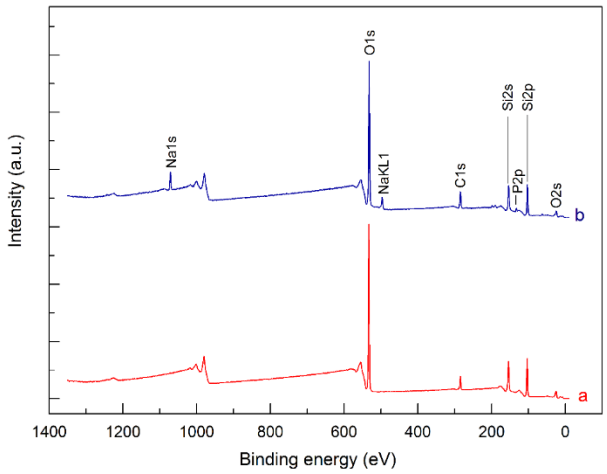

Figure 4.2: XPS survey spectra of the bare (a) and THPMP coated (b) silica surfaces.

		Peak binding energy (eV)	FWHM fit param (eV)	Atomic percentage
BARE SILICA	P2p	-	-	0
	Si2p	103.6	1.5	32.5
	O1s	532.9	1.4	55.5
	High C1s	284.8	1.5	11.1
	Low C1s	286.5	1.3	0.9
THPMP COATED SILICA	P2p	133.2	2.0	2.8
	High Si2p	103.6	1.6	24.8
	Low Si2p	102.1	1.4	1.3
	High O1s	532.9	1.4	47.0
	Low O1s	531.1	1.5	4.1
	High C1s	284.8	1.5	14.1
	Low C1s	286.5	1.2	2.8
	Na1s	1071.5	-	3.1

Table 4.1: XPS results of the bare and THPMP coated silica surfaces.

Figure 4.3 represents the comparison of high resolution XPS scans of P2p, Si2p, O1s and C1s regions for bare and THPMP coated silica surfaces. XPS spectrum of bare silica is known to possess single peaks for both silicon and oxygen, while functional group related new peaks emerge after organosilane modification [54], which is coincident with our data. As seen in the Si2p scan of the bare silica surface, a single peak at 103.6 eV is from oxygen-rich Si binding environment [57]. The THPMP coated silica shows an additional peak, located at 102.1 eV, suggesting a C–Si–O bonding [58]. This peak with lower energy verifies that a slightly carbon-rich environment is induced on the Si surface due to THPMP bonding. Additionally, O1s scans of the bare and THPMP coated silica surfaces show a common peak located at 532.9 eV. This peak arises from thermal oxide [59]. After the THPMP coating, a lower energy peak located at 531.1 eV appeared. This peak shows Si–O bonding [54] between THPMP molecules and the silica surface. C1s scans of the bare and THPMP coated silica surfaces show two common peaks at 284.8 and 286.5 eV, which are attributed to C–C bonding and C–O bonding [60], respectively. The intensity of the lower energy peak at 286.5 eV increases significantly after the THPMP coating due to covalent bonding of the THPMP molecules over silica surface.

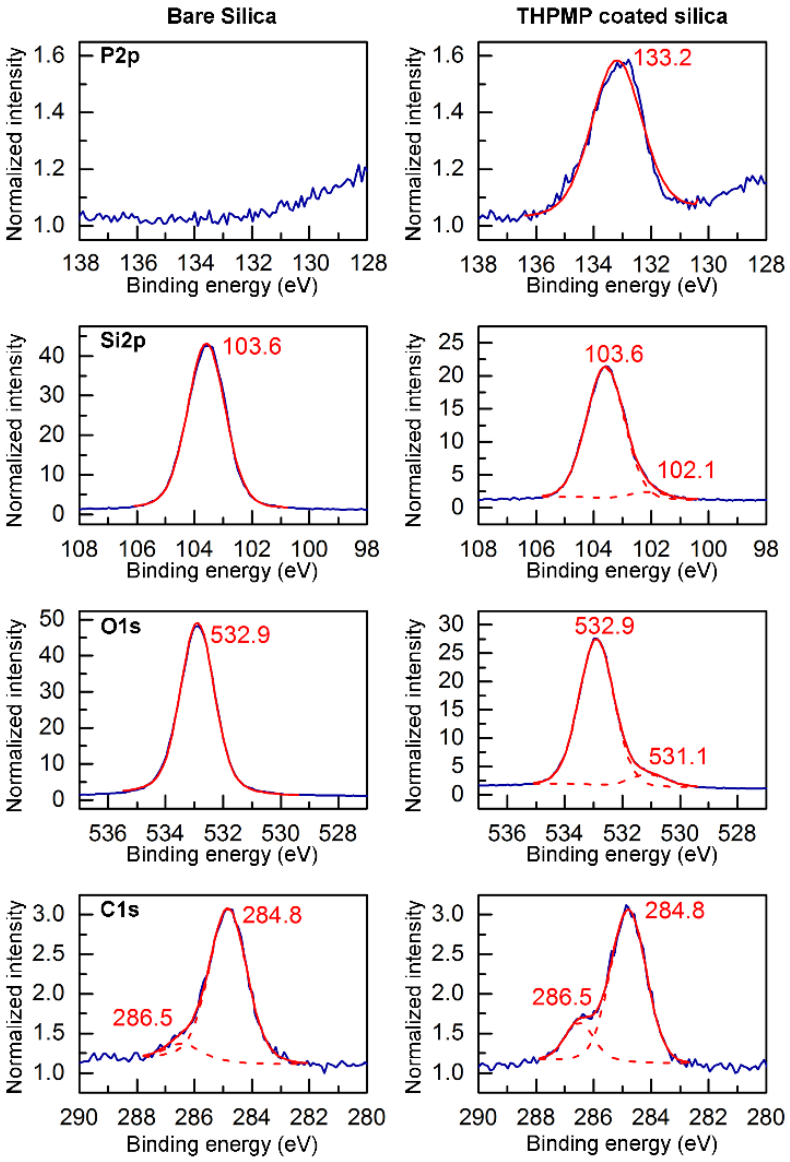

Figure 4.3: Comparison of high resolution XPS scans of P2p, Si2p, O1s and C1s regions for bare silica and THPMP coated silica surfaces. Original data were given in blue lines, while fits for single peaks and envelopes were given in dashed and solid red lines, respectively.

Static contact angle measurements were done with a contact angle meter (OCA-30, Dataphysics, Germany). Each measurement was done with 3 µl water droplet and repeated three times with different wafers at room temperature. Laplace-Young fitting was done to obtain contact angle values. All contact angle measurements were performed on 1 µm thermally grown oxide on Si wafers. For piranha cleaned and

THPMP coated samples, we used wafers cut into 2 x 2 cm and 0.5 x 0.5 cm, respectively. Contact angle measurement of a piranha cleaned surface revealed contact angles of ~3°, since the surface became highly hydrophilic after the piranha treatment (Figure 4.4). After the THPMP coating, the surface gained a static contact angle of 49.4±2.0° (Figure 4.4b) indicating the existence of a moderately hydrophilic methylphosphonate containing thin film over the silica surface. Additionally, in another study it was indicated that contact angles of ~50° had been observed at hydroxyl terminated and compact monolayers of phosphonate coatings [61].

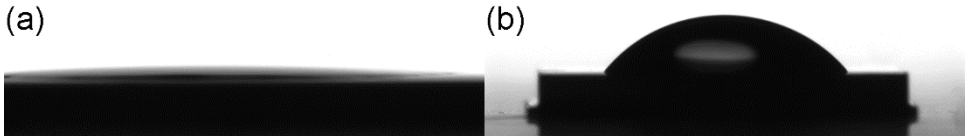

Figure 4.4: CCD camera images of water droplets on the (a) piranha cleaned silica surface (2 x 2 cm) and (b) THPMP coated silica surface (0.5 x 0.5 cm) at room temperature. Droplet volume was 3 µl for both samples.

To observe surface morphology and measure root-mean-square (rms) surface roughness, AFM (XE-100E, PSIA, Korea) was used in non-contact mode at 0.65 Hz scan rate during all measurements. For each measurement, 1 x 1 µm area was scanned from three different regions and rms surface roughnesses were calculated. Additionally, covalently BSA conjugated THPMP coated silica surface was scanned with 10 x 10 µm areas from three different regions and rms surface roughness was calculated. During all AFM studies, 1 µm thermally grown oxide on Si wafers, cut into 0.5 x 0.5 cm pieces, were used.

AFM results (Figure 4.5 and 4.6) demonstrate a roughened surface after the coating. Also, this has been commonly observed in other silane based coatings [62]. Rms surface roughnesses from 1 x 1 µm scanned areas of the bare and THPMP coated silica surfaces were calculated as 0.59±0.03 nm and 2.08±0.09 nm, respectively.

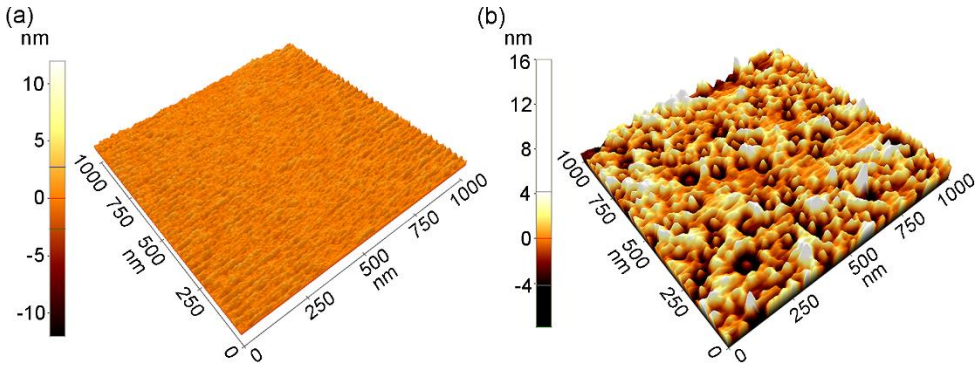

Figure 4.5: Surface topologies of bare (a) and THPMP coated (b) silica surfaces. Rms surface roughness increased after THPMP coating of silica surface.

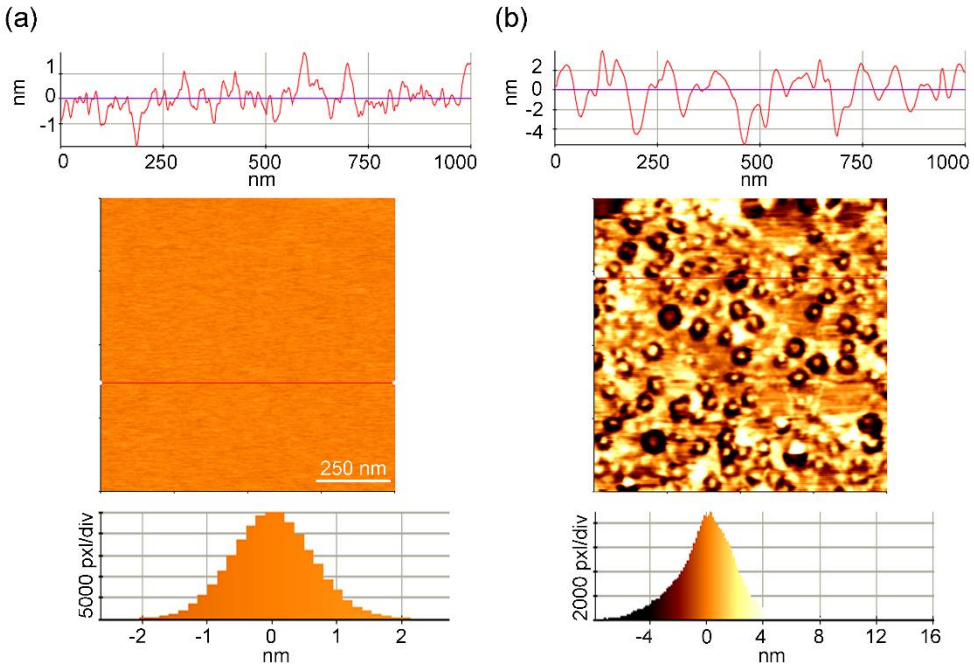

Figure 4.6: 2D AFM images (1 x 1 μm) of the (a) bare silica, (b) THPMP coated silica given with line profiles and histograms.

Additionally, from ellipsometry measurements, we assessed the thickness of the THPMP film. Ellipsometry measurements were performed with a spectroscopic ellipsometer (J.A.Woollam V-VASE). The ellipsometer was operated at single

wavelength (633 nm), while the incident angle was varied from 30° to 90° by steps of 2°, and optical constants; amplitude component (Ψ) and phase difference (Δ) were measured. Afterwards, thickness of the films were estimated by fitting data with the optical constants obtained from the literature [62, 63]. During all ellipsometry studies, 250 nm thermally grown oxide on Si wafers, cut into 1.5 x 1.5 cm, were used, and three spots from each wafer was measured.

The thickness of the THPMP film was measured as 0.65±0.02 nm. This thickness is less than the rms values we obtained; however, since the ellipsometry measurement is performed over a much larger area compared to AFM, we observe an average characteristic of the THPMP film. Rms values higher than the thickness were previously reported, which occur due to local polymerization of organosilane molecules over the surface [62]. Thus, we suggest that our results both from the AFM and ellipsometer do not contradict with each other. Our results indicate that we coated the silica surface completely with a thin THPMP film with partial aggregations.

4.3 Demonstration of the Protein Resistance of THPMP Coated Silica Surfaces

We tested the protein resistance of THPMP coating against four different proteins: Bovine Serum Albumin (BSA), lysozyme, fibrinogen and γ-globulin. BSA and γ-globulin are serum proteins with different molecular weights, while fibrinogen, another serum protein, is used in adsorption studies regarding its large molecular weight and sticky nature. Lysozyme, on the other hand, a small protein which is positively charged at our experimental conditions (at pH 7.4), is used to observe whether any electrostatic effects are present [64]. THPMP coated silica surfaces were exposed to 1 mg/ml of BSA, albumin, γ-globulin and lysozyme solutions in 1X PBS (at pH 7.4) separately for 1h at room temperature on a lab shaker.

We did XPS measurements to characterize the adsorption of these proteins. High resolution XPS scans of N1s regions of piranha treated and THPMP coated silica

surfaces were compared after being exposed separately to the aforementioned four protein solutions. The corresponding data is given in Figure 4.7.

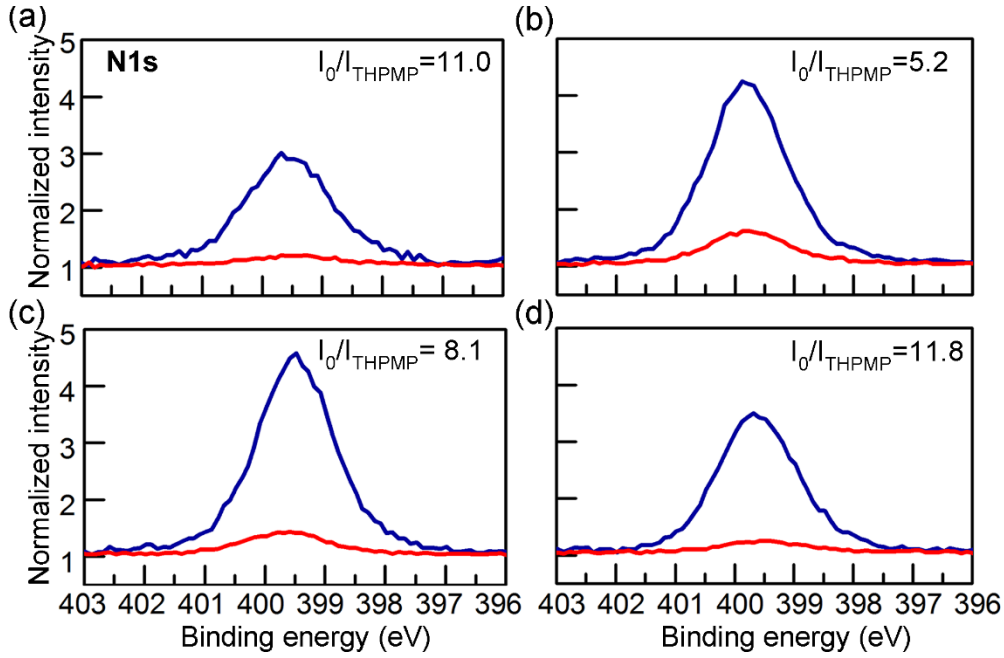

Figure 4.7: XPS spectra for N1s of bare and THPMP coated silica surfaces after exposure to (a) BSA, (B) γ-globulin, (c) fibrinogen, and (d), lysozyme solutions. THPMP coating showed significant resistance to all tested proteins. The ratios of intensities (I_0/I_{THPMP}) were calculated after background correction.

The results shown in Figure 4.7 represent that N1s signals significantly decreased from the samples having THPMP coating. While comparing the peak intensities quantitatively, instead of directly using atomic percentages of the survey [65], we performed a background correction, because we observed a significant difference in the baselines among piranha treated and THPMP coated silica surfaces, probably caused by the increased surface roughness.

We also performed ellipsometry measurements to compare BSA films formed over silica surfaces before and after the THPMP coating (Figure 4.8). The amount of the adsorbed mass could be calculated according to the formula:

$$m = d\rho$$

where d is the thickness of the protein layer measured by the ellipsometer and ρ is the density of the protein [63], which is 1320 g/L in our case [66].

The amount of BSA adsorbed is estimated to reduce fivefold according to the measured film thicknesses, which is comparable to similar ellipsometry measurements [67]. It is important to note here that it is difficult to assess the actual thickness solely depending on ellipsometry, especially when the surface contains voids [68], as in protein adsorption case. Nevertheless, the protein thicknesses we deduced from the ellipsometric fits from different spots on the wafer (Table 4.2) demonstrate that there is a significant qualitative difference between piranha treated and THPMP coated silica surfaces, coinciding with our XPS results.

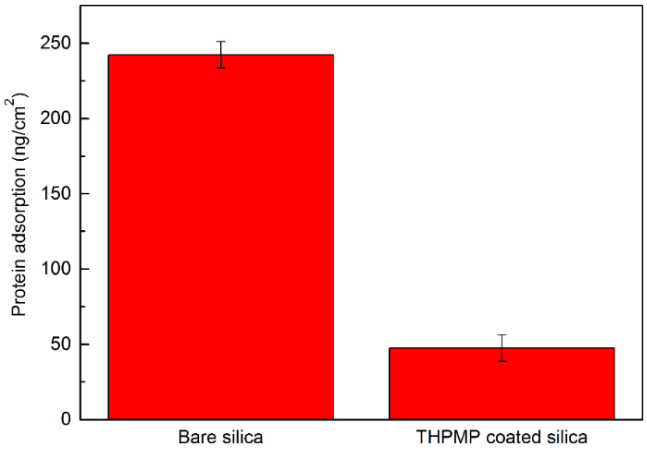

Figure 4.8: Ellipsometry measurements of nonspecific BSA adsorption over bare silica and THPMP coated silica surfaces.

	Thickness (nm)	Standard deviation	Mean-square-error	Average thickness (nm)	Protein adsorption (ng/cm^2)
B_1	1.89	0.10	1.54	1.84±0.07	242.30±8.77
B_2	1.86	0.10	1.57		
B_3	1.76	0.09	1.73		
T_1	0.40	0.09	1.57	0.36±0.07	47.50±8.94
T_2	0.39	0.09	1.66		
T_3	0.28	0.15	2.34		

Table 4.2: Ellipsometry data regarding nonspecific BSA adsorption over bare (B_{1-3}) and THPMP coated (T_{1-3}) silica surfaces. The data are given with the corresponding standard deviation and mean square error values estimated through the analysis.

Many factors are shown to contribute to protein resistance, among which the most prominent ones are hydrophilicity, inclusion of hydrogen-bond acceptors but not donors, and neutral overall charge [69]. Methylphosphonate group is hydrophilic, contains two oxygens as hydrogen-bond acceptors but no hydrogen-bond donors, and is neutral or very slightly negatively charged in PBS (pH 7.4) when coated on silica nanoparticles, as measured previously by our research group [53]. Therefore, the THPMP coating over silica could be predicted to show a considerable protein resistance, since its characteristics fit within the empirically described domain of high protein resistance.

4.4 Covalent Protein Conjugation to the THPMP Functionalized Silica Surfaces

In order to covalently conjugate proteins to the methylphosphonate groups, we used N-(3-Dimethylaminopropyl)-N′-ethylcarbodiimide hydrochloride (EDC, MW 191.70, Merck) as an activator. THPMP coated silica surfaces were soaked into a 5 mM EDC solution in MES buffer (50 mM MES, 0.1 mM NaCl in ultrapure water at pH 6.0 adjusted by NaOH) and incubated for 2h on a lab shaker for surface activation. To

remove residual EDC molecules, the surfaces were washed once with the MES buffer rapidly and then soaked into a 1 mg/ml protein containing 1X PBS (at pH 7.4) for 1 h on a lab shaker. To remove unbound proteins, the surfaces were washed with 1X PBS (at pH 7.4). All steps were performed at room temperature.

EDC attacks to the negatively charged terminal oxygen of methylphosphonate, forming an unstable O-acylisourea intermediate, which is then replaced by a primary amine. As a verification, we used N-Hydroxysuccinimide (NHS, MW 115.09, Merck) to apply EDC/NHS chemistry and performed high resolution N1s scan to observe NHS esters (Figure 4.9). THPMP coated silica surface was activated with a solution containing 5 mM EDC and 2 mM NHS in the MES buffer for 2 h on a lab shaker. Then, the surface was washed with MES buffer to remove any residual products. We observe two distinct peaks at 400.0 and 402.2 eV, corresponding to the N–C and N–O, respectively, indicating formation of NHS ester termination [70]. In one previous study regarding EDC activation of methylphosphonate for covalent attachment of primary amines, phosphoramidate chemistry was suggested; i.e., the unstable O-acylisourea was suggested to be formed via the methyl group of the methylphosphonate [49]. However, according to our XPS data, we observe the typical N–C and N–O bondings verifying the formation of NHS esters. Our results imply that the NHS ester formation occurs via negatively charged oxygen terminal of THPMP molecules, suggesting a phosphonamidate structure [71].

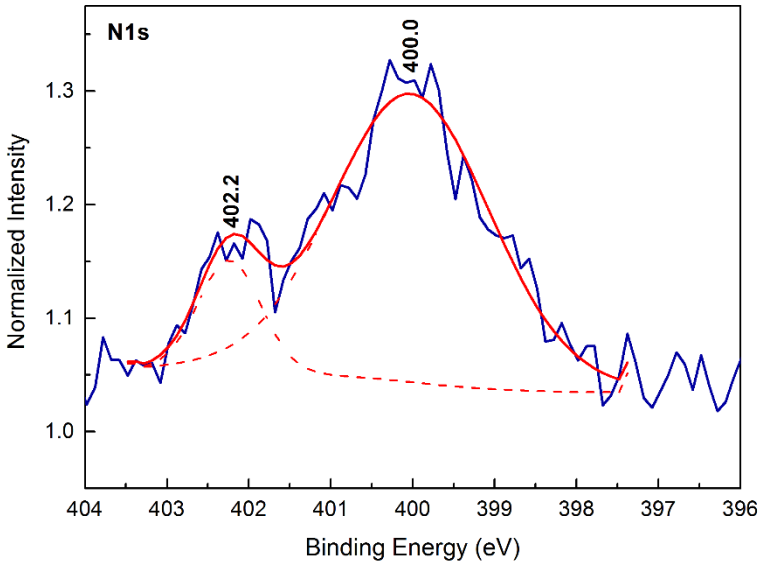

Figure 4.9: High resolution XPS scan of N1s region for the EDC/NHS chemistry applied THPMP coated silica surface. Original data were given in blue lines, while fits for single peaks and envelopes were given in dashed and solid red lines, respectively. Components peaks (at 402.2 and 400.0 eV) verifies the existence of stable NHS-esters on surface. Full-width half-maxima of the component peaks at 402.2 and 400.0 eV, are 0.9 eV and 2.3 eV, respectively.

We utilized confocal microscopy to examine protein resistance and bioconjugation simultaneously and compare different samples quantitatively, using albumin–fluorescein isothiocyanate conjugate (FITC-BSA, MW of BSA 66 kDa and MW of FITC 389.4, Sigma-Aldrich) (Figure 4.10). Confocal measurements were performed with a confocal microscope (Model LSM 510, Zeiss, Germany). FITC-BSA nonspecifically adsorbed on the substrates were excited with Argon laser at 488 nm, and emission were collected over 505 nm using photomultiplier tubes. The settings for gain and offset were kept constant throughout all measurements. The pinhole was set to 5 airy units in order to collect more signal, and the images were formed by averaging each scan line 16 times. ImageJ program was used for image processing. Fluorescent intensity from one only piranha treated sample was utilized as background signal, and the measured fluorescence intensity value was subtracted from each data. For quantitative comparison, three measurements from different places of each wafer were

considered. Quartz wafers were used to avoid interference effects that could be observed with thin thermal silica on Si. The quartz samples were incubated for 1 h in 1 mg/ml solutions of FITC-BSA (in 1X PBS at pH 7.4) on a lab shaker at room temperature. Environmental light was avoided during sample preparation. During all confocal microscopy studies, quartz wafers, cut into 0.5 x 1.5 cm, were used. First, we verified that the THPMP coated surface is protein resistant, as could be seen from the confocal images of the piranha treated (Figure 4.10a) and THPMP coated (Figure 4.10b) quartz wafers, comparing their fluorescence intensities. Then, we covalently attached FITC-BSA over the THPMP coated quartz wafers after EDC activation (Figure 4.10c) by incubating in a 1 mg/ml solution of FITC-BSA for 1 h, and observed a significant fluorescence, which intensity is comparable to the nonspecific adsorption. Normally, it is difficult to distinguish covalent coupling from nonspecific adsorption [72]. However, we assert that covalent conjugation occurred, since proteins were successfully accommodated over the THPMP film after EDC activation, which was otherwise protein resistant. We also tested the recovery of THPMP after EDC activation by washing the wafer thoroughly with ultrapure water prior to incubation with FITC-BSA. We observed a significant loss in the fluorescence (Figure 4.10d), indicating reversibility of the EDC activation. The quantitative comparison of all fluorescence intensities was also given (Figure 4.10e). These results show that THPMP possesses a dramatic protein resistant behavior. Additionally, covalent attachment of proteins is feasible by activating the THPMP coated surface with EDC, which is totally reversible in terms of protein resistance.

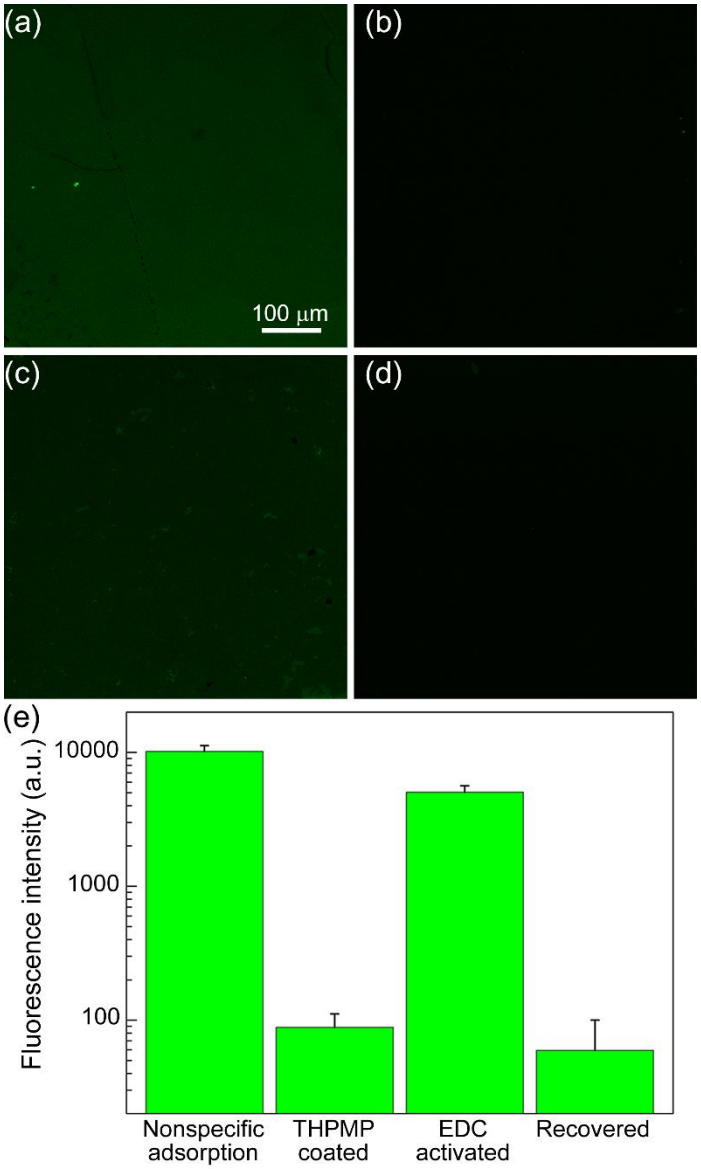

Figure 4.10: Confocal microscopy for quantitative detection of protein resistance. Nonspecific adsorption of FITC-BSA over piranha treated quartz surface (a) is almost diminished after THPMP coating (b). Covalent attachment, which produces comparable signal level to nonspecific adsorption, is possible by EDC activation (c), while THPMP coating can be reverted to its protein resistant original state later (d). The comparison of the fluorescence intensities (e) enables quantitative comparison of the amount of protein present over the surface.

High resolution XPS scans of P2p and N1s regions of recovered THPMP coatings on thermal silica (Figure 4.11) also verified that the film chemically returns to its unmodified form. The fact that O-acylisourea is quite unstable in aqueous environment

could be advantageous, regarding recovery of protein resistance property of the THPMP film after EDC activation and covalent modification.

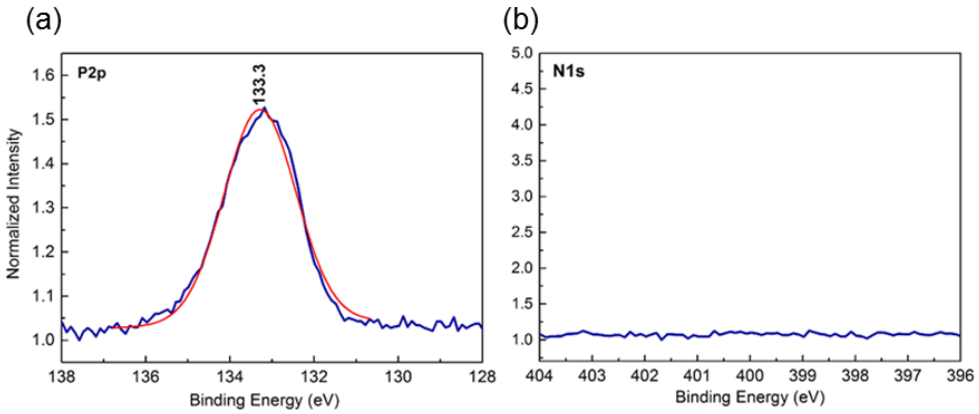

Figure 4.11: High resolution XPS scans of P2p and N1s regions for the (a) EDC activated and (b) then recovered THPMP coated silica surface. Original data were given in blue lines, while fit for single peak was given in solid red line. P2p peak (solid red line) has full-width half-maximum of 2.0 eV.

As a separate control, we covalently conjugated amine modified deoxyribonucleic acid (DNA) single strands labeled with the fluorophore Cy5 (Excitation: 633 nm, Emission: 670 nm) to the THPMP coating by applying the same procedure we used to conjugate the proteins, and compared fluorescence intensities of both Cy5 and FITC after incubating one sample in 1 mg/ml FITC-BSA solution for 1 h (Figure 4.12). Results verified that our surface is bioconjugable, and its protein resistant characteristics endure after the bioconjugation.

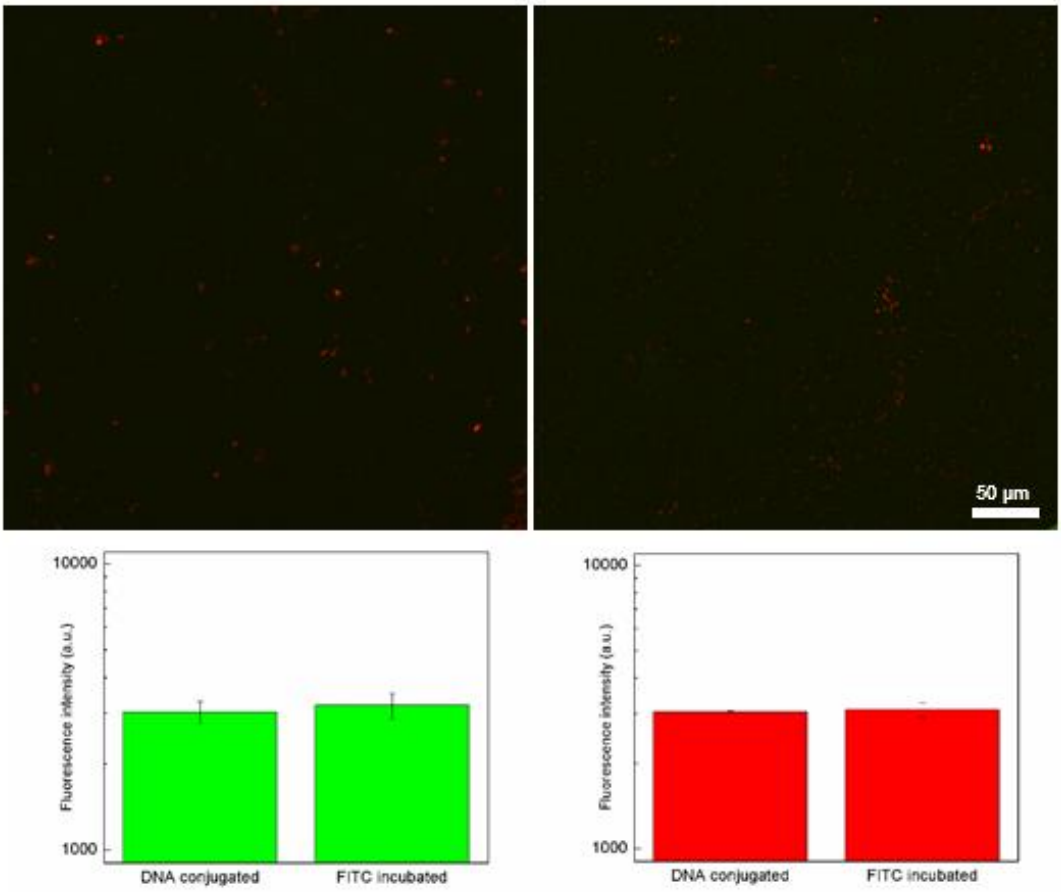

Figure 4.12: Confocal microscopy images of quartz wafers functionalized with Cy5 labeled single strand DNA (a) and subsequently incubated in 1 mg/ml FITC-BSA (b). The fluorescence intensities of FITC (c) and Cy5 (d) does not show a significant difference between these two samples, demonstrating the bioconjugability and simultaneous protein resistance.

Confocal microscopy measures emitted photons from fluorophores attached to the proteins, which is proportional to the amount of proteins on surface, suggesting that THPMP induces around two orders of magnitude reduction in the amount of adsorbed BSA. According to the XPS measurements, the resistance towards other proteins is expected to be on the same order as well. Although not coinciding with the obtained XPS and ellipsometry results, when the limitations of these research tools are considered, such as difficulty of measurement on rough surfaces with XPS [73], or thin film approximation of ellipsometer [63], we could assume that the confocal microscopy measurements are much reliable for a quantitative analysis.

AFM images were taken after covalent coupling of BSA over the THPMP coated silica surface with two different scanned areas (Figure 4.13 and 4.14). Rms surface roughnesses of scanned with wide and narrow areas from the covalently BSA conjugated surface were measured as 3.82±0.16 nm and 3.62±0.56 nm, respectively. The surface roughness increased after covalent coupling of BSA to the THPMP film. Moreover, the surface shows a uniform distribution of the BSA over a wide area range. It can be seen from the figure that the proteins formed a layer following pattern of the THPMP coating.

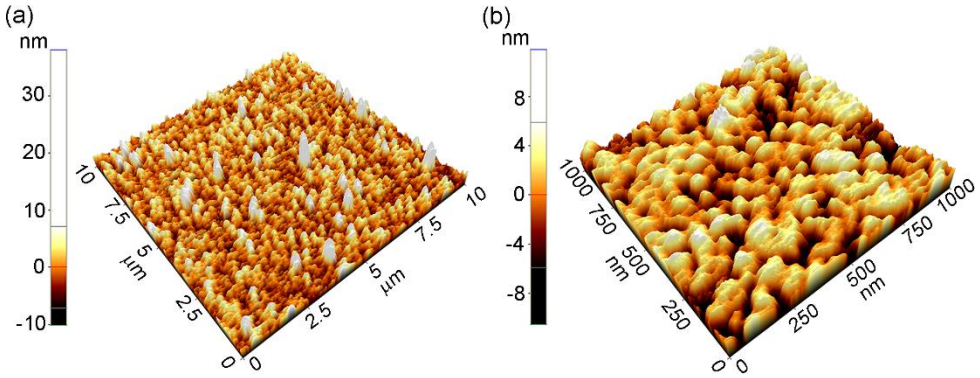

Figure 4.13: Surface topologies of covalently BSA conjugated silica surfaces with (a) 10 x 10 and (b) 1 x 1 µm scanned areas. 3D image on the left shows that the bioconjugated coating has a definite topography over a wide area. 3D AFM image on the right demonstrates that the bioconjugation follows the pattern of the THPMP coating, with a slightly but yet significantly increased rms surface roughness.

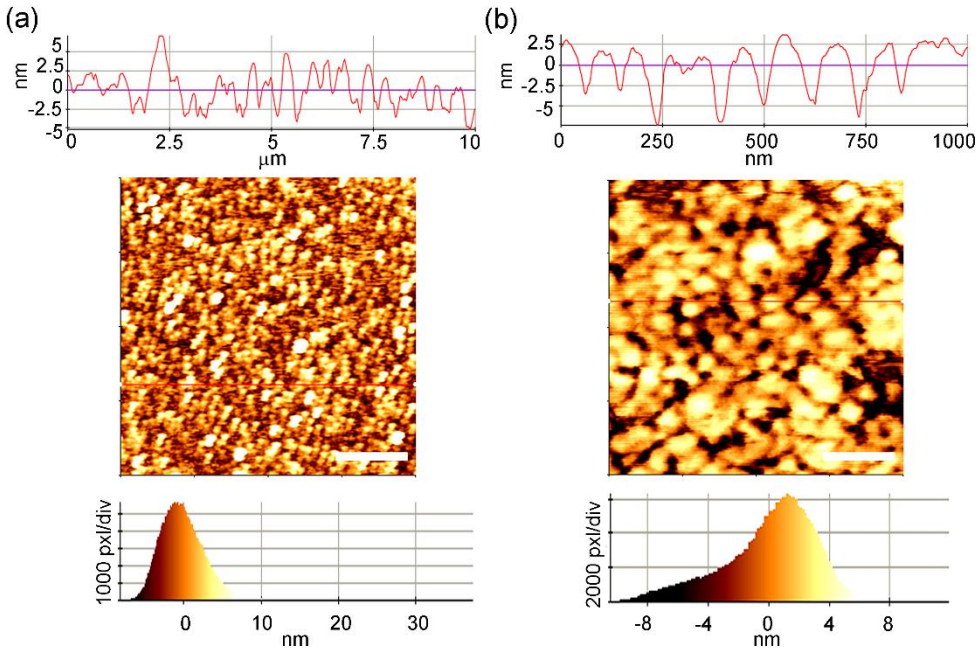

Figure 4.14: 2D AFM images of the covalently BSA conjugated THPMP coated silica surface with (a) 10 x 10 µm, and (b) 1 x 1 µm scanned areas given with line profiles and histograms. Scale bars are 2.5 µm and 250 nm, respectively.

We also took an AFM image of non-specifically bound BSA onto a piranha cleaned silica surface with 1 x 1 µm scanned area (Figure 4.15). Rms surface roughness was measured as 1.23±0.19 nm and a significantly different morphology than of the BSA conjugated THPMP film was observed.

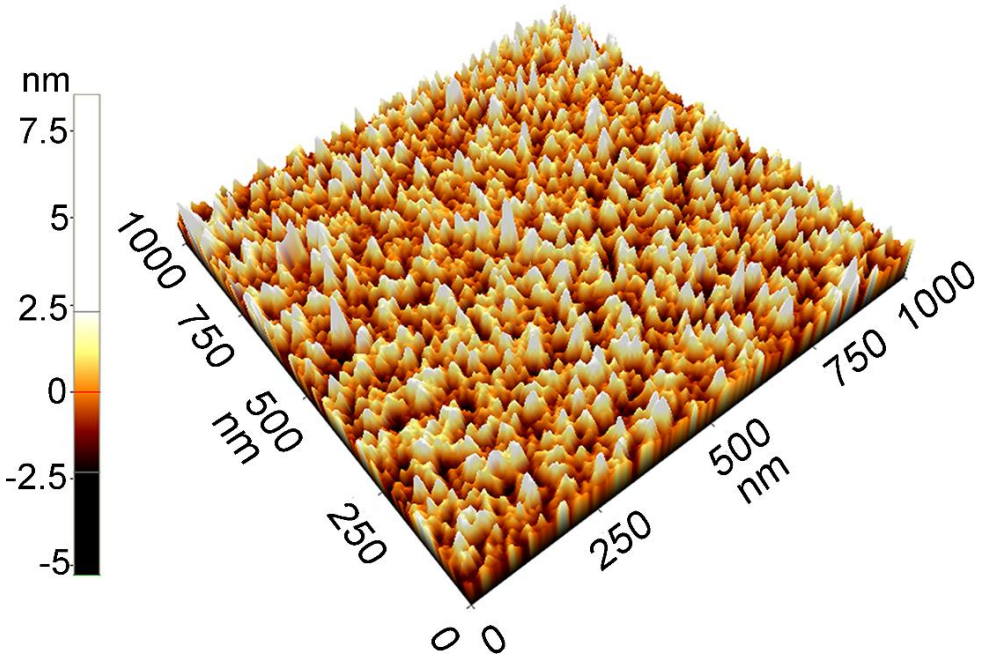

Figure 4.15: Surface topology of the non-specifically bound BSAs onto piranha cleaned silica surface. Rms surface roughness was measured as 1.23 ± 0.19 nm.

In conclusion, we demonstrated that methylphosphonate containing organosilanes could effectively be used as protein resistant coatings which is simultaneously bioconjugable [74]. Both coating of silica with methylphosphonate and covalent protein conjugation are quite straightforward and efficient, and activation of methylphosphonates could easily be reverted, forming an inert coating around the bioconjugated moiety. Using only a single molecule in a multifunctional manner provides an unprecedented flexibility to the model we propose, which in our opinion could find important applications especially in biomedical field, such as smart biocompatible implants, targeted drug delivery, and high selectivity and sensitivity biosensors. The first application would be for functionalization of microtoroids for high selectivity and sensitivity biodetection.

Chapter 5

Microtoroids as Biosensors with High Selectivity and Sensitivity

5.1 Construction of the Biosensing Setup

Since almost all biomolecular interactions occur inside an aquatic environment, and most of the analytes, which might be desired to be detected, exist as an aqueous solution, it is critical to perform biosensing experiments inside water. Therefore, two syringe pumps were integrated to the optical measurement system. Plexiglas substrates were drilled by a drilling machine (Dremel) and syringe needles were inserted inside the drill holes. Then, needles were fixed by using silicone rubber. After the appropriate tubing, the syringe pumps could be used for infusion or withdrawal of fluids precisely. A glass microscope slide standing on columns in order to keep the liquid droplet stable, in the form of a microaquarium. For maintaining the volume of the droplet constant, one pump performs infusion while the other pump withdraws the liquid. The image of the biosensing setup is given in Figure 5.1. The experiment procedure is schematically shown in Figure 5.2. Prior to the experiment, the infusion tube was filled with analyte

solution, while 200 µl of buffer solution free of analyte was placed below the microscope slide, over the microtoroid by a micropipette.

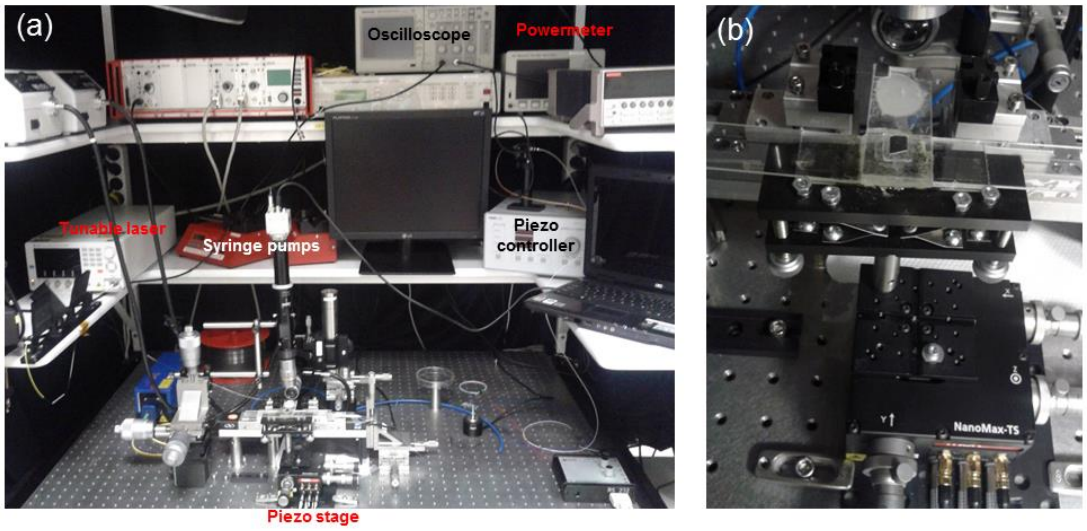

Figure 5.1: Image of the biosensing setup. (a) The components of the biosensing setup, which are piezo stage and controller, tunable laser, powermeter or detector, oscilloscope, and syringe pumps with appropriate tubing. (b) A close view of the biosensing platform.

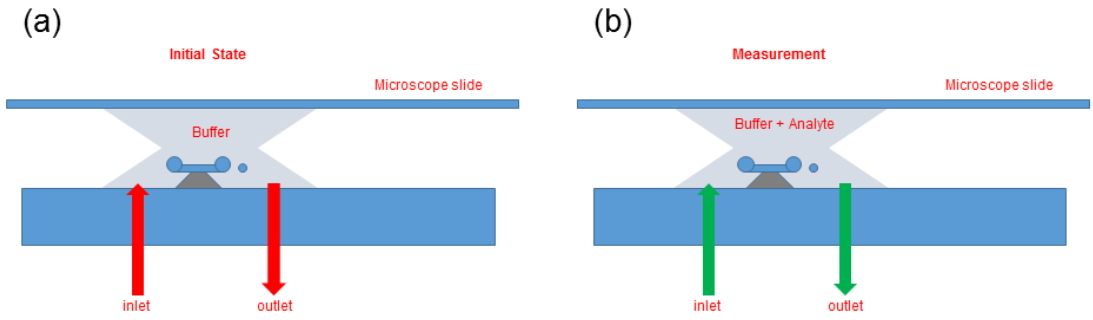

Figure 5.2: Schematic representation of the biosensing in the microaquarium. The chip is fixed on the Plexiglas by tape. There are two holes drilled on the Plexiglas platform, for simultaneous infusion and withdrawal of liquids via the syringe pumps. (a) The microtoroids are optically coupled inside the microaquarium prior to experiment. (b) The analyte is infused and the liquid constituting the microaquarium is withdrawn simultaneously with the same rate in order to keep liquid volume constant.

For biosensing, WGM resonances of the microtoroids were monitored with high speed and accuracy by tracking a single resonant mode continuously and recording each measurement. This way, the shifts in the resonant wavelength with respect to time could be determined. After the data was collected, a script implemented in MATLAB was used to make a Lorentzian fit for each data frame by nonlinear regression. The resonant wavelength of each data frame was determined by the Lorentzian fit, and was considered as a function of time (See Appendix).

5.2 Analysis of the Data

Biosensing with microtoroids depends on the interaction of the analytes with the microresonator on its surface, which could occur as specific or nonspecific adsorption. These interactions cause shifts in the resonant wavelength, depending on the change in the optical path length [75]. In our experimental setup, interaction occurs within a microaquarium formed by a glass microscope slide placed over a liquid droplet. The analyte was infused inside the microaquarium with a syringe pump. The microaquarium volume was kept constant by simultaneously withdrawing liquid at the same flow rate. Assuming that no concentration gradient exist within the microaquarium, since the volume is small, the differential equation that governs the analyte concentration inside the microaquarium with respect to time is:

$$\frac{dC}{dt} = C_o \frac{J_i}{V} - C \frac{J_o}{V}$$

where C is the microaquarium concentration at a given t, C_o is the concentration of the analyte solution pumped inside, J_i and J_o are inward and outward flux rates, and V is the volume of the microaquarium. The solution of this differential equation under proper boundary conditions could be written as:

$$C(t) = C_i\left(e^{-Jt/V}\right) + C_o(1 - e^{-Jt/V})$$

where the flux rates inward and outward are denoted by J, since their rates are equal, and C_i is the initial analyte concentration within the microaquarium. In our experimental conditions C_i is equal to zero, thus the equation is simplified to:

$$C(t) = C_o(1 - e^{-Jt/V})$$

It is obvious that at $t = 0$; the analyte concentration inside the microaquarium is 0, and when t approaches infinity, the microaquarium analyte concentration approaches to the concentration of the analyte infused.

5.3 Surface Modification of Microtoroids

One of the most serious problem regarding biosensing is suppressing nonspecific interactions. This is a critical issue because it impedes utilization of especially biosensors with high sensitivity in complex media, due to the fact that the analyte concentration is orders of magnitude lower than other materials, especially proteins under these circumstances. As sensors with ultimate sensitivity, optical microresonators encounter with this drawback limiting their uses except within extremely controlled buffer solutions frequently. Although elaborate strategies exist for functionalization of microresonators with various agents such as antibodies or single DNA strands in order to attain specificity, eliminating nonspecific interactions still persists as a problem. Most frequently used method for reducing the effect of nonspecific interactions is calibrating the measurement with respect to complex media without the analyte, and then performing the detection [14, 76]. There have been some recent work regarding modification of WGM microresonator surfaces with silane based molecules that resist protein resistance [24]; however, the results of this study failed to show a significant level of reduction in nonspecific adsorption, even in much lower protein concentrations than a real complex media such as serum, and also a simultaneous bioconjugation strategy was not suggested.

The results of our recent research related to production of simultaneously protein resistant and bioconjugable silica surfaces [74] was applied to microtoroids in order to attain label-free biosensing with high selectivity and sensitivity. This strategy solves two important problems at the same time: reducing, if not eliminating, the nonspecific adsorption, and covalent conjugation of targeting probes; i.e., antibodies in our case.

All silane based molecules require an activation step in order to increase the number of and expose the hydroxyl groups on the silica surface, from which covalent conjugation of the silanes occur. Piranha treatment and oxygen plasma are the most widely used methods for silica surface activation, while there are other treatments including ozone-UV, sodium hydroxide, ammonia:hydrogen peroxide mixture, nitric acid, hydrochloric acid, sulfuric acid, chromic acid, or mineral acids with hydrogen peroxide [39]. More than one of these applications could also be combined or sequentially used. In a previous study, some of these methods were compared regarding functionalization of microtoroids, and especially piranha treatment was reported to damage the microtoroids by inducing micron sized cracks, reducing quality factors of the resonators [33]. However, in our experimental conditions, we did not observe such a significant effect of piranha treatment on the Q of the microtoroids (Figure 5.3). Therefore, piranha treatment was used for activation of the microtoroid surfaces prior to coating.

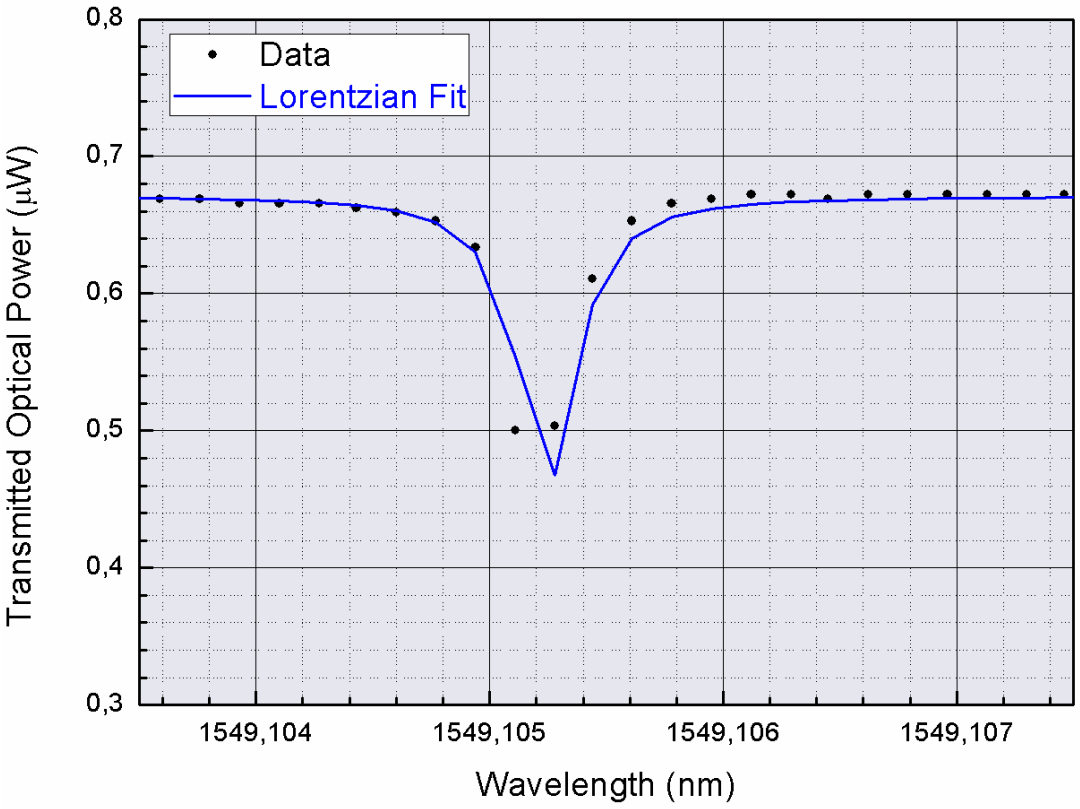

Figure 5.3: A resonance dip recorded from optical coupling to a piranha treated microtoroid. After 15 min of treatment, no decrease in the Q was observed.

The microtoroids were coated with a similar recipe that was used in our previous research. A slight modification was done in the THPMP solution; i.e., a 5 % methanol solution in ddH_2O (pH 4.6, adjusted with acetic acid) was used at RT. The modification was performed because this recipe provided better results regarding protein resistance. Piranha cleaned and THPMP coated microtoroids were compared regarding nonspecific protein adsorption over them by using confocal microscopy. During these experiments, DIC and fluorescence images of the microtoroids were sequentially captured and then merged for better understanding the spatial properties of the fluorescence. As could be seen from Figure 5.4, there is a considerable nonspecific protein adsorption over piranha cleaned microtoroid, while the THPMP coated microtoroid exhibits a significant protein resistant characteristic.

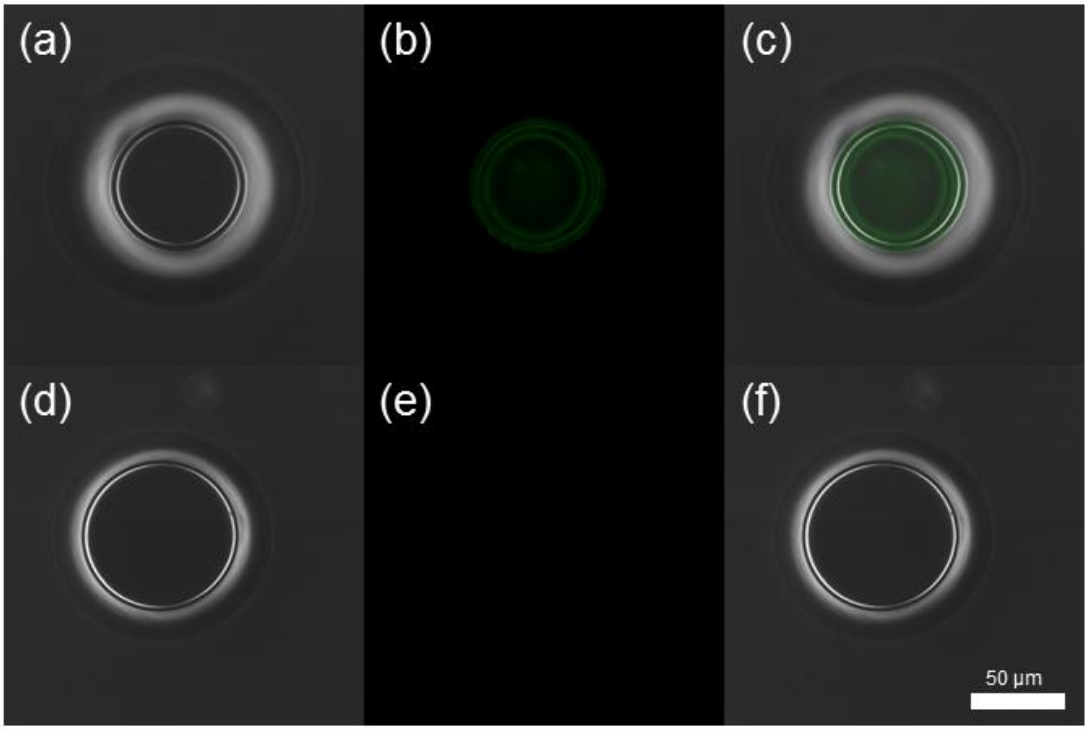

Figure 5.4: DIC and confocal images of only piranha cleaned (a,b) and THPMP coated (d,e) microtoroids. There is a significant fluorescence from the piranha cleaned microtoroid, while this signal is almost vanished from THPMP coated one, showing a significant reduction in nonspecific protein adsorption. The merged images of these microtoroids are also given (c,f).

Covalent protein conjugation is performed with the same recipe we used to conjugate proteins on silica surfaces [74]. Human anti iterleukin-2 (IL-2) antibodies (Sigma-Aldrich) are covalently attached to THPMP after EDC activation in MES buffer. The activation is performed for 2 h at RT, while the conjugation takes place at 4 °C for again 2 h in PBS. The concentration of the antibody used is 2.5 µg/ml, freshly prepared from 1 mg/ml aliquots of 2.5 µl. After the conjugation, the chip is washed with and kept inside PBS at 4 °C until the experiment.

5.4 Label-free Biosensing with Microtoroids with High Sensitivity and Selectivity

Human IL-2 protein (Sigma-Aldrich) in 100 mM acetic acid is diluted to a final concentration of 250 ng/ml in PBS or PBS containing 0.1X fetal bovine serum (FBS). They are freshly prepared from 1 mg/ml aliquots of 2.5 µl. Also, 0.1X FBS in PBS is prepared for control experiments. All reagents are used within the first 6 h of preparation, and later discarded properly.

The reagents are filled inside syringes, and the tubes connecting the syringes to the measurement setup is completely filled with the liquid. Then, the chip is placed on the platform and fixed by using tape from both sides. 200 µl of PBS is dropped over the chip by a micropipette and a glass slide is placed over the droplet, standing on three columns on the platform, approximately 1 mm higher than the chip. Because of the hydrophobicity of Plexiglas and hydrophilicity of the glass slide, the droplet between the surfaces forms a stable microaquarium.

After the optical coupling is attained, the experiment is started. It is important to note here that due to higher absorption of H_2O compared to air at the wavelength we use; i.e., 1550 nm, the mode spectrum enlarges inside liquid media, and Q reduces *ca.* two orders of magnitude. This effect could be seen from the Figure 5.5. One other significant effect in measurements in liquid is that overall reduction in the transmission, depending on a reduced refractive index difference between the fiber and its environment.

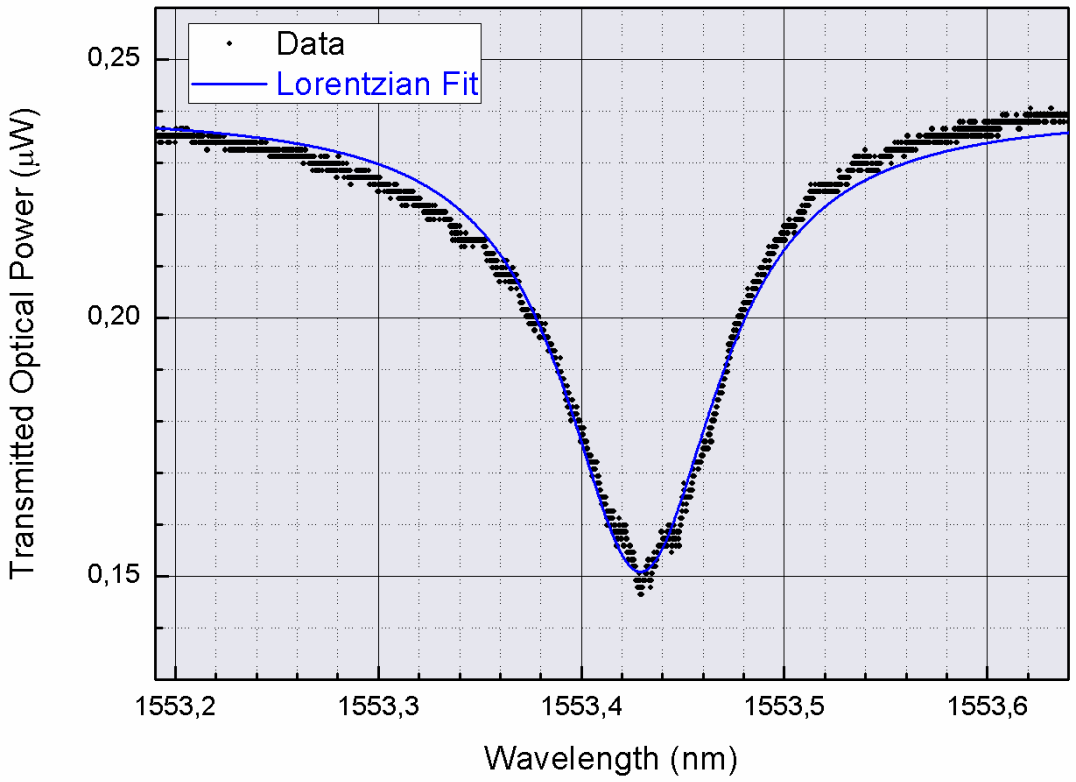

Figure 5.5: Measurement of whispering gallery modes inside liquid media. There is a quite significant enlargement in the $FWHM$ of the mode, representing a decrease in Q. This effect occurs because H_2O molecules around the microresonator absorb the light around 1550 nm to some extent.

Under coupled regime is used throughout all the experiments. This was preferred because due to the perturbation caused by liquid infusion and withdrawal, the critically coupled fiber might enter into over coupling regime, causing a further enlargement of the WGM, and also a shift in the resonant wavelength. Under coupled mode is tracked for 2-5 min before initiating the infusion and withdrawal. This enables observation of noise in the data. As could be observed from Figure 5.5 we have a significant noise in the data.

The main cause of the noise is related to hysteresis in our tunable laser system. Yet, this noise could be minimized by some techniques. One strategy is instead of performing one way scan and returning to the start wavelength quickly, performing a two way scan, enabling slow reorientation of the gratings inside our laser. Also, a

sweep delay of 100 ms between two consecutive scans is applied. Additionally, it is always possible to apply some appropriate statistical methods effectively such as filtering, or smoothing the data. On the other hand, there is another part of the noise, which is caused by the low Q of the microtoroids in aqueous environment. This is caused by fitting a data with a large linewidth (on the order of tens of picometers) to a Lorentz function, where the error becomes more significant. This problem could be solved by using a tunable laser at visible wavelengths, especially around 670 nm [7], where the absorption of H_2O is at its minimum.

The noise level is critical in biosensing, because the limit of detection (LOD) and limit of quantification (LOQ) of the sensor are proportional to the standard deviation (std) of the data. The LOD is 3 X std, while the LOQ is 10 X std.

After each data is collected and analyzed, the time trace is converted to the concentration. In order to correlate the resonance shift with respect to time to analyte concentration, the formula reached at Section 5.2 is used, which is:

$$C(t) = C_o(1 - e^{-Jt/V})$$

First, the modified microtoroid was compared to a bare microtoroid regarding nonspecific protein adsorption. For this, 0.1 X FBS in PBS was introduced to the microaquarium with a flow rate of 5 µl/min. As could be seen from Figure 5.6, the modified microtoroid showed a significant protein resistance compared to the bare microtoroid. The degree of anti-fouling was lower than we expected, considering the confocal microscopy results, yet the resonance shift pattern of the modified microtoroid is temporally different than the bare one, and the amount of protein resistance is comparable to the values in the literature [24]. Although THPMP was shown to be resistant against nonspecific adsorption of different proteins in our previous work [74], serum is a quite complex media [77], including many different types of proteins, among which some could be relatively unaffected from THPMP coating (Table 5.1). Also, a difference in the refractive indices of PBS and FBS probably caused the shift in the resonance wavelength, independent of the protein adsorption. Another reason might be that although we diluted FBS to 0.1 X, the total protein concentration is still higher than we used in confocal microscopy experiments.

It could be seen from Figure 5.6b that especially at lower FBS concentrations, modified microtoroid shows a stable protein resistant characteristic, until up to a certain FBS concentration value.

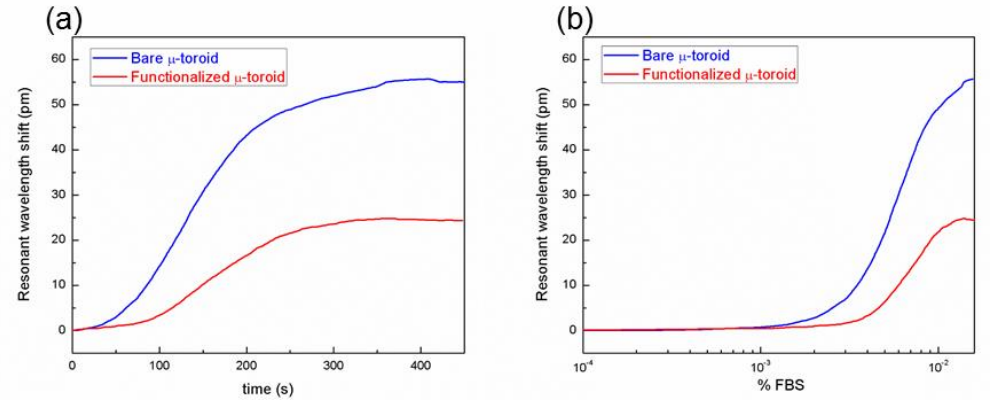

Figure 5.6: Protein resistant characteristic of a surface modified microtoroid. (a) Time trace of the resonant wavelength shift after introduction of 0.1X FBS with an infusion rate of 5 μm/s. The graph starts at the point of the increase of the resonant wavelength. (b) The corresponding FBS concentration dependence of the resonant wavelength shift.

Component	Average	Range
Endotoxins (ng/ml)	0.35	0.01 - 10.0
Glucose (mg/ml)	1.25	0.85 - 1.81
Protein (mg/ml)	38	32 - 70
Albumin (mg/ml)	23	20 - 36
Hemoglobine (µg/ml)	113	24 - 181
Bilirubin, total (µg/ml)	4	3 - 11
Bilirubin, direct (µg/ml)	2	0 - 5
Urea (µg/ml)	160	140 - 200
Urate (µg/ml)	29	13 - 41
Creatinin (µg/ml)	31	16 - 43
Insulin (µU/ml)	10	6 - 14
Cortisol (ng/ml)	0.5	0.1 - 23
Growth hormone (ng/ml)	39	18.7 - 51.6
Parathormone, PTH (ng/ml)	1.72	0.085 - 6.18
Triiodothyronine, T3 (ng/ml)	1.2	0.56 - 2.23
Thyroxine, T4 (ng/ml)	0.12	0.08 - 0.16
Thyroid-stimulating hormone, TSH (ng/ml)	1.22	0.2 - 4.5
Follicle-stimulating hormone, FSH (pg/ml)	95	20 - 338
Testosterone (pg/ml)	400	210 - 990
Progesterone, P4 (pg/ml)	80	3 - 360
Prolactin = Luteotropic hormone, LTH (pg/ml)	176	20 - 500
Luteinizing hormone, LH (pg/ml)	8	1,2 - 18
Prostaglandin E (ng/ml)	5.9	0.5 - 30.5
Prostaglandin F (ng/ml)	12.3	3.8 - 42.0
Vitamin A (ng/ml)	90	10 - 350
Vitamin E (ng/ml)	1.1	1 - 4.2
Cholesterol (µg/ml)	310	120 - 630
Lactate-dehydrogenase, LDH (mU/ml)	864	260 - 1,215
Alkaline Phosphatase (mU/ml)	255	110 - 352
Aspartate-Aminotransferase, ASAT (mU/ml)	130	20 - 200
Sodium, Na+ (µeq/ml)	137	125 - 143
Potassium, K+ (µeq/ml)	11.2	10.0 - 14.0
Calcium, Ca2+ (µeq/ml)	6.75	6.30 - 7.15
Chloride, Cl-(µeq/ml)	103	98 - 108
Phosphate, Pi (µg/ml)	98	43 - 114
Selen (µg/ml)	0.026	0.014 - 0.038
pH	7.4	7.20 - 7.60

Table 5.1: Composition of FBS. In 0.1X FBS in PBS, the total protein concentration is in average 3.8 mg/ml, of which 2.3 mg/ml are albumins [77].

The second time trace and the corresponding concentration calibration given in Figure 5.7 represent the IL-2 measurement performed in PBS. It could be seen from the Figure that although the IL2 concentration in the analyte solution is very low, it

could still induce a significant shifts in the resonant wavelength. Taken together with the std of this data, which is 0.025 pm after smoothing, the LOD in PBS is estimated to be 0.1 nM, and LOQ was found to be 0.4 nM. These values are 1-2 orders of magnitude lower; therefore better than ELISA sensitivity, which is the gold standard in label-free protein detection.

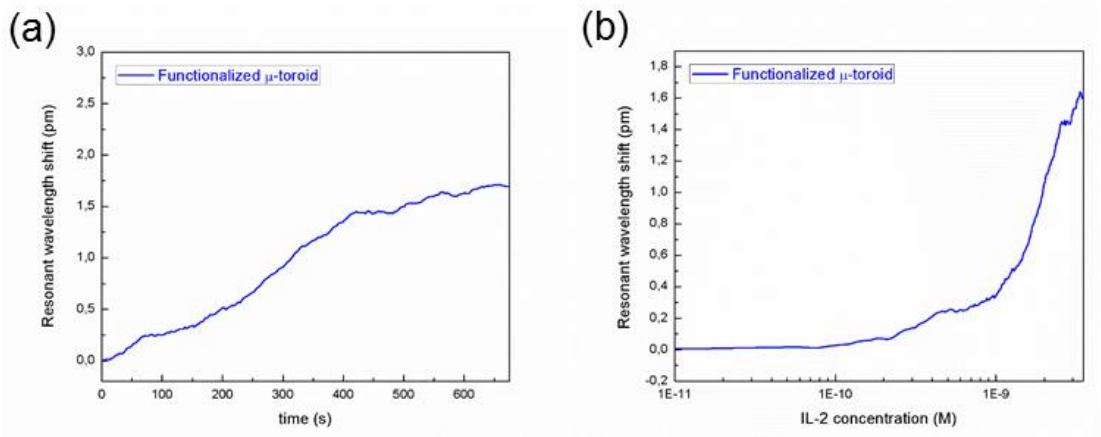

Figure 5.7: IL-2 measurement in PBS buffer. (a) Time trace of the resonant wavelength shift after introduction of IL-2 with an infusion rate of 5 μm/s in PBS. The graph starts at the point of the increase of the resonant wavelength. (b) The corresponding IL-2 concentration dependence of the resonant wavelength shift.

The time traces in the Figure 5.8 represents the comparison of the responses of the bare and functionalized microtoroids towards IL-2 in PBS containing 0.1X FBS. Prior to the infusion, in order to have the FBS concentration constant, 200 μl of 0.1X FBS in PBS was added over the microtoroid. As could be seen in the figure, IL-2 created a shift in the resonant wavelength of the functionalized microtoroid. The resonant wavelength of the bare microtoroid tends to decrease with time, probably due to absorption of some components of FBS on the syringe and tube walls. This effect is expected to occur in the experiment with functionalized microtoroid; therefore, under these circumstances, it would be difficult to estimate the concentration dependence of the shift. Yet, compared with the response in Figure 5.7, we could deduce that the sensitivity of the biosensing is not significantly affected in complex media. The concentration of the analyte compared to the total protein concentration in complex

media is more than four orders of magnitude lower, and this results shows that our microtoroid based biosensor is quite selective besides its sensitivity.

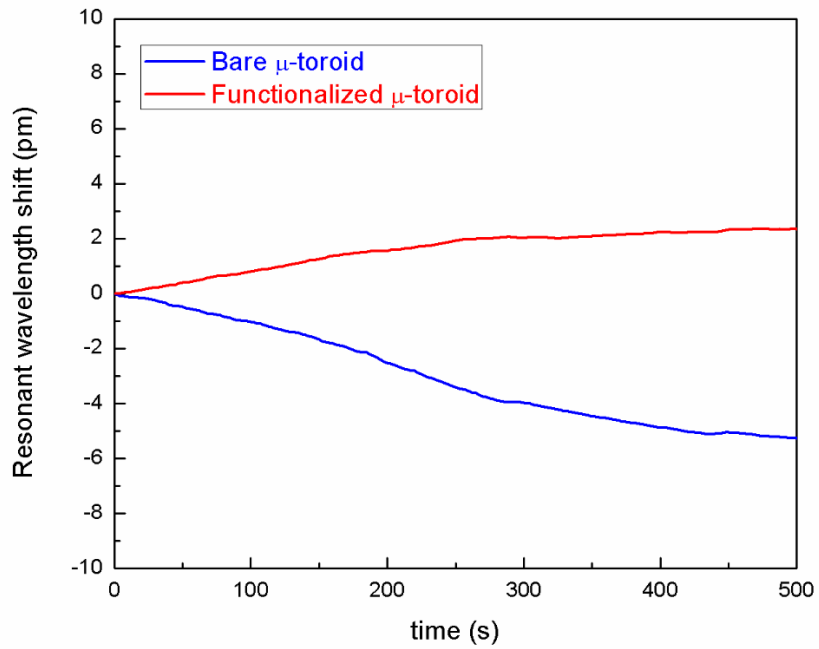

Figure 5.8: IL-2 measurement in PBS buffer with 0.1X FBS. The time trace of the functionalized microtoroid shows a significant shift after the infusion of the analyte in complex media. This shift is on the same order with the shift observed in PBS. A significant shift was not observed in the bare microtoroid, which could be anticipated, since the concentration of IL-2 in the analyte solution is more than four orders of magnitude lower that the total protein concentration. The decrease in the resonant wavelength with time could have occurred due to absorption of some constituents of FBS on the syringe and tube walls.

As a conclusion, a novel strategy was demonstrated in order to produce biosensors with high selectivity besides sensitivity. Phosphonate based modification of biosensors in order to obtain bioconjugable protein resistant surfaces could be used reliably in order to perform biodetection in complex media, therefore expand the use of WGM based biosensors beyond the laboratories, in real life issues such as detection of cancer markers or pathogens, food safety and public health, and civil defense against bioterrorism or biological weapons [78].

Chapter 6

Large Scale Integration of Nanowires as a Macroscopic Functional Device

6.1 Large Scale Nanowire Integration Strategies

Integration of nanoscale building blocks to macroscopic structures is currently at the forefront of nanotechnology applications. Among various distinct types of nanostructures, nanowires constitute a unique category regarding their outstanding characteristics such as virtually unlimited material composition, excellent tunability of size, dimensions, hierarchy and geometry, and a myriad of elaborate methods for their production [79]. There have been major leaps towards large scale integration of nanostructures like carbon nanotubes [80, 81] and graphene [82, 83] recently, yet the fields still await ultimate solutions. However, large scale utilization of their nanowire counterparts could not be satisfactorily accomplished to date, despite their unusual and promising physical properties and considerable efforts put into their design and fabrication. Assembly of nanowires into functional devices possesses substantial challenges. Besides their extremely small dimensions hindering their manipulation, as well as other nanostructures, inevitable complications exist since usually nanowires

have been produced in a random or irrelevant orientation regarding their final device location, irrespective of their production method [84]. Each nanowire production technique exclusively comprises its own integration strategy. Therefore, solving the dilemma of "macroscopic nanostructures" requires revision of current nanowire production methodology.

Lithography and chemical etching for nanowire fabrication enable production of wafer-scale aligned nanowires with high densities and precisely defined locations [85], which could afterwards be transferred to any kind of substrate [86, 87] for integration. Although these top-down techniques are quite convenient for high yield and repeatable production of nanowires, the procedure is restricted to certain materials and the equipment is costly [79].

On the other hand, bottom-up methods provide considerable versatility in nanowire composition and dimensions, and some solution based methods, such as synthesis of metallic nanowires in aqueous environment [88], are quite cost-effective. Various techniques exist for integration of bottom-up nanowires. Nanowire dispersion based methods were investigated thoroughly since in many techniques nanowires are formed inside or suspended into liquids. The problem herein is the alignment of the randomly oriented nanowires, which could be achieved by directional flow of the liquid through microfluidic channels [89, 90], compressing nanowires on a Langmuir-Blodgett trough [91] or similarly in a liquid-liquid interface [92], applying electric field to recruit and align nanowires on predetermined positions [93, 94], blow extrusion of polymer suspension of nanowires [95], or assisting the assembly by biological entities [96] or by graphene [97].

Large area integration and alignment of nanowires produced in a relatively ordered manner, on the other hand, could be accomplished by methods like template based synthesis of nanowires [98], bridging parallel substrates [99], or embedding vertically grown nanostructures inside flexible polymers [100]. Contact printing is another versatile method for managing vertically grown nanowires [101, 102] that large scale integration of nanowires into device prototypes such as imaging circuitry [103, 104] or artificial skin [105] could be attained. Industrial scale practice of all these methods is largely constrained by the fact that these techniques require considerable expertise

and custom designed machinery, and also some might be not suitable for mass production intrinsically.

We have developed a new iterative thermal size reduction technique [106] for production of flexible polymer embedded indefinitely long and axially aligned one dimensional micro and nanostructure arrays of various materials including chalcogenide glasses, semiconductors, polymers and metals. The fabrication method yields nanowires with macroscopic lengths, perfect parallel alignment and tunable physical properties[107], rendering them suitable for bridging nanoscale and macroscale dimensions. Figure 6.1 shows the schematic representation of the iterative thermal size reduction technique.

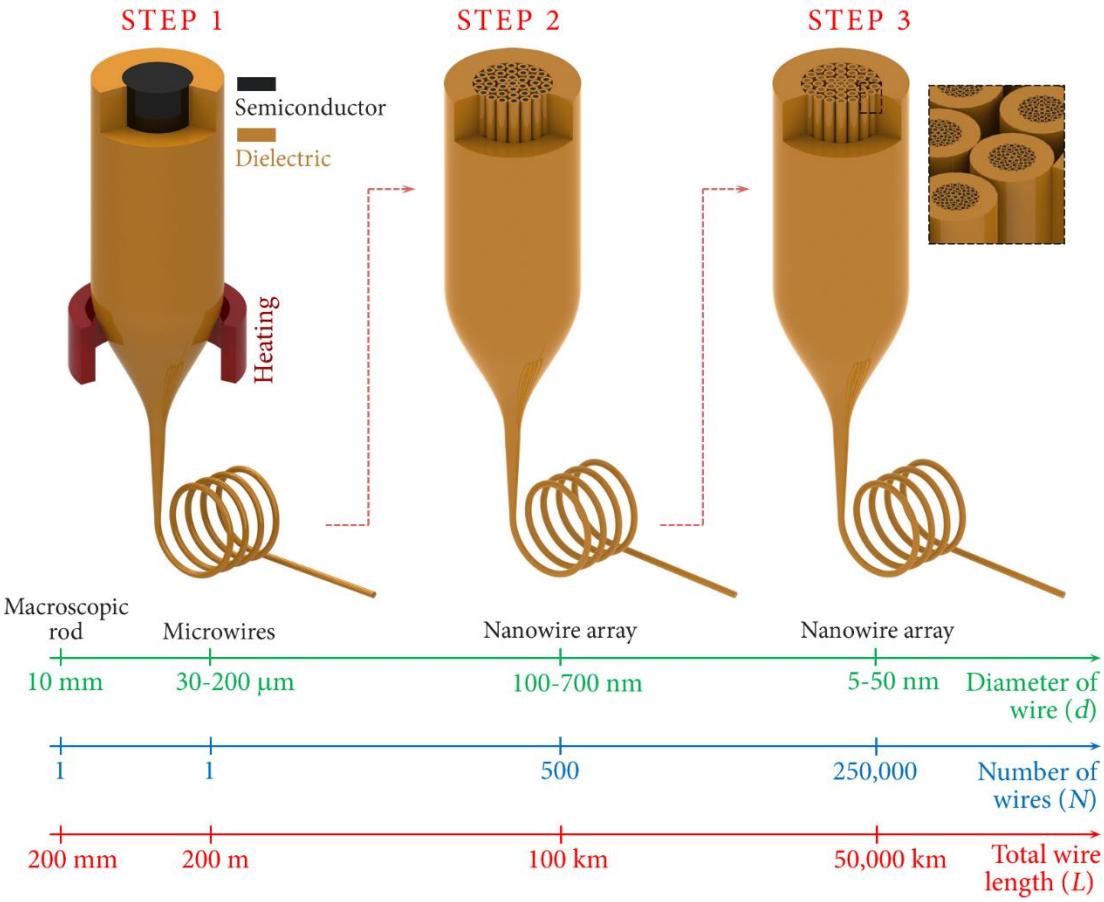

Figure 6.1: Schematic representation of iterative size reduction technique for nanowire production. A macroscopic preform containing the material of which the nanowire would be produced, encapsulated by a protecting polymer layer is prepared and then drawn in a custom built fiber tower. The resulting wires are cut into pieces and stacked together, and encapsulated again with the same polymer to obtain a second preform for a second thermal drawing step. This procedure could be repeated until nanowires of the desired size are obtained. During the process, the fiber diameter decreases, while the length and total number of micro and nanowires within the polymer encapsulated fiber increases. This method enables production of thousands of aligned and uniform nanowires of various material sets.

6.2 Emergent Semiconductor Properties in Selenium Nanowire Arrays Fabricated by Direct Size Reduction Technique

Selenium is an interesting semiconductor with distinct thermomechanical, electrical and optical characteristics such as the convenience of thermal drawing to obtain fibers

[106], photoconductivity [108], light induced crystallization, and phase dependent electrical conductivity [109]. Therefore phase change memory, optoelectronics and photodetection research could exploit these characteristics, provided that the fabrication process is carefully designed and established according to the demand of the particular field. Especially selenium nanowire and nanotubes attract considerable attention, since they exhibit improved semiconductor characteristics. Selenium nanowire fabrication is performed mainly by solution phase redox reactions [108, 110], while organic solvent and enzyme mediated atomic reorganization [111, 112], or thermal drawing of thin selenium films into nanofilaments [113] have been proposed as alternative strategies. However, industrial scale uniform and aligned selenium nanowires with high throughput yield have not been shown yet prior to our recent research [106]. This work showed that amorphous selenium nanowire arrays composed of thousands of individual selenium nanowires could be produced by iterative size reduction.

Figure 6.2 shows the Scanning Electron Microscope (SEM) image of these nanowires. The polymer encapsulation around the nanowires was dissolved in an organic solvent, dichloromethane (DCM). The exposed nanowires were sputter coated with a thin layer of Au-Pd in order to reduce charging effects by a precision etching and coating system (PECS).

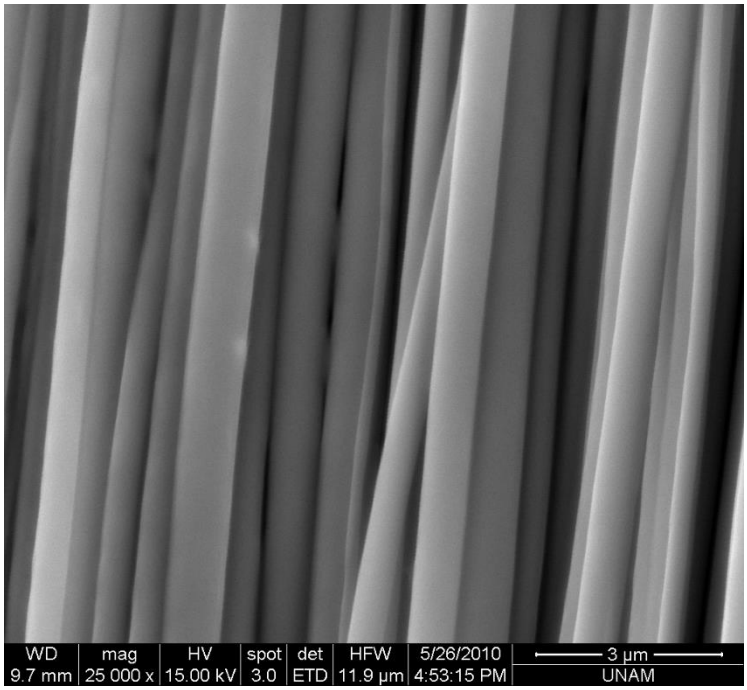

Figure 6.2: SEM image of the amorphous selenium nanowire array. The wires could be preserved axially ordered as they were produced within the encapsulating polymer layer.

In order to examine emergent properties of selenium nanowires, three different set of selenium wires were compared, which were collected from the consecutive thermal drawing steps. The wires from the first two steps were crystallized by thermal annealing, while the third step wire, which is the nanowire was crystallized by pyridine treatment. The electron microscopy cross-sections, and also crystallinity information from X-ray diffraction (XRD) or electron diffraction were given in Figure 6.3.

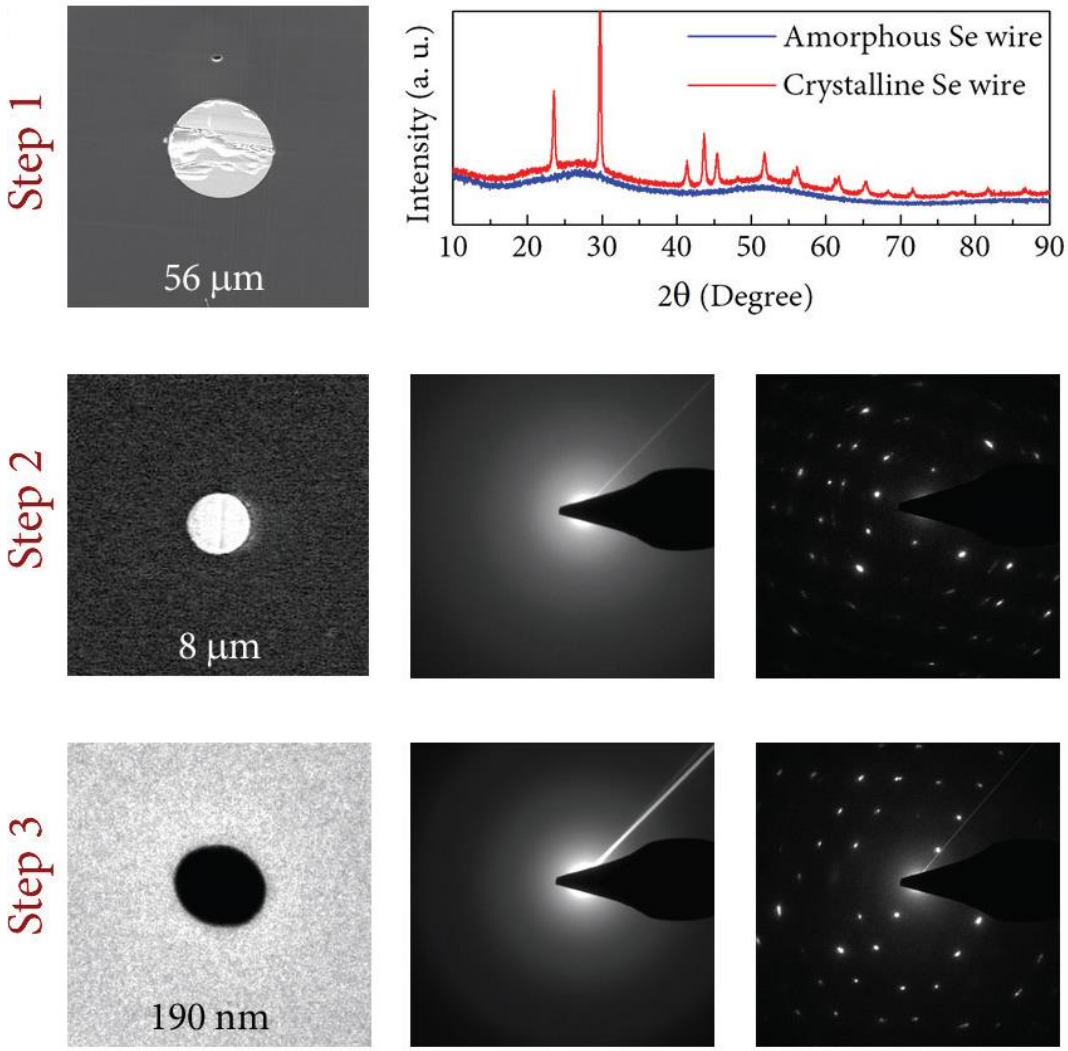

Figure 6.3: Sizes and crystalline structure of selenium micro and nanowires produced by iterative thermal drawing. Step 1 and Step 2 microwires could be crystallized by thermal annealing, while pyridine treatment was required in order to crystallize the Step 3 nanowires.

The conductivity of selenium increases dramatically when being crystallized; and normally thermal annealing is supposed to crystallize selenium [113]; however, amorphous selenium nanowires could not be crystallized via thermal annealing, possibly due to inadequate dimensions for the crystal grains to form, or an atomic level instability related to iterative thermal drawing process. Yet, selenium has an interesting property of crystallization in the presence of specific organic reagents including pyridine, aniline, piperidine, which are all ring compounds containing nitrogen [114].

Although the exact mechanism is not known, it is postulated in the literature that these solvents adsorbed on selenium surface play a catalytic role in selenium reorganization [111]. We used pyridine in order to crystallize nanowires, while we diluted pyridine as a 50% aqueous solution in order to conserve the general structure of the nanowires (Figure 6.4); otherwise the nanowires were reorganized into spiky structures (Figure 6.5).

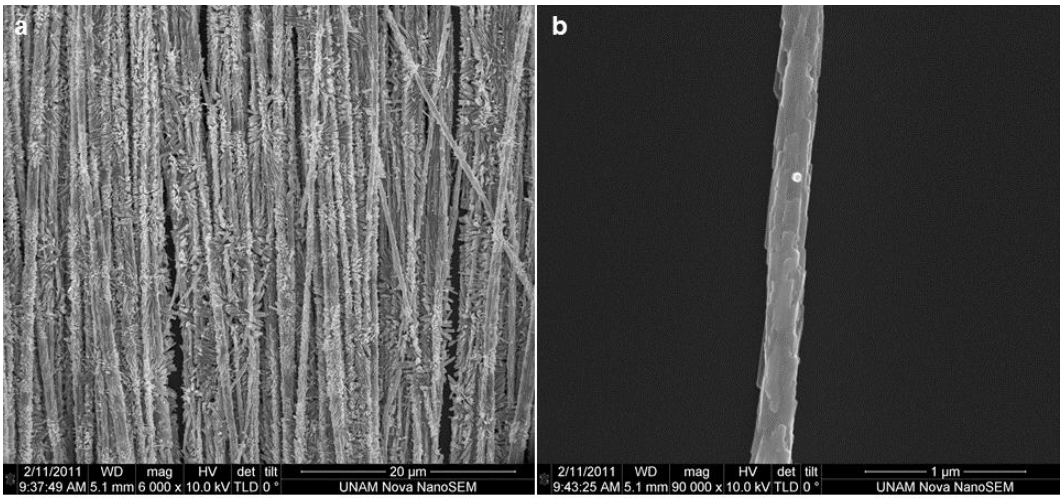

Figure 6.4: SEM micrographs of crystallized selenium nanowires. (a) SEM image of highly ordered selenium nanowire array. The wires extend to microscopic lengths, while their diameters are in the order of nanometers. (b) SEM image of a single crystalline selenium nanowire. Although the surface has a roughness to some extent, the integrity of the wire is not compromised.

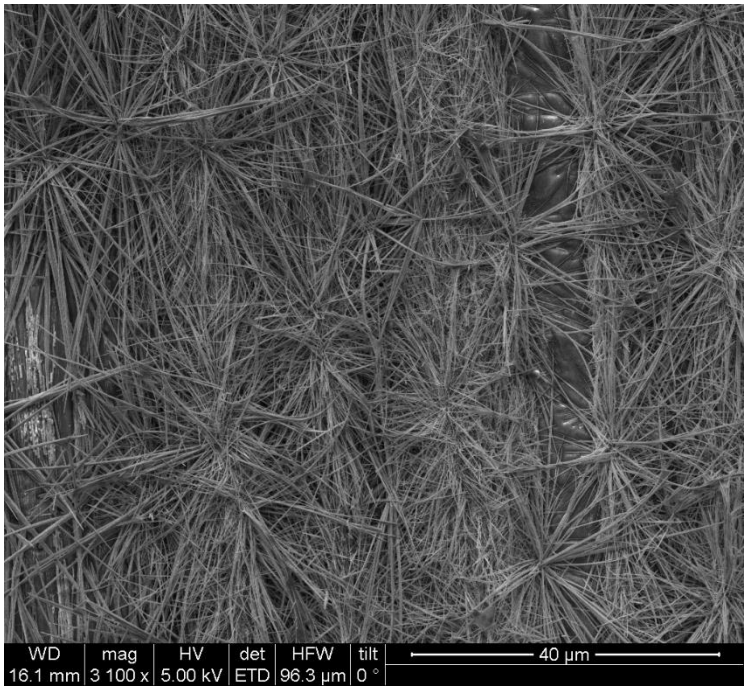

Figure 6.5: Spiky shapes formed after overnight pyridine incubation of exposed amorphous selenium nanowires.

Photoconductivity of the micro and nanowires with different sizes were compared by measuring of the increase of electrical conduction under illumination with white light. Electrical measurements were performed with Keithley 2400 Sourcemeter controlled by a generic computer program. A 50 W light source coupled to a fiber was used for illumination. Electrical contacts to the micro and nanowires were formed by applying silver paint on the facets of the fiber. Current was monitored while applying a constant voltage bias, and light was turned on and off in order to observe the photoconductivity. The results are given in figure 6.6. All data were normalized according to the initial current value for easier comparison. These results demonstrate that decreasing the size significantly increases the photoconductivity of selenium.

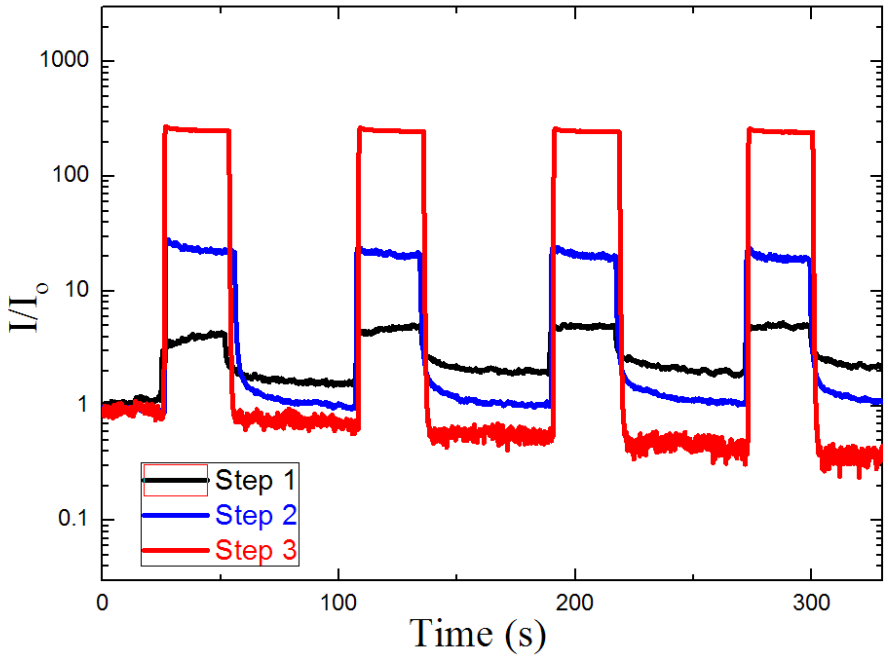

Figure 6.6: Size-dependent photoconductivity of selenium nanowires. The peaks occur when the light is on, while the conductivity decreases when the illumination is off.

One interesting observation about this experiment is that selenium wires with larger diameter revert to their previous conductivity states in longer durations. In order to understand this effect better, the photoresponse of these micro and nanowires were also investigated. The light source is modulated with an optical chopper, and the response of the micro and nanowires towards the modulated signal were measured via a lock-in amplifier. The results clearly show that the nanowires have much shorter response time compared to microwires. Figure 6.7 shows the frequency response of wires of different diameters.

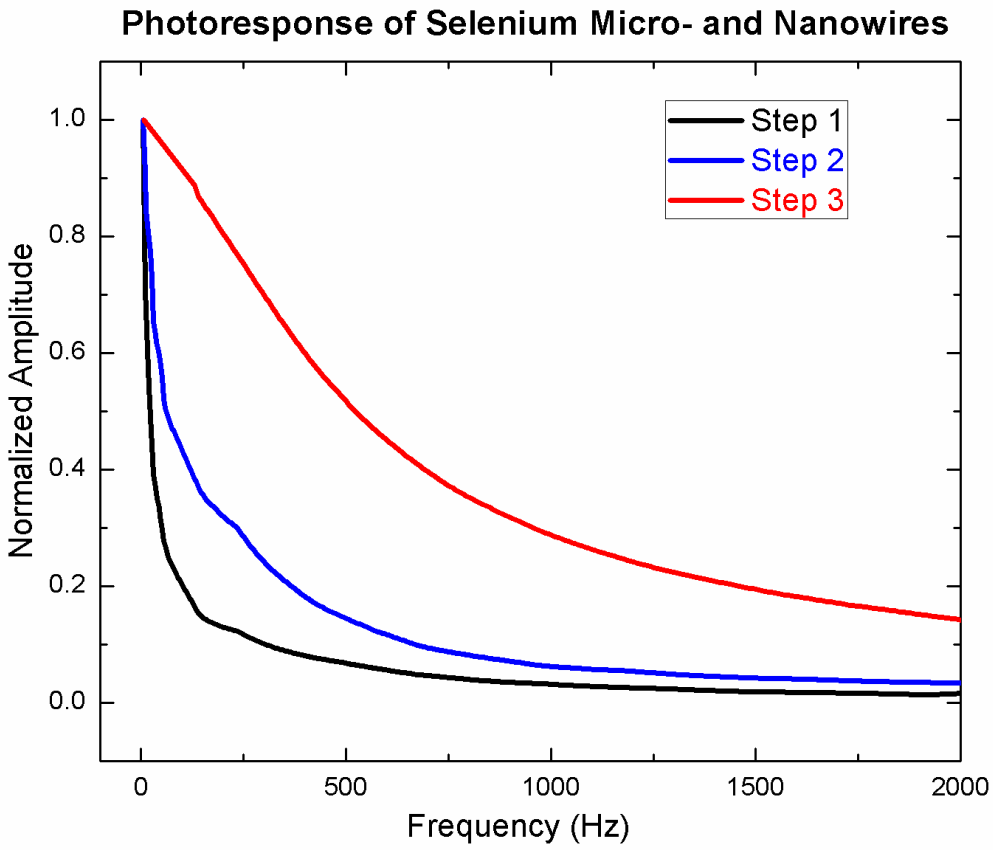

Figure 6.7: Photoresponse of selenium micro and nanowires according to their sizes. The photoresponsivity increases with decreasing sizes. The data suggests that selenium nanowires could reliably be used with kHz modulation.

6.3 Macroscopic Assembly of Indefinitely Long and Parallel Nanowires into Large Area Photodetection Circuitry

Polymer fiber embedded nanowires were used to construct large area photodetection circuitry. By manual alignment of the encapsulating fibers that contain hundreds of individual nanowires over a patterned circuitry chip, and controlled etching of the polymer encapsulation using organic solvents, parallel nanowire arrays are exposed as monolayers to form functional units over exceptionally large areas, as shown in Figure 6.8. Each circuit element is composed of hundreds of parallel nanowires, which provide durability, stability and reliability to the system, as well as enhanced signal-to-noise ratio compared to that of single nanowire circuitry. There is

virtually no limitation over the area that could be covered with nanowires totally, enabling production of remarkably large area nanowire devices. The technique is relatively substrate and nanowire composition independent. Resulting device is unique in its geometry and is capable to function in diverse applications requiring integration of nanowires into electrical circuitry, which is a serious challenge itself [115]. Finally, the integration procedure is intrinsically suitable for automation, post modification and mass production.

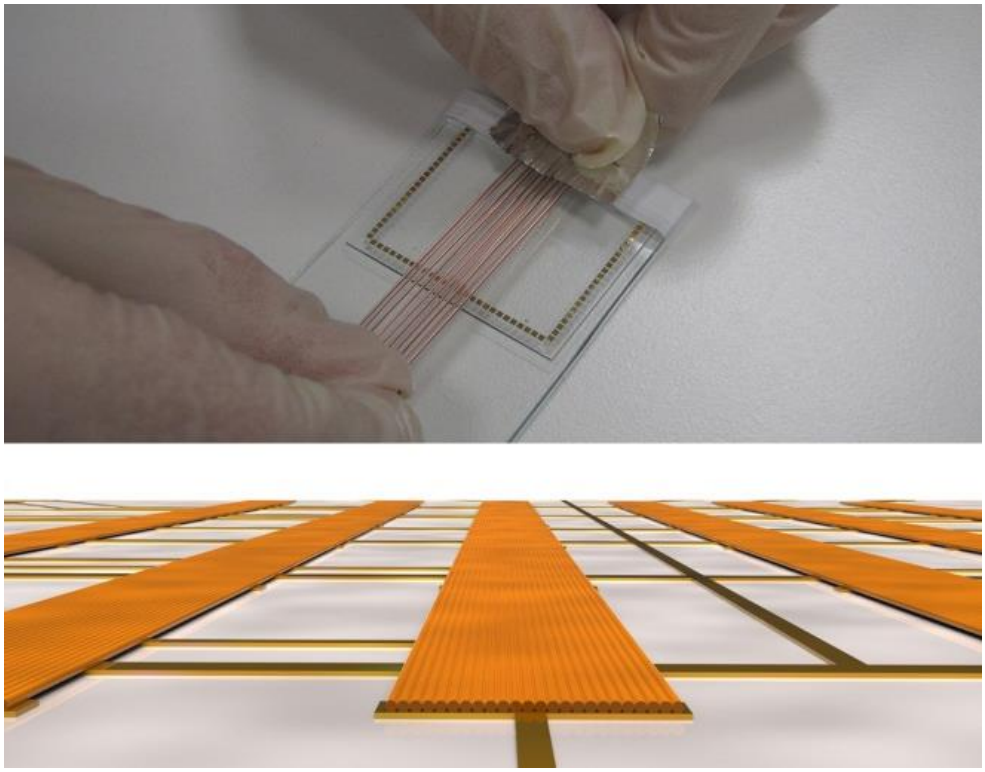

Figure 6.8: Macroscopic assembly of nanowires over a predefined circuitry. First step of nanowire integration to a macroscopic circuitry for large area photodetection is manual alignment and accommodation of polymer fiber arrays, each containing hundreds of nanowires embedded inside, over lithographically defined circuitry. A concept design of photodetection device resulting from macroscopic assembly of indefinitely long and endlessly parallel nanowires is given at the bottom. Nanowires are exposed over the metal electrode pairs as monolayers, forming pixels as photoconductive units, which are addressable by external readout circuits. Exposed light intensity can be deduced by applying a constant voltage across the pair of electrodes and measuring the change in conductance.

As a proof of principle, a nanowire based circuitry for photodetection, which is an area of intensive research [116] was constructed. The diameters of these nanowires were around 500 nm. We prepared the chip of the circuitry on Pyrex glass by lithography, gold deposition and lift-off. It contained a 10x10 pixel array in an area of 1 cm^2. We manually assembled fibers on the chip and stabilized their position with Teflon tape, then immersed them in DCM longitudinally with a slight tilt towards the bottom of the container; therefore, the exposed nanowires would be supported by the substrate. We let DCM to evaporate slowly, without disturbing the orientation of the polymer-free individual nanowires, which tend to form monolayers on the substrate. After the evaporation, we gently washed the chip with DCM in order to remove the PES remnants. The process was shown schematically in Figure 6.9.

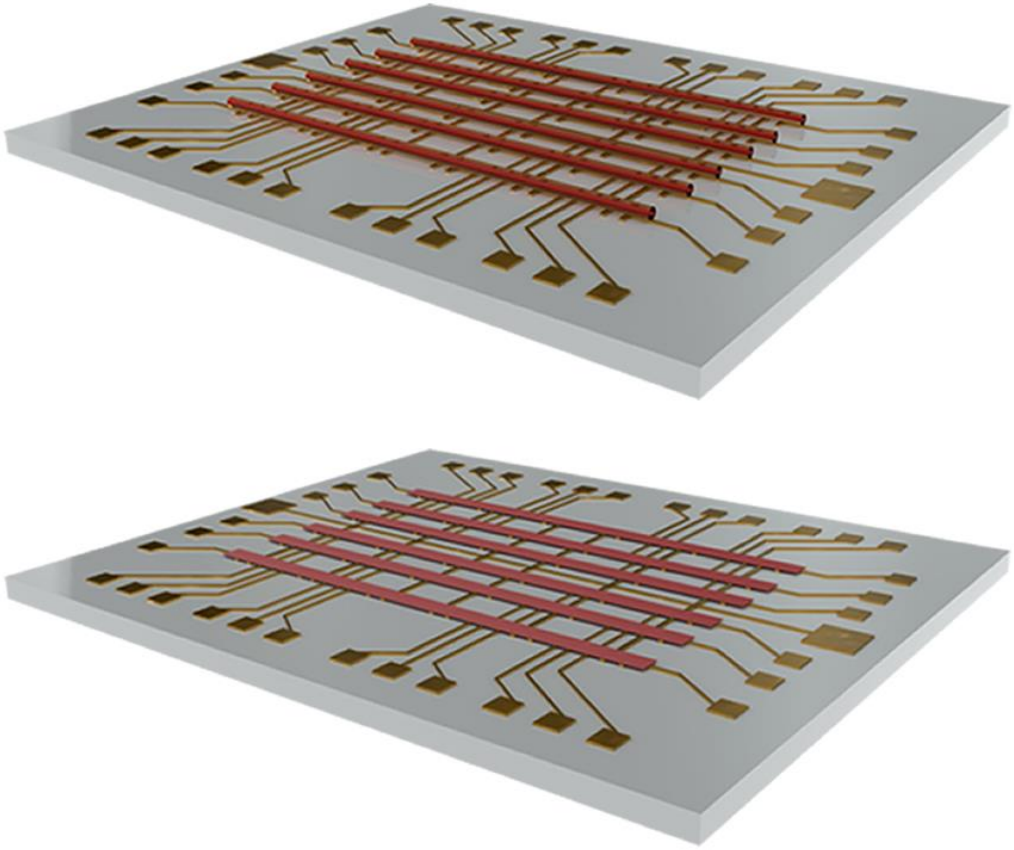

Figure 6.9: Schematic representation of nanowire based circuitry fabrication. After the nanowire arrays were properly placed over the electrical contacts, the polymer encapsulation was gently dissolved without disturbing the position of the nanowires. There, nanowires formed conduction channels over the electrodes.

We immersed the chip into a 50% by volume aqueous pyridine solution overnight to crystallize the selenium nanowires [114]. Crystalline structure of the selenium was investigated via high resolution transmission electron microscopy (Figure 6.10)

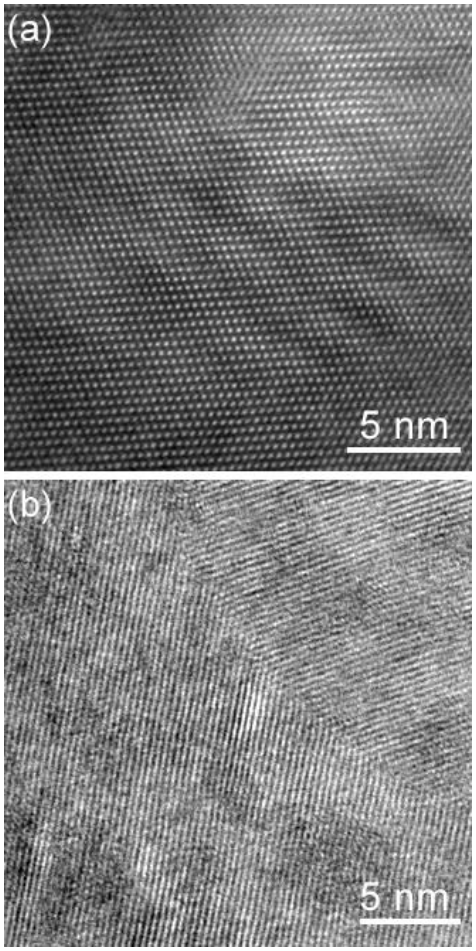

Figure 6.10: High resolution transmission electron microscopy images of the selenium nanowires after crystallization. Fiber embedded nanowires were assembled over a TEM grid, and after removal of the polymer encapsulation, they were crystallized by exposing to an aqueous pyridine solution, 50% by volume, overnight. Pyridine reorganizes selenium atoms into crystalline form, while being diluted preserves the integrity of individual nanowires. The crystal structure could be (a) single crystal or (b) polycrystalline.

The SEM image of the resulting structure is shown in Figure 6.11. Each fiber was aligned over a column of ten electrode pairs. Figure 6.11a shows the global orientation of the nanowires over the circuitry, and Figure 6.11b is a detailed image of a single pixel, composed of hundreds of parallel nanowires over electrode pairs.

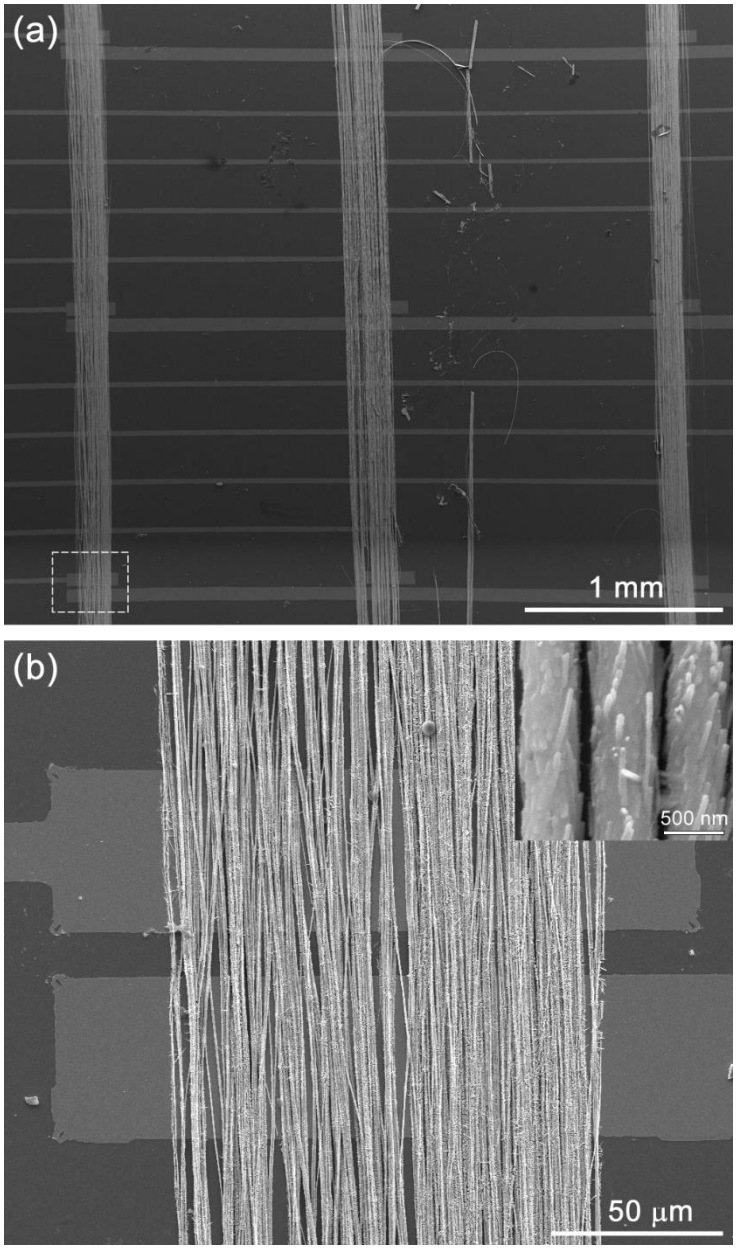

Figure 6.11: SEM image of the large area nanowire device. (a) The electron microscopy image of crystallized selenium nanowires lying over ground and readout electrodes of the lithographically defined circuitry. A 3x3 pixel part of the device is shown here. Even though pixels are sparsely distributed on the circuitry, nanowire alignment over the electrode pairs of pixels can be easily accomplished. The limits of a device prepared by manual macroscopic alignment is defined only by photolithography. (b) SEM image of a single pixel, composed of hundreds of photoconductive selenium nanowires aligned over electrode pairs. Distance between a pair of electrodes is 10 micrometers. A high resolution SEM image of NW arrays can be seen in the inset.

In order to utilize resulting structure as a sensing part of an imaging device, first of all, we investigated photoconductive properties of each pixel under dark, constant and on-off modulated illumination with a broadband light source. Applying a constant voltage of 10 volts between the common ground and data readout electrodes, pixel photocurrent was monitored versus time under on-off modulated illumination, of which results are given in Figure 6.12a. Current and Voltage (IV) characteristics of the pixels under static dark and bright illumination were obtained as shown in Figure 6.12b. Dark current Io (I_{Dark}) is found to be on the order of picoampers.

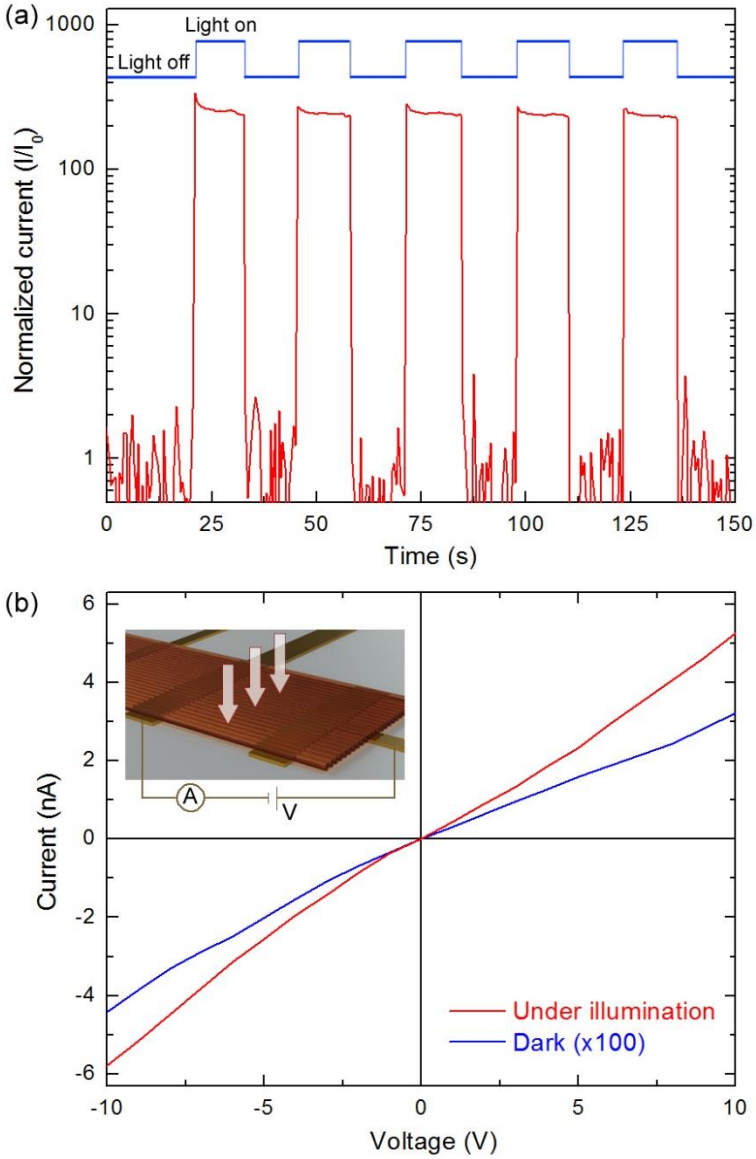

Figure 6.12: Electrical characterization of a single nanowire array over the electrodes. (a) Photoconductive response of a nanowire based pixel under on-off modulated illumination of a broadband light source. Current data is normalized to dark current I_o which is on the order of picometers. (b) Current-voltage characterization of one of the pixels for a static dark (blue) and bright illumination (red) showing ohmic behavior. Inset shows an individual pixel under applied voltage and illumination at constant intensity.

To use a circuitry composed of nanowire-based pixel array as an imaging device, photoconductive response of each pixel needs to be converted into a grayscale color of corresponding pixel from which an image is to be constructed. To accomplish this,

we designed custom readout hardware for photodetection circuitry and developed application software for image construction. Photoconductive responses of every pixel in the 10x10 array as a voltage signal were sampled by analog multiplexers, 10 bit digitized and converted to 8 bit gray scale color values. Before constructing an image, each pixel must be calibrated to match their photosensitivities since they might have slightly different responses to the same light intensity due to the fabrication ambiguities such as number of active nanowires in contact with electrode pairs and electrical contact quality. Distribution of pixel photosensitivity shows that majority of functional pixels has almost same sensitivity except a few highly sensitive and insensitive pixels (Figure 6.13).

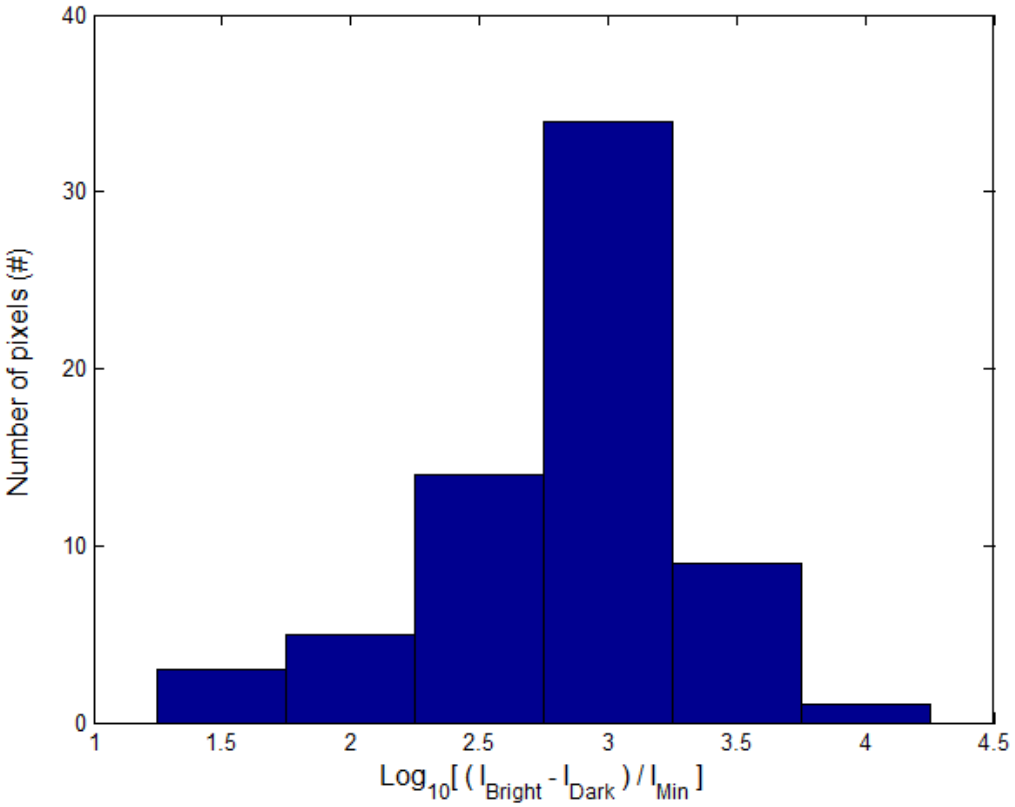

Figure 6.13: Capturing, displaying and identifying via large-area nanowire based photodetector circuitry. The circuitry is composed of a 10 x 10 pixel array over an area of 1 cm^2, over which pixels have 1 mm separation. In order to create an image, dark field imaging was applied via passing white light through transparent parts of a shadow mask. The mask was prepared by printing alphabetic characters on transparent paper. The increase in conductivity regarding light exposure on the illuminated pixels were monitored and conditioned by the embedded software, and the information is then transferred to the computer via USB. After calibration of each pixel by a custom built application software, alphabetic characters were identified in the images captured by the device.

Calibration was done by the software for each pixel using photoresponse values of static dark and bright illumination of predetermined intensity. Nanowire assembled photodetection circuitry and readout electronics can be seen in Figure 6.14a. Full exposure of the device to static dark and bright illumination with calibrated pixels is shown in Figure 6.14b and Figure 6.14c, respectively. Blue pixels denote dead pixels, which are found to be poorly sensitive or completely insensitive to the light as a result of broken metal lines produced by lift-off process or poor electrical contact formation

between nanowires and pixel electrodes due to misalignment of the fibers. Using close contact masks, dark field illumination of some characters can be projected on the pixel array (Figure 6.15) and captured by the software as images of alphabetic characters shown in Figure 6.14d. Using right-angle sided fonts and careful alignment of close contact masks over the sparsely distributed pixels of the circuitry, we obtained images of sharp contrast. The device is 68% functional.

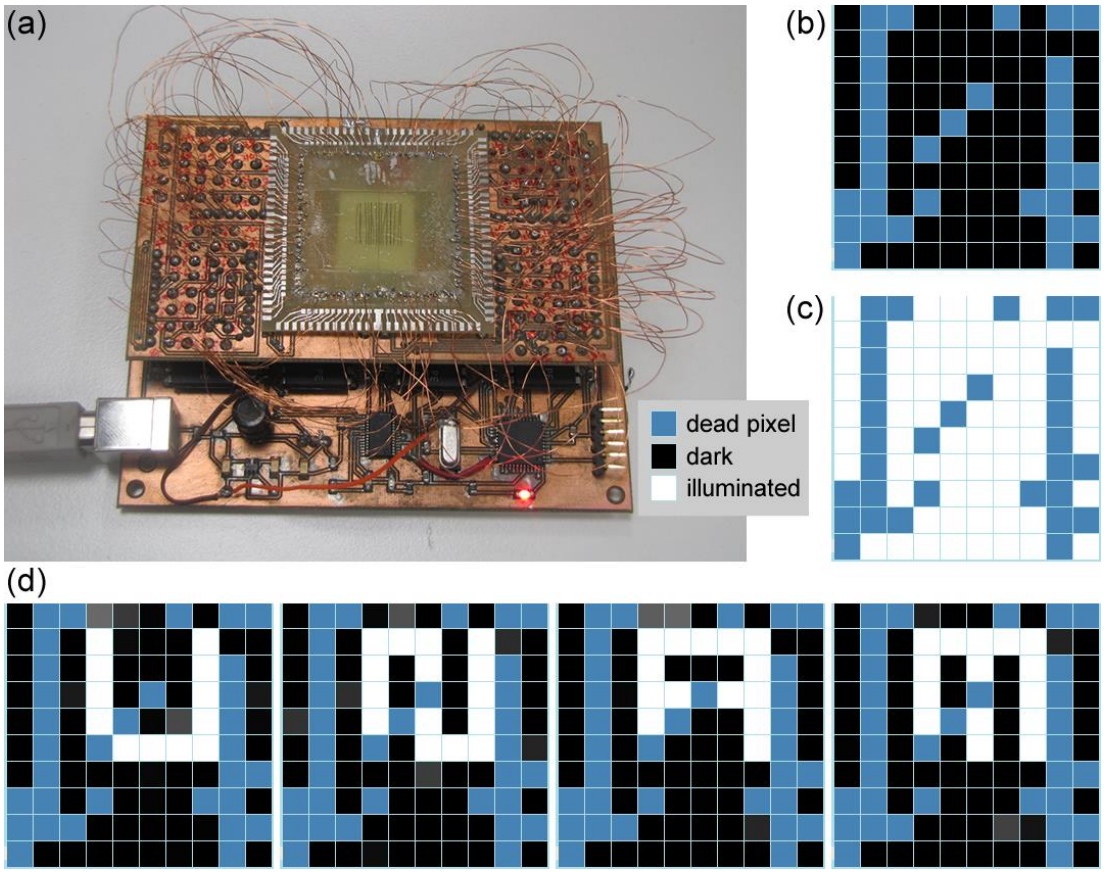

Figure 6.14: Large area nanowire photodetection circuitry. (a) Assembled selenium nanowires on photodetection circuitry and custom made readout electronics. (b) Software constructed image of 10 x 10 pixels after full exposure of the device to a light source for static dark and (c) bright illumination. (d) Images of dark field illuminated alphabetic characters of "UNAM" captured by nanowire based pixel array. Blue pixels are dead pixels which can result from the imperfections of electrical contacts on the circuitry or of the nanowire alignment process. There are particularly two dead pixel columns, related to a slight misalignment of the nanowires over the pixel electrodes.

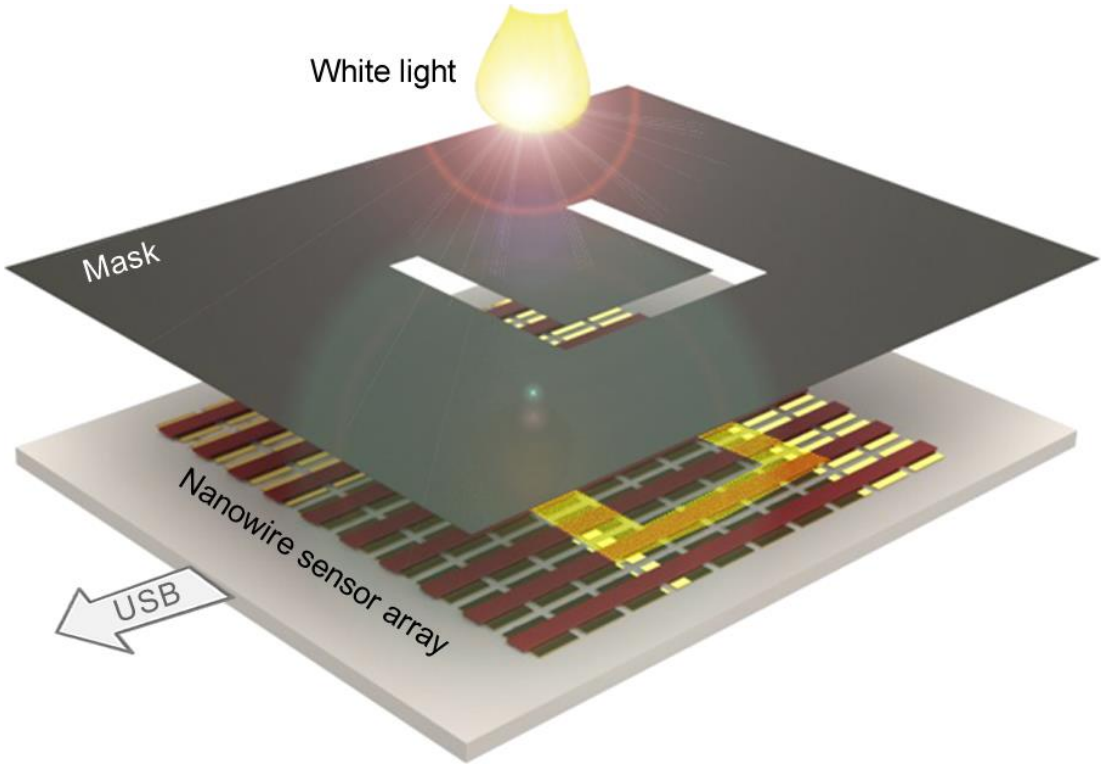

Figure 6.15: Capturing, displaying and identifying via large-area nanowire based photodetector circuitry. The circuitry is composed of a 10x10 pixel array over an area of 1 cm^2, over which pixels have 1 mm separation. In order to create an image, dark field imaging was applied via passing white light through transparent parts of a shadow mask. The mask was prepared by printing alphabetic characters on transparent paper. The increase in conductivity regarding light exposure on the illuminated pixels were monitored and conditioned by the embedded software, and the information is then transferred to the computer via USB. After calibration of each pixel by a custom built application software, alphabetic characters were identified in the images captured by the device.

In this work, we demonstrated fabrication of nanowire based photodetection device by macroscopic manual assembly of nanowires. We used in-fiber nanowires in construction of the device, and removed the polymer encapsulation by dissolving it within an organic solvent, DCM. The continuous and aligned nanowires are originally accumulated at the center of the polymer fiber, which acts as a guide for manual alignment. After the accommodation of the fibers onto the circuitry, we protected the edges from being etched; therefore, only the center is exposed to the solvent. The nanowires thus expanded as a monolayer around the area defined by their original position. This strategy is quite efficient, except in some cases if the fibers could not be

placed firmly on the substrate, they might be slightly misaligned to the desired contact area, causing columns of dead pixels, as could be observed in our device. This could be avoided by fixing the fibers better onto the substrate. The etching process is sensitive against agitation such that the alignment could be distorted, and especially if the solvent is removed too quickly after the exposure, the nanowires tend to aggregate as bundles, which might impair the device performance, because either the number of nanowires on the electrical contacts will decrease, or the nanowires on top of others will prevent the photons reach the conducting wires. However, a slow transfer of the solvent out of the container might work, as well as evaporation. In our case, misalignment is a more serious problem than bundling.

Our pixels are sparsely distributed over an active area of 1 cm^2, with resolution as low as 1 pixel/1 mm or 4 dpi. However, it can be easily improved by decreasing the space between electrode pairs and increasing the number of pixel electrodes per unit length, which is only limited by photolithography. Especially along the direction parallel to nanowires, nanowire alignment and accommodation over every pixel can be realized simultaneously. Unfortunately, increase in pixel numbers comes along with the electrical readout problem, which requires readout circuits such as used in active matrix displays.

Another problem in the readout of pixels is very high impedance of nanowires between pair electrodes, which can be on the order of 10^8 ohms. Therefore impedance matching circuits to analog digital converters are also needed in this particular case. There are two kinds of electrical coupling which can occur between pixels. For every read-out electrode of pixels, there are multi electrical pathways to the other common ground lines having contact with same nanowire bundle of the pixel and also over other nanowire bundles to the ground lines. However, these pathways have much more distance, hence much more resistance in comparison with 10 micrometer, the closest gap between pixel electrodes. This kind of situation can be always prevented by adding extra lithographic and coating steps to produce a resistive thin film coating having window openings only over the electrode pairs of pixels.

The macroscopic alignment of nanowires shown here is unique and has many advantages compared to other nanowire assembly techniques. The strength of this technique depends on the unusual state of the nanowires we use: indefinitely long,

ordered and polymer encapsulated. By this method, the position and orientation of the nanowires could be determined manually with high precision and ultimate yield. There is no restriction on the substrate characteristics, where whole surfaces of planar, curved or flexible substrates could essentially be covered with nanowires. Each functional unit is composed of hundreds of individual nanostructures, forming individual conducting channels. This maintains an extraordinary robustness to the system, when a facile single step alignment is considered. The most important aspect of this procedure is that it could be applied in diverse application fields regarding nanowire integration to large area devices at industrial scale.

To sum up, we demonstrated a strategy of nanowire integration for a large area photodetection circuitry, which utilizes controlled etching of the polymer jacket of indefinitely long nanowire arrays. The macroscopic alignment procedure used here resulted in functionalization of semiconducting nanowires as a large area functional device. Employment of thermally drawn nanowires with a macroscopic alignment approach might pave the way for very interesting occasions where nanoscale and macroscale are effectively bridged. Some possible routes towards utilization of this technique might be fabrication of nanowire thin film transistor columns, integration of phase change nanowires into various memory circuitries such as cross bar structures, fabrication of large scale nanowire based thermal sensors or artificial skin and muscle. Also integrating nanowires onto flexible or curved surface device geometries, or efficiently aligning very long core-shell nanostructures [107] for photonic and photovoltaic applications would be possible [117]. The outcomes of this research is expected to have important impacts in the photonics field in near future [118].

Chapter 7

Conclusions

The present work describes some novel large scale applications related to microphotonics, nanobiotechnology and nanophotonics. These fields are of paramount importance regarding increasing the capabilities of our civilization. Nevertheless, the research related to these areas is frequently restricted within laboratories, due to the fact that it is tedious to bridge the micro and nanoscopic systems to our macroscopic everyday lives.

One of the aims of this thesis research was developing highly sensitive biosensors also having a significant selectivity for their targets, which was accomplished to a great extent. Microtoroids have huge potentials that could make them convenient candidates for single molecule sensing. On the other hand, since they are quite sensitive towards the smallest perturbations in their environments, it is difficult to achieve selectivity simultaneously without applying extensive surface chemistry. This research, from its beginning, had a practical approach regarding many features of these microcavities, and in depth analysis of many of their traits, including detailed mathematical analysis of their optical nature was intentionally skipped. Instead, more crucial issues for the large scale applicability of these unique microstructures were investigated in detail, such as alternative fabrication and optical coupling methods. In most, if not every, case

simple but definitely “not easy” solutions to emerging problems were tried to be developed. Especially the optical coupling and measurement setup was designed and constructed elaborately. The research and development enabled us not only to investigate microtoroids, but also novel concept of on chip chalcogenide microcavities [29].

Since the most critical part of this particular research was development of a convenient surface chemistry, and the state-of-the-art coatings lacked simultaneous protein resistance and bioconjugation capability, a novel surface chemistry was developed and demonstrated successfully. This THPMP based coatings could find very important applications on many different platforms besides biosensing [74].

Functionalized microtoroids were shown to possess a significant protein resistance. They were also shown to specifically detect antigens with the aid of antibodies bioconjugated over them [78]. Although this research still requires some optimization, the preliminary results show that we are on the right track. This research will be continued, without leaving the goal of single molecule detection with ultimate selectivity.

Nanowires have many superior characteristics compared to bulk material. However, it is challenging to form large scale devices using them, due to their extremely low dimensions. Indefinitely long nanowire arrays produced by iterative thermal drawing [106] has an incredible potential to overcome many problems related to nanowire assembly. During this thesis research, semiconducting selenium nanowires were successfully assembled into a large area photodetection circuitry [117], paving the way for many novel nanowire based applications.

As a conclusion, micro/nanophotonics and nanobiotechnology are fertile fields of research, where some simple but innovative ideas could have enormous impacts. The main aim of this thesis was to be able to develop a few from such ideas, and bring these ideas to the reality. The outcomes of this research during this period, and possibility of continuation are important criteria regarding the success of all the efforts in order to realize this initial motivation.

Bibliography

[1] B. Alberts, A. Johnson, J. Lewis, M. Raff, K. Roberts, and P. Walter, "Molecular Biology of The Cell, 4th edition," *Garland Science*, 2002.

[2] B. Liedberg, C. Nylander, and I. Lundstrom, "Surface-plasmon resonance for gas-detection and biosensing," *Sensor. Actuator.*, vol. 4, no. 2, pp. 299-304, 1983.

[3] H. Muramatsu, J. M. Dicks, E. Tamiya, and I. Karube, "Piezoelectric crystal biosensor modified with protein-a for determination of immunoglobulins," *Anal. Chem.*, vol. 59, no. 23, pp. 2760-2763, Dec, 1987.

[4] X. L. Su, and Y. B. Li, "A QCM immunosensor for Salmonella detection with simultaneous measurements of resonant frequency and motional resistance," *Biosens. Bioelectron.*, vol. 21, no. 6, pp. 840-848, Dec, 2005.

[5] M. S. Luchansky, and R. C. Bailey, "High-Q Optical Sensors for Chemical and Biological Analysis," *Anal. Chem.*, vol. 84, no. 2, pp. 793-821, Jan 17, 2012.

[6] K. J. Vahala, "Optical microcavities," *Nature*, vol. 424, no. 6950, pp. 839-846, Aug 14, 2003.

[7] D. W. Vernooy, V. S. Ilchenko, H. Mabuchi, E. W. Streed, and H. J. Kimble, "High-Q measurements of fused-silica microspheres in the near infrared," *Opt. Lett.*, vol. 23, no. 4, pp. 247-249, Feb 15, 1998.

[8] D. K. Armani, T. J. Kippenberg, S. M. Spillane, and K. J. Vahala, "Ultra-high-Q toroid microcavity on a chip," *Nature*, vol. 421, no. 6926, pp. 925-928, Feb 27, 2003.

[9] A. M. Armani, and K. J. Vahala, "Biological and chemical detection using ultra-high-Q toroidal microresonators," *Biophys. J.*, pp. 29A-29A, Jan, 2007.
[10] S. Arnold, M. Khoshsima, I. Teraoka, S. Holler, and F. Vollmer, "Shift of whispering-gallery modes in microspheres by protein adsorption," *Opt. Lett.*, vol. 28, no. 4, pp. 272-274, Feb 15, 2003.
[11] F. Vollmer, S. Arnold, D. Braun, I. Teraoka, and A. Libchaber, "Multiplexed DNA quantification by spectroscopic shift of two microsphere cavities," *Biophys. J.*, vol. 85, no. 3, pp. 1974-1979, Sep, 2003.
[12] F. Vollmer, S. Arnold, and D. Keng, "Single virus detection from the reactive shift of a whispering-gallery mode," *PNAS*, vol. 105, no. 52, pp. 20701-20704, Dec 30, 2008.
[13] J. Topolancik, and F. Vollmer, "Photoinduced transformations in bacteriorhodopsin membrane monitored with optical microcavities," *Biophys. J.*, vol. 92, no. 6, pp. 2223-2229, Mar 15, 2007.
[14] A. M. Armani, R. P. Kulkarni, S. E. Fraser, R. C. Flagan, and K. J. Vahala, "Label-free, single-molecule detection with optical microcavities," *Science*, vol. 317, no. 5839, pp. 783-787, Aug 10, 2007.
[15] X. M. Zhang, and A. M. Armani, "Silica microtoroid resonator sensor with monolithically integrated waveguides," *Opt. Express*, vol. 21, no. 20, pp. 23592-23603, Oct, 2013.
[16] C. L. Zou, F. J. Shu, F. W. Sun, Z. J. Gong, Z. F. Han, and G. C. Guo, "Theory of free space coupling to high-Q whispering gallery modes," *Opt. Express*, vol. 21, no. 8, pp. 9982-9995, Apr, 2013.
[17] M. L. Gorodetsky, and V. S. Ilchenko, "High-Q optical whispering-gallery microresonators - precession approach for spherical mode analysis and emission patterns with prism couplers," *Opt. Commun.*, vol. 113, no. 1-3, pp. 133-143, Dec, 1994.
[18] S. M. Spillane, T. J. Kippenberg, O. J. Painter, and K. J. Vahala, "Ideality in a fiber-taper-coupled microresonator system for application to cavity quantum electrodynamics," *Phys. Rev. Lett.*, vol. 91, no. 4, pp. 4, Jul, 2003.
[19] L. Ding, C. Belacel, S. Ducci, G. Leo, and I. Favero, "Ultralow loss single-mode silica tapers manufactured by a microheater," *Appl. Optics*, vol. 49, no. 13, pp. 2441-2445, May, 2010.
[20] T. A. Birks, and Y. W. Li, "The shape of fiber tapers," *J. Lightwave Technol.*, vol. 10, no. 4, pp. 432-438, Apr, 1992.

[21] H. S. Haddock, P. M. Shankar, and R. Mutharasan, “Fabrication of biconical tapered optical fibers using hydrofluoric acid,” *Mat. Sci. Eng. B-Solid,* vol. 97, no. 1, pp. 87-93, Jan, 2003.
[22] F. Orucevic, V. Lefevre-Seguin, and J. Hare, “Transmittance and near-field characterization of sub-wavelength tapered optical fibers,” *Opt. Express,* vol. 15, no. 21, pp. 13624-13629, Oct, 2007.
[23] B. E. A. Saleh, and M. C. Teich, "Fundamentals of photonics, 2nd edition," *John Wiley &* Sons, 2007.
[24] C. E. Soteropulos, K. M. Zurick, M. T. Bernards, and H. K. Hunt, “Tailoring the Protein Adsorption Properties of Whispering Gallery Mode Optical Biosensors,” *Langmuir,* vol. 28, no. 44, pp. 15743-15750, Nov, 2012.
[25] Z. Y. Li, R. G. T. Bennett, and G. E. Stedman, “Swept-frequency induced optical cavity ringing,” *Opt. Commun.,* vol. 86, no. 1, pp. 51-57, Oct, 1991.
[26] K. Srinivasan, M. Borselli, T. J. Johnson, P. E. Barclay, O. Painter, A. Stintz, and S. Krishna, “Optical loss and lasing characteristics of high-quality-factor AlGaAs microdisk resonators with embedded quantum dots,” *Appl. Phys. Lett.,* vol. 86, no. 15, pp. 3, Apr, 2005.
[27] Y. Takahashi, H. Hagino, Y. Tanaka, B. S. Song, T. Asano, and S. Noda, “High-Q nanocavity with a 2-ns photon lifetime,” *Opt. Express,* vol. 15, no. 25, pp. 17206-17213, Dec, 2007.
[28] M. Notomi, E. Kuramochi, and T. Tanabe, “Large-scale arrays of ultrahigh-Q coupled nanocavities,” *Nat. Photonics,* vol. 2, no. 12, pp. 741-747, Dec, 2008.
[29] O. Aktas, E. Ozgur, O. Tobail, M. Kanik, E. Huseyinoglu, and M. Bayindir, “A New Route for Fabricating On-Chip Chalcogenide Microcavity Resonator Arrays,” *Advanced Optical Materials,* vol. 2, no. 7, pp. 618-625, Jul, 2014.
[30] W. Senaratne, L. Andruzzi, and C. K. Ober, “Self-assembled monolayers and polymer brushes in biotechnology: Current applications and future perspectives,” *Biomacromolecules,* vol. 6, no. 5, pp. 2427-2448, Sep-Oct, 2005.
[31] F. Zhang, S. W. Liu, Y. Zhang, Z. G. Chi, J. R. Xu, and Y. Wei, “A facile approach to surface modification on versatile substrates for biological applications,” *J. Mater. Chem.,* vol. 22, no. 33, pp. 17159-17166, 2012.
[32] T. L. Sun, L. Feng, X. F. Gao, and L. Jiang, “Bioinspired surfaces with special wettability,” *Accounts Chem. Res.,* vol. 38, no. 8, pp. 644-652, Aug, 2005.

[33] H. K. Hunt, C. Soteropulos, and A. M. Armani, "Bioconjugation Strategies for Microtoroidal Optical Resonators," *Sensors,* vol. 10, no. 10, pp. 9317-9336, Oct, 2010.
[34] A. E. Nel, L. Madler, D. Velegol, T. Xia, E. M. V. Hoek, P. Somasundaran, F. Klaessig, V. Castranova, and M. Thompson, "Understanding biophysicochemical interactions at the nano-bio interface," *Nat. Mater.,* vol. 8, no. 7, pp. 543-557, Jul, 2009.
[35] J. Wang, J. D. Byrne, M. E. Napier, and J. M. DeSimone, "More Effective Nanomedicines through Particle Design," *Small,* vol. 7, no. 14, pp. 1919-1931, Jul, 2011.
[36] A. Ulman, "Formation and structure of self-assembled monolayers," *Chem. Rev.,* vol. 96, no. 4, pp. 1533-1554, Jun, 1996.
[37] J. C. Love, L. A. Estroff, J. K. Kriebel, R. G. Nuzzo, and G. M. Whitesides, "Self-assembled monolayers of thiolates on metals as a form of nanotechnology," *Chem. Rev.,* vol. 105, no. 4, pp. 1103-1169, Apr, 2005.
[38] P. E. Laibinis, M. A. Fox, J. P. Folkers, and G. M. Whitesides, "Comparisons of self-assembled monolayers on silver and gold-mixed monolayers derived from HS(CH2)21X and HS(CH2)10Y (X, Y = CH3, CH2OH) have similar properties," *Langmuir,* vol. 7, no. 12, pp. 3167-3173, Dec, 1991.
[39] M. J. Banuls, R. Puchades, and A. Maquieira, "Chemical surface modifications for the development of silicon-based label-free integrated optical (IO) biosensors: A review," *Anal. Chim. Acta,* vol. 777, pp. 1-16, Mar, 2013.
[40] M. Malmsten, K. Emoto, and J. M. Van Alstine, "Effect of chain density on inhibition of protein adsorption by poly(ethylene glycol) based coatings," *J. Colloid Interf. Sci.,* vol. 202, no. 2, pp. 507-517, Jun, 1998.
[41] S. Herrwerth, W. Eck, S. Reinhardt, and M. Grunze, "Factors that determine the protein resistance of oligoether self-assembled monolayers - Internal hydrophilicity, terminal hydrophilicity, and lateral packing density," *JACS,* vol. 125, no. 31, pp. 9359-9366, Aug, 2003.
[42] M. Kyo, K. Usui-Aoki, and H. Koga, "Label-free detection of proteins in crude cell lysate with antibody arrays by a surface plasmon resonance imaging technique," *Anal. Chem.,* vol. 77, no. 22, pp. 7115-7121, Nov, 2005.

[43] H. Lee, S. M. Dellatore, W. M. Miller, and P. B. Messersmith, "Mussel-inspired surface chemistry for multifunctional coatings," *Science*, vol. 318, no. 5849, pp. 426-430, Oct, 2007.

[44] M. Ghosh, C. Alves, Z. Tong, K. Tettey, K. Konstantopoulos, and K. J. Stebe, "Multifunctional surfaces with discrete functionalized regions for biological applications," *Langmuir*, vol. 24, no. 15, pp. 8134-8142, Aug, 2008.

[45] V. Zoulalian, S. Monge, S. Zurcher, M. Textor, J. J. Robin, and S. Tosatti, "Functionalization of titanium oxide surfaces by means of poly(alkyl-phosphonates)," *J. Phys. Chem. B*, vol. 110, no. 51, pp. 25603-25605, Dec, 2006.

[46] S. P. Pujari, Y. Li, R. Regeling, and H. Zuilhof, "Tribology and Stability of Organic Mono layers on CrN: A Comparison among Silane, Phosphonate, Alkene, and Alkyne Chemistries," *Langmuir*, vol. 29, no. 33, pp. 10405-10415, Aug, 2013.

[47] D. Gerion, F. Pinaud, S. C. Williams, W. J. Parak, D. Zanchet, S. Weiss, and A. P. Alivisatos, "Synthesis and properties of biocompatible water-soluble silica-coated CdSe/ZnS semiconductor quantum dots," *J. Phys. Chem. B*, vol. 105, no. 37, pp. 8861-8871, Sep, 2001.

[48] R. P. Bagwe, L. R. Hilliard, and W. H. Tan, "Surface modification of silica nanoparticles to reduce aggregation and nonspecific binding," *Langmuir*, vol. 22, no. 9, pp. 4357-4362, Apr, 2006.

[49] A. Popat, J. Liu, G. Q. Lu, and S. Z. Qiao, "A pH-responsive drug delivery system based on chitosan coated mesoporous silica nanoparticles," *J. Mater. Chem.*, vol. 22, no. 22, pp. 11173-11178, 2012.

[50] J. T. G. Pena, C. Sohn-Lee, S. H. Rouhanifard, J. Ludwig, M. Hafner, A. Mihailovic, C. Lim, D. Holoch, P. Berninger, M. Zavolan, and T. Tuschl, "miRNA in situ hybridization in formaldehyde and EDC-fixed tissues," *Nat. Methods*, vol. 6, no. 2, pp. 139-141, Feb, 2009.

[51] N. Renwick, P. Cekan, P. A. Masry, S. E. McGeary, J. B. Miller, M. Hafner, Z. Li, A. Mihailovic, P. Morozov, M. Brown, T. Gogakos, M. B. Mobin, E. L. Snorrason, H. E. Feilotter, X. Zhang, C. S. Perlis, H. Wu, M. Suarez-Farinas, H. C. Feng, M. Shuda, P. S. Moore, V. A. Tron, Y. Chang, and T. Tuschl, "Multicolor microRNA FISH effectively differentiates tumor types," *J. Clin. Invest.*, vol. 123, no. 6, pp. 2694-2702, Jun, 2013.

[52] C. D. Medley, S. Bamrungsap, W. H. Tan, and J. E. Smith, "Aptamer-Conjugated Nanoparticles for Cancer Cell Detection," *Anal. Chem.*, vol. 83, no. 3, pp. 727-734, Feb, 2011.
[53] A. Yildirim, E. Ozgur, and M. Bayindir, "Impact of mesoporous silica nanoparticle surface functionality on hemolytic activity, thrombogenicity and non-specific protein adsorption," *J. Mater. Chem. B*, vol. 1, no. 14, pp. 1909-1920, 2013.
[54] R. A. Shircliff, P. Stradins, H. Moutinho, J. Fennell, M. L. Ghirardi, S. W. Cowley, H. M. Branz, and I. T. Martin, "Angle-resolved XPS analysis and characterization of monolayer and multilayer silane films for DNA coupling to silica," *Langmuir*, vol. 29, no. 12, pp. 4057-4067, Mar, 2013.
[55] C. Wen, E. Barrow, J. Hattrick-Simpers, and J. Lauterbach, "One-step production of long-chain hydrocarbons from waste-biomass-derived chemicals using bi-functional heterogeneous catalysts," *Phys. Chem. Chem. Phys.*, vol. 16, no. 7, pp. 3047-3054, 2014.
[56] S. J. Wilkins, M. Greenough, C. Arellano, T. Paskova, and A. Ivanisevic, "In Situ Chemical Functionalization of Gallium Nitride with Phosphonic Acid Derivatives during Etching," *Langmuir*, vol. 30, no. 8, pp. 2038-2046, Mar, 2014.
[57] P. H. T. Ngamou, J. P. Overbeek, H. M. van Veen, J. F. Vente, P. F. Cuperus, and M. Creatore, "On the enhancement of pervaporation properties of plasma-deposited hybrid silica membranes," *RSC Adv.*, vol. 3, no. 34, pp. 14241-14244, 2013.
[58] A. Afzal, H. M. Siddiqi, S. Saeed, and Z. Ahmad, "Exploring resin viscosity effects in solventless processing of nano-SiO2/epoxy polymer hybrids," *RSC Adv.*, vol. 3, no. 12, pp. 3885-3892, 2013.
[59] X. N. Xie, M. Deng, H. Xu, S. W. Yang, D. C. Qi, X. Y. Gao, H. J. Chung, C. H. Sow, V. B. C. Tan, and A. T. S. Wee, "Creating polymer structures of tunable electric functionality by nanoscale discharge-assisted cross-linking and oxygenation," *JACS*, vol. 128, no. 8, pp. 2738-2744, Mar, 2006.
[60] L. H. Wang, Y. Tian, H. Y. Ding, and J. D. Li, "Microstructure and properties of organosoluble polyimide/silica hybrid films," *Eur. Polym. J.*, vol. 42, no. 11, pp. 2921-2930, Nov, 2006.
[61] A. Cattani-Scholz, D. Pedone, M. Dubey, S. Neppl, B. Nickel, P. Feulner, J. Schwartz, G. Abstreiter, and M. Tornow, "Organophosphonate-based PNA-functionalization of silicon nanowires for label-free DNA detection," *ACS Nano*, vol. 2, no. 8, pp. 1653-1660, Aug, 2008.

[62] J. A. Howarter, and J. P. Youngblood, "Optimization of silica silanization by 3-aminopropyltriethoxysilane," *Langmuir,* vol. 22, no. 26, pp. 11142-11147, Dec, 2006.
[63] M. Stenberg, and H. Nygren, "The use of the isoscope ellipsometer in the study of adsorbed proteins and biospecific binding reactions," *J. Phys. Colloques,* vol. 44, pp. *C10-83-6*, 1983.
[64] R. G. Chapman, E. Ostuni, S. Takayama, R. E. Holmlin, L. Yan, and G. M. Whitesides, "Surveying for surfaces that resist the adsorption of proteins," *JACS,* vol. 122, no. 34, pp. 8303-8304, Aug, 2000.
[65] J. H. Lee, J. Kopecek, and J. D. Andrade, "Protein-resistant surfaces prepared by peo-containing block copolymer surfactants," *J. Biomed. Mater. Res.,* vol. 23, no. 3, pp. 351-368, Mar, 1989.
[66] N. Muramatsu, and A. P. Minton, "Tracer diffusion of globular-proteins in concentrated protein solutions," *PNAS,* vol. 85, no. 9, pp. 2984-2988, May, 1988.
[67] M. Q. Zhang, T. Desai, and M. Ferrari, "Proteins and cells on PEG immobilized silicon surfaces," *Biomaterials,* vol. 19, no. 10, pp. 953-960, May, 1998.
[68] P. Tengvall, I. Lundstrom, and B. Liedberg, "Protein adsorption studies on model organic surfaces: an ellipsometric and infrared spectroscopic approach," *Biomaterials,* vol. 19, no. 4-5, pp. 407-422, Mar, 1998.
[69] E. Ostuni, R. G. Chapman, R. E. Holmlin, S. Takayama, and G. M. Whitesides, "A survey of structure-property relationships of surfaces that resist the adsorption of protein," *Langmuir,* vol. 17, no. 18, pp. 5605-5620, Sep, 2001.
[70] Y. Coffinier, N. Nguyen, H. Drobecq, O. Melnyk, V. Thomy, and R. Boukherroub, "Affinity surface-assisted laser desorption/ionization mass spectrometry for peptide enrichment," *Analyst,* vol. 137, no. 23, pp. 5527-5532, 2012.
[71] I. Wilkening, G. del Signore, and C. P. R. Hackenberger, "Synthesis of phosphonamidate peptides by Staudinger reactions of silylated phosphinic acids and esters," *Chemical Communications,* vol. 47, no. 1, pp. 349-351, 2011.
[72] Y. Gao, and I. Kyratzis, "Covalent Immobilization of Proteins on Carbon Nanotubes Using the Cross-Linker 1-Ethyl-3-(3-dimethylaminopropyl)carbodiimide-a Critical Assessment," *Bioconjugate Chem.,* vol. 19, no. 10, pp. 1945-1950, Oct, 2008.

[73] B. A. Kobe, S. Ramamurthy, M. C. Biesinger, N. S. McIntyre, and A. M. Brennenstuhl, “XPS imaging investigations of pitting corrosion mechanisms in Inconel 600,” *Surf. Interface Anal.,* vol. 37, no. 5, pp. 478-494, May, 2005.

[74] E. Ozgur, P. Toren, and M. Bayindir, “Phosphonate based organosilane modification for a simultaneously protein resistant and bioconjugable silica surface,” (submitted).

[75] F. Vollmer, and S. Arnold, “Whispering-gallery-mode biosensing: label-free detection down to single molecules,” *Nat. Methods,* vol. 5, no. 7, pp. 591-596, Jul, 2008.

[76] A. L. Washburn, L. C. Gunn, and R. C. Bailey, “Label-Free Quantitation of a Cancer Biomarker in Complex Media Using Silicon Photonic Microring Resonators,” *Anal. Chem.,* vol. 81, no. 22, pp. 9499-9506, Nov 15, 2009.

[77] T. Lindl, "Zell- und Gewebekultur, 5th ed.," *Spektrum Akademischer Verlag,* 2002.

[78] E. Ozgur, P. Toren, O. Aktas, E. Huseyinoglu, and M. Bayindir, “High selectivity label-free biosensing in complex media using microtoroidal resonators,” (in preparation).

[79] C. M. Lieber, and Z. L. Wang, “Functional nanowires,” *MRS Bull.,* vol. 32, no. 2, pp. 99-108, Feb, 2007.

[80] S. J. Kang, C. Kocabas, T. Ozel, M. Shim, N. Pimparkar, M. A. Alam, S. V. Rotkin, and J. A. Rogers, “High-performance electronics using dense, perfectly aligned arrays of single-walled carbon nanotubes,” *Nat. Nanotechnol.,* vol. 2, no. 4, pp. 230-236, Apr, 2007.

[81] D. M. Sun, M. Y. Timmermans, Y. Tian, A. G. Nasibulin, E. I. Kauppinen, S. Kishimoto, T. Mizutani, and Y. Ohno, “Flexible high-performance carbon nanotube integrated circuits,” *Nat. Nanotechnol.,* vol. 6, no. 3, pp. 156-161, Mar, 2011.

[82] G. Eda, G. Fanchini, and M. Chhowalla, “Large-area ultrathin films of reduced graphene oxide as a transparent and flexible electronic material,” *Nat. Nanotechnol.,* vol. 3, no. 5, pp. 270-274, May, 2008.

[83] J. W. Bai, X. Zhong, S. Jiang, Y. Huang, and X. F. Duan, “Graphene nanomesh,” *Nat. Nanotechnol.,* vol. 5, no. 3, pp. 190-194, Mar, 2010.

[84] Z. Y. Fan, J. C. Ho, T. Takahashi, R. Yerushalmi, K. Takei, A. C. Ford, Y. L. Chueh, and A. Javey, “Toward the Development of Printable Nanowire Electronics and Sensors,” *Adv. Mater.,* vol. 21, no. 37, pp. 3730-3743, Oct 5, 2009.

[85] N. A. Melosh, A. Boukai, F. Diana, B. Gerardot, A. Badolato, P. M. Petroff, and J. R. Heath, "Ultrahigh-density nanowire lattices and circuits," *Science*, vol. 300, no. 5616, pp. 112-115, Apr 4, 2003.

[86] Y. G. Sun, and J. A. Rogers, "Fabricating semiconductor nano/microwires and transfer printing ordered arrays of them onto plastic substrates," *Nano Lett.*, vol. 4, no. 10, pp. 1953-1959, Oct, 2004.

[87] M. C. McAlpine, H. Ahmad, D. W. Wang, and J. R. Heath, "Highly ordered nanowire arrays on plastic substrates for ultrasensitive flexible chemical sensors," *Nat. Mater.*, vol. 6, no. 5, pp. 379-384, May, 2007.

[88] K. Vasilev, T. Zhu, M. Wilms, G. Gillies, I. Lieberwirth, S. Mittler, W. Knoll, and M. Kreiter, "Simple, one-step synthesis of gold nanowires in aqueous solution," *Langmuir*, vol. 21, no. 26, pp. 12399-12403, Dec 20, 2005.

[89] Y. Huang, X. F. Duan, Q. Q. Wei, and C. M. Lieber, "Directed assembly of one-dimensional nanostructures into functional networks," *Science*, vol. 291, no. 5504, pp. 630-633, Jan 26, 2001.

[90] X. F. Duan, C. M. Niu, V. Sahi, J. Chen, J. W. Parce, S. Empedocles, and J. L. Goldman, "High-performance thin-film transistors using semiconductor nanowires and nanoribbons," *Nature*, vol. 425, no. 6955, pp. 274-278, Sep 18, 2003.

[91] D. Whang, S. Jin, Y. Wu, and C. M. Lieber, "Large-scale hierarchical organization of nanowire arrays for integrated nanosystems," *Nano Lett.*, vol. 3, no. 9, pp. 1255-1259, Sep, 2003.

[92] C. Y. Zhang, X. J. Zhang, X. H. Zhang, X. M. Ou, W. F. Zhang, J. S. Jie, J. C. Chang, C. S. Lee, and S. T. Lee, "Facile One-Step Fabrication of Ordered Organic Nanowire Films," *Adv. Mater.*, vol. 21, no. 41, pp. 4172-4175, Nov 6, 2009.

[93] P. A. Smith, C. D. Nordquist, T. N. Jackson, T. S. Mayer, B. R. Martin, J. Mbindyo, and T. E. Mallouk, "Electric-field assisted assembly and alignment of metallic nanowires," *Appl. Phys. Lett.*, vol. 77, no. 9, pp. 1399-1401, Aug 28, 2000.

[94] E. M. Freer, O. Grachev, X. F. Duan, S. Martin, and D. P. Stumbo, "High-yield self-limiting single-nanowire assembly with dielectrophoresis," *Nat. Nanotechnol.*, vol. 5, no. 7, pp. 525-530, Jul, 2010.

[95] G. H. Yu, A. Y. Cao, and C. M. Lieber, "Large-area blown bubble films of aligned nanowires and carbon nanotubes," *Nat. Nanotechnol.*, vol. 2, no. 6, pp. 372-377, Jun, 2007.

[96] M. W. Li, R. B. Bhiladvala, T. J. Morrow, J. A. Sioss, K. K. Lew, J. M. Redwing, C. D. Keating, and T. S. Mayer, "Bottom-up assembly of large-area nanowire resonator arrays," *Nat. Nanotechnol.*, vol. 3, no. 2, pp. 88-92, Feb, 2008.
[97] Y. G. Li, and Y. Y. Wu, "Coassembly of Graphene Oxide and Nanowires for Large-Area Nanowire Alignment," *JACS*, vol. 131, no. 16, pp. 5851-5857, Apr 29, 2009.
[98] C. R. Martin, "Nanomaterials - a Membrane-Based Synthetic Approach," *Science*, vol. 266, no. 5193, pp. 1961-1966, Dec 23, 1994.
[99] M. S. Islam, S. Sharma, T. I. Kamins, and R. S. Williams, "Ultrahigh-density silicon nanobridges formed between two vertical silicon surfaces," *Nanotechnology*, vol. 15, no. 5, pp. L5-L8, May, 2004.
[100] K. E. Plass, M. A. Filler, J. M. Spurgeon, B. M. Kayes, S. Maldonado, B. S. Brunschwig, H. A. Atwater, and N. S. Lewis, "Flexible Polymer-Embedded Si Wire Arrays," *Adv. Mater.*, vol. 21, no. 3, pp. 325-328, Jan 19, 2009.
[101] A. Javey, S. Nam, R. S. Friedman, H. Yan, and C. M. Lieber, "Layer-by-layer assembly of nanowires for three-dimensional, multifunctional electronics," *Nano Lett.*, vol. 7, no. 3, pp. 773-777, Mar, 2007.
[102] Z. Y. Fan, J. C. Ho, Z. A. Jacobson, R. Yerushalmi, R. L. Alley, H. Razavi, and A. Javey, "Wafer-scale assembly of highly ordered semiconductor nanowire arrays by contact printing," *Nano Lett.*, vol. 8, no. 1, pp. 20-25, Jan, 2008.
[103] Z. Y. Fan, J. C. Ho, Z. A. Jacobson, H. Razavi, and A. Javey, "Large-scale, heterogeneous integration of nanowire arrays for image sensor circuitry," *PNAS*, vol. 105, no. 32, pp. 11066-11070, Aug 12, 2008.
[104] W. S. Wong, S. Raychaudhuri, R. Lujan, S. Sambandan, and R. A. Street, "Hybrid Si Nanowire/Amorphous Silicon FETs for Large-Area Image Sensor Arrays," *Nano Lett.*, vol. 11, no. 6, pp. 2214-2218, Jun, 2011.
[105] K. Takei, T. Takahashi, J. C. Ho, H. Ko, A. G. Gillies, P. W. Leu, R. S. Fearing, and A. Javey, "Nanowire active-matrix circuitry for low-voltage macroscale artificial skin," *Nat. Mater.*, vol. 9, no. 10, pp. 821-826, Oct, 2010.
[106] M. Yaman, T. Khudiyev, E. Ozgur, M. Kanik, O. Aktas, E. O. Ozgur, H. Deniz, E. Korkut, and M. Bayindir, "Arrays of

indefinitely long uniform nanowires and nanotubes," *Nat. Mater.*, vol. 10, no. 7, pp. 494-501, Jul, 2011.
[107] T. Khudiyev, E. Ozgur, M. Yaman, and M. Bayindir, "Structural Coloring in Large Scale Core-Shell Nanowires," *Nano Lett.,* vol. 11, no. 11, pp. 4661-4665, Nov, 2011.
[108] B. Gates, B. Mayers, B. Cattle, and Y. N. Xia, "Synthesis and characterization of uniform nanowires of trigonal selenium," *Adv. Funct. Mater.,* vol. 12, no. 3, pp. 219-227, Mar, 2002.
[109] M. A. Popescu, "Non-crystalline chalcogenides," *Kluwer Academic Publishers,* 2002.
[110] X. M. Li, Y. Li, S. Q. Li, W. W. Zhou, H. B. Chu, W. Chen, I. L. Li, and Z. K. Tang, "Single crystalline trigonal selenium nanotubes and nanowires synthesized by sonochemical process," *Cryst. Growth Des.,* vol. 5, no. 3, pp. 911-916, May-Jun, 2005.
[111] T. Ohtani, N. Takayama, K. Ikeda, and M. Araki, "Unusual crystallization behavior of selenium in the presence of organic molecules at room temperature," *Chem. Lett.,* vol. 33, no. 2, pp. 100-101, Feb, 2004.
[112] C. T. Ho, J. W. Kim, W. B. Kim, K. Song, R. A. Kanaly, M. J. Sadowsky, and H. G. Hur, "Shewanella-mediated synthesis of selenium nanowires and nanoribbons," *J. Mater. Chem.,* vol. 20, no. 28, pp. 5899-5905, 2010.
[113] D. S. Deng, N. D. Orf, S. Danto, A. F. Abouraddy, J. D. Joannopoulos, and Y. Fink, "Processing and properties of centimeter-long, in-fiber, crystalline-selenium filaments," *Appl. Phys. Lett.,* vol. 96, no. 2, pp. 3, Jan, 2010.
[114] A. P. Saunders, "The allotropic forms of selenium," *J. Phys. Chem.,* vol. 4, no. 6, pp. 423–513, 1900.
[115] F. Leonard, and A. A. Talin, "Electrical contacts to one- and two-dimensional nanomaterials," *Nat. Nanotechnol.,* vol. 6, no. 12, pp. 773-83, 2011.
[116] R. X. Yan, D. Gargas, and P. D. Yang, "Nanowire photonics," *Nat. Photonics,* vol. 3, no. 10, pp. 569-576, Oct, 2009.
[117] E. Ozgur, O. Aktas, M. Kanik, M. Yaman, and M. Bayindir, "Macroscopic Assembly of Indefinitely Long and Parallel Nanowires into Large Area Photodetection Circuitry," *Nano Lett.,* vol. 12, no. 5, pp. 2483-2487, May, 2012.
[118] E. Ozgur, O. Aktas, and M. Bayindir, "Manually assembled macroscopic nanowire image sensor," *Opt. Photonics News,* vol. 23, pp. 36, 2012.

Appendix

MATLAB script for tracking the resonant wavelength by applying Lorentzian fit for each data frame

```
function [timecourse, totalerror] = nllorentzdata (data, t)

%   nllorentzdata is a function tracking the resonant wavelength on a WGM
%   by calculating the lorentzian fit of each data frame.
%
%   [timecourse, totalerror] = nllorentzdata(data, t)
%
%   timecourse is a matrix of two columns, one is the time,
%   and the other is the resonant wavelength. total error is the total
%   error of the calculation
%
%   data is a matrix of two columns, one is the wavelength, the independent
%   variable, and the other is the associated transmission. it consists of
%   frames of WGMs
%
%   t is the duration of each frame
%
%   Erol OZGUR, 2014


warning('off', 'stats:nlinfit:ModelConstantWRTParam');
```

```
%   calculate the number of frames

dataframe = find(data(:, 2)<0);
[r, c] = size(dataframe);

%   initiate time parameter

tindex = 0;

%   make lorentzian fit for each frame, using the function 'nllorentzfit'.
%   frames are determined by the function 'datapart'. too small
%   (uncoupling) or too big (overcoupling) transmissions are eliminated by
%   the function 'dataquality'.

timecourse = zeros(r, 2);
errorcourse = zeros(r, 2);
qcourse = zeros(r, 1);
for jj = 1:r
   frame = datapart(data, jj);
   q = dataquality(frame);
   if q > 1.2
      if q < 1.6
         [Res, mse] = nllorenzfit(frame);
      end
   end

%   write the matrices

   timecourse(tindex+1,:) = [tindex*t Res(2)];
   errorcourse(tindex+1,:) = [tindex*t mse];
   qcourse(tindex+1) = q;
```

```
   tindex = tindex+1;
end

%   filter the values with high error values

errorfilter = find(errorcourse(:,2 )>2e-18);
lerror = length(errorfilter);

for kk = 1:lerror
   timecourse(errorfilter(kk), 2) = timecourse(errorfilter(kk)-1, 2);
end
cla;
clf;

%  draw the figures

%  timecourse of resonant wavelength and smoothing

figure(1);
subplot(3, 1, 1);
plot(timecourse(:, 1), timecourse(:, 2));
hold on
stimecourse = smooth(timecourse(:, 2), 30);
plot(timecourse(:, 1), stimecourse, 'k');
title('resonant wavelength shift');

%   error for each frame

subplot(3, 1, 2);
plot(errorcourse(:,1), errorcourse(:,2), '*');
title('error');
```

```
%   data quality; i.e., quality of coupling

subplot(3,1,3);
plot(timecourse(:,1), qcourse, '*');
title('data quality');

%   save the timecourse data
save('D:\Matlab\resonator\timecourse.txt', 'timecourse', '-ASCII', '-DOUBLE', '-
TABS');

%   calculate total error

totalerror = sum(errorcourse(:,2));

warning('on', 'stats:nlinfit:ModelConstantWRTParam');



function part = datapart(data, n)

%  datapart recognizes the frames by the minus transmission value
%  intentionally placed at the end of each frame helping them to be
%  treated individually

dataframe = find(data(:, 2) < 0);
dataframe = [0; dataframe];

part = data(dataframe(n) + 1 : dataframe(n+1) - 1, :);



function q = dataquality(data)
```

```
%   dataquality analyses the coupling strength

q1 = data(1, 2)/min(data(:, 2));
q2 = data(end, 2)/min(data(:, 2));

q = min([q1 q2]);


function [param, mse] = nllorentzfit(data)

%   nllorentzfit uses the function 'nlinfit' to apply nonlinear regression
%   for fitting the data to a lorentzian function. it uses
%   'findinitialparam' function in order to estimate the fit parameters.
%
%   data is the frame. param are parameters of the lorentzian function.
%   mse is the mean square error of each lorentzian fit.
%

X = data(:, 1);
Y = data(:, 2);

initialparam = findinitialparam(data);

[param, r, j, covb, mse] = nlinfit(X, Y, 'nllorenz', initialparam);


function param = findinitialparam(data)

%   findinitialparam function estimates the parameters of the lorentzian fit.
%   these values are used as initial parameters in nonlinear regression analysis.
```

```
%   estimate the initial transmission

param(1) = mean(data(1 : 10, 2));

%   estimate the resonant wavelength

Lc = find(data(:, 2) == min(data(:, 2)));
param(2) = data(Lc(1), 1);

%   estimate the fwhm

I = param(1) - min(data(:, 2));

fwhm = find(data(:, 2) < param(1) - I/2);

param(3) = -(data(fwhm(1), 1)-data(fwhm(end), 1));

%   estimate the amplitude of coupling

param(4) = I*(param(3)/2)^2;


function Res = nllorenz(initialparam,data)

%   nllorentz is a function that calculates the lorentzian of a given
%   wavelength vector.
%   note: this function should be saved as a separate m-file

%   Res = nllorenz(data, initialparam)

%   Res is a vector of calculated transmission with the
%   data is a vector of the wavelength.
```

```
%   initialparam is a vector of four elements, which are the four
%   parameters of the lorentzian fit taken as the input.

Ti = initialparam(1); %   initial transmission
L = initialparam(2); %   resonant wavelength
fwhm = initialparam(3); %   full width half minimum
A = initialparam(4); %   amplitude of coupling

Res = Ti-A./(((L - data)).^2 + ((fwhm/2)^2));
```